ARO-D 6086.4-EN

AD 745912

THE VARIABILITIES OF WIND AND TEMPERATURE STRUCTURES IN THE LOWER TROPOSPHERE AS REVEALED BY AN INFRA-SONIC WAVE PROBE

ANDREW CHIU-AN CHUNG

JUNE 8, 1972

DEPARTMENT OF EARTH AND PLANETARY SCIENCES
MASSACHUSETTS INSTITUTE OF TECHNOLOGY
CAMBRIDGE, MASSACHUSETTS 02139

INTERIM TECHNICAL REPORT
U.S. ARMY RESEARCH OFFICE

CONTRACT NO. : DA-31-124-ARO-D-431
PROJECT NOS. : P-6086-EN
2M061102B53B

DISTRIBUTION OF THIS DOCUMENT IS UNLIMITED.

156

Security Classification

DOCUMENT CONTROL DATA - R & D

(Security classification of title, body of abstract and indexing annotation must be entered when the overall report is classified)

1. ORIGINATING ACTIVITY *(Corporate author)*

Massachusetts Institute of Technology

2a. REPORT SECURITY CLASSIFICATION

2b. GROUP

3. REPORT TITLE

The Variabilities of Wind and Temperature Structures in the Lower Troposphere as Revealed by an Infra-Sonic Wave Probe.

4. DESCRIPTIVE NOTES *(Type of report and inclusive dates)* Interim Technical Report - June 8, 1972

5. AUTHOR(S) *(First name, middle initial, last name)*

Andrew Chiu-An Chung

6. REPORT DATE	7a. TOTAL NO. OF PAGES	7b. NO. OF REFS
June 8, 1972	138	28

8a. CONTRACT OR GRANT NO. DA-31-124-ARO-D-431

b. PROJECT NO.

c.

d.

9a. ORIGINATOR'S REPORT NUMBER(S) ARO-D-6086.4-EN

9b. OTHER REPORT NO(S) *(Any other numbers that may be assigned this report)*

10. DISTRIBUTION STATEMENT

Distribution of this document is unlimited

11. SUPPLEMENTARY NOTES

12. SPONSORING MILITARY ACTIVITY

Department of the Army
U.S. Army Research Office-Durham
Box CM, Duke Station
Durham, North Carolina 27706

13. ABSTRACT

Wind variations in the atmospheric boundary layer are studied by means of an acoustic propagation experiment. The source was a quarter wave resonant tube operating at about 13.5 cps. The receiver was located 9.2 km to the South East. From the periodicity of the fluctuations, and the magnitude of the amplitude and phase variations one can infer the magnitude and scale of the atmospheric turbulence. The average RMS fluctuations levels were 20% in amplitude and 0.4 radians in phase for variations in the 1-2 minute period range. The inferred eddy sizes averaged 100 meters in the vertical, but with longer horizontal scales, and their associated wind variations averaged 0.13 $\pm$ .06 m/sec.

ia

DD FORM 1 NOV 65 1473 (PAGE 1)

S/N 0101-807-6801

Security Classification

3ND PPSO 13152

14 KEY WORDS	LINK A		LINK B		LINK C	
	ROLE	WT	ROLE	WT	ROLE	WT
Acoustic						
Wave Propagation						
Turbulence						
Atmospheric Boundary Layer						
Infra-Sonics						
Wind Fluctuations						

ii

THE VARIABILITIES OF WIND AND TEMPERATURE STRUCTURES IN THE LOWER TROPOSPHERE AS REVEALED BY AN INFRA-SONIC WAVE PROBE

ANDREW CHIU-AN CHUNG

JUNE 8, 1972

DEPARTMENT OF EARTH AND PLANETARY SCIENCES
MASSACHUSETTS INSTITUTE OF TECHNOLOGY
CAMBRIDGE, MASSACHUSETTS 02139

INTERIM TECHNICAL REPORT
U.S. ARMY RESEARCH OFFICE

CONTRACT NO. : DA-31-124-ARO-D-431
PROJECT NOS. : P-6086-EN
2M061102B53B

DISTRIBUTION OF THIS DOCUMENT IS UNLIMITED.

ja

Preface

This technical report is concerned with the theory and observations of acoustic wave propagation through the atmospheric boundary layer. The observations consist of amplitude and doppler shift variations recorded at a single receiver about 10 kilometers from the transmitting site. These observations provide indirect evidence of the magnitude and scale of the wind velocity fluctuations, which are the main causes of the acoustic propagation variations. Better resolution of the scale of these fluctuations and their distributions as a function of height can be achieved by incorporating an array of receivers recording simultaneously, and we are presently working at this extension. The array data can also define the diurnal variations of the wind and temperature profiles.

ABSTRACT

An infra-sonic wave probe has been constructed to investigate the variability of the wind and temperature structures in the lower troposphere. The probe could be used for detecting internal atmopsheric gravity waves and for studying air pollution meteorology. The turbulence and diurnal variations of the atmospheric boundary layer were detected by a prolonged operation of the probe with a fixed receiver located 9200 m to the SE of the source. At periods of .5 to 8 minutes, the wind fluctuations and eddy sizes are inferred from doppler shifts and amplitude variations. The root-mean-square horizontal wind fluctuations are .13 ± .06 m/s at heights of about 192 m. The horizontal scales of the eddies range from 200 m to 1400 m, while the vertical scales are 99 ± 28 m. Therefore the eddies appear to be horizontally elongated in the atmospheric boundary shears. Signal amplitude variations at periods of .5 to 6 hours as well as diurnal variations of air temperature and winds suggest 6 fundamental effective wind profiles in the atmospheric boundary layer. The signal source of the probe is a tube-resonator operated at a constant frequency of around 13.5 cps, and the receiver is a Globe microphone with a phase lock amplifier.

TABLE OF CONTENTS

GLOSSARY OF TECHNICAL TERMS

Some technical terms, which are often used in this work and may not be familiar to readers, are listed and briefly explained. The number following each term denotes the page where the term is defined. Definitions for commonly-used meteorological terms can be found in Glossary of Meteorology (Huschke 1959).

EFFECTIVE WIND is defined by

$$V_e = (V_y - V_{yo}) + (C - C_o),$$

where V_y = the horizontal wind component along the source-receiver line,

C = the speed of sound,

and the subscript "o" denotes the value at the Earth's surface. (41)

EFFECTIVE WIND SHEAR is the vertical gradient of the effective wind.

ELEVATED EFFECTIVE WIND SHEAR is the positive effective wind shear of the upper layer in a two-layer model. The effective wind shear in the lower layer may be positive, negative, or zero. (45)

AVERAGE RAY HEIGHT (H_{av}) is the average height to which the received signal has propagated. (41)

SHEAR VANISHING HEIGHT (z_m) is the height where the positive effective wind shear vanishes. The shear vanishing height is at about 200 m to 600 m above the Earth's surface. (43)

SIGNAL PENETRATING HEIGHT (H) is the maximum height to which the received signal has propagated. (41)

FOCUSING FACTOR (f) is the ratio of the observed signal amplitude to the amplitude which one would expect if the signal was propagating over the same horizontal distance in a homogeneous atmosphere. The focusing factor is a measure of the geometrical spreading of neighboring rays. (31) (42)

LIST OF SYMBOLS

(The number following each symbol denotes the page where the symbol is defined or first occurs.)

A	Ratio of fractional variations of signal amplitude and z_m (55)
a	Inside radius of the tube resonator (9)
a_p	Piston radius (9)
a_x, a_y, a_z	Correlation scale (62)
bar	10^6 dynes/cm^2 or 10^5 newtons/m^2, approximately equal to the surface atmospheric pressure (10)
C	Sound speed (28)
C_{Lz}	Correction factor of inferred turbulence scales for diffraction (82)
$C_{\Delta v}$	Correction factor of inferred wind fluctuation for diffraction (81)
cps	Cycle per second (1)
D	Wave parameter (79-80)
D_{zm}	Doppler shift due to the variation of z_m (56)
D_{So}	Doppler shift due to the variation of S_o (56)
E	Common coefficient of mean-square phase and amplitude variations (80)
f	Focusing factor (31) (42)
F	$F = F_a / F_d$ (56)
F_a	Observed time rate of fractional change of signal amplitude (56)
f_a	Predicted time rate of fractional change of signal amplitude (55)
F_d	Observed fractional doppler shift (56)
f_d	Predicted fractional doppler shift (55)

G	Normalized ray angle for the logarithmic profile (119)
H	Signal penetrating height (41)
H_{av}	Average ray height (41)
h_1	Lower layer thickness of a two-layer model (124)
h_b	Lower layer thickness of elevated shear profile type b (52)
h_c	Lower layer thickness of elevated shear profile type c (53-54)
K	Modification coefficient of the wave parameter for signal amplitude variations in boundary shears (81)
K_1, K_2, K_3	Signal amplitude variation coefficients (63)
K_S	$K_S = K_1 + K_2 + K_3$ (64)
K_{SM}	$K_{SM} = K_1 + K_2 / M^2 + K_3 / M^4$ (67)
$\vec{k}: (k_x, k_y, k_z)$	Wave vector (28)
L	1. Effective tube length of the resonator (9)
	2. Turbulence scale (64)
L_x	Horizontal turbulence scale perpendicular to the source-receiver line (64)
L_y	Turbulence scale along the source-receiver line (64)
L_z	Vertical turbulence scale (64)
M	1. $M = a_x / a_z$ (67)
	2. Medium parameter $M = S_o$ or z_m (126)
$\vec{n}$	Unit wave vector (28)
P	Signal source power (6)
P_o	Open end acoustic power at resonance of the signal transmitter (7)

P_p	Piston end acoustic power at resonance of the signal transmitter (7)
P_{noise}	Noise power (17)
P_{signal}	Signal power (17)
p	Acoustic pressure of the signal (31) (42)
p_p	Piston end acoustic pressure in resonance of the signal transmitter (10)
Q	1. Quality factor of the resonator (7)
	2. Ratio of fractional variation of z_m and S_o (55)
$\vec{R}$: (X, Y, Z)	Receiver coordinate (30)
R (s)	Normalized one-dimensional correlation function of wind fluctuations (64)
R_a	Radiation resistance at the open end of the resonator (7)
R_b	Dissipation resistance inside the tube resonator (9)
R_S	Ratio of the mean-square phase shift to the mean-square fractional amplitude variation (82)
$\vec{r}$: (x, y, z)	Position coordinate (30)
r	1. Magnitude of position coordinate (28)
	2. Amplitude ratio of two interfering rays (36)
S	Effective wind shear (43) (44)
S_o	Surface effective wind shear (43) (44) (45)
S_1	Lower layer shear of a two-layer model (124)
S_2	Upper layer shear of a two-layer model (124)
S/N	Signal-to-noise ratio (18)
s	One-dimensional separation coordinate (64)
t	Time coordinate (28)

T	Signal travel time (128)
u_p	Piston velocity (9)
u^*	Friction velocity (34)
$\vec{V}$: (V_x, V_y, V_z)	Wind vector (28)
V_e	Effective wind (41)
V_{av}	Average effective wind (66)
V_{xav}	The magnitude of the average horizontal wind component perpendicular to the source-receiver line (66)
V_ℓ	Reference effective wind of the logarithmic profile (44)
V_m	Effective wind at the shear vanishing height (43)
Y	Source-receiver distance, i.e., horizontal signal travel distance (41)
Y_{mini}	Minimum signal travel distance for some elevated shear profile (124) (126)
z_{am}	Height of a relatively maximum profile fluctuation (58-59)
z_{ao}	Height of zero profile fluctuation (59)
z_m	Shear vanishing height (43)
z_o	Roughness length (44)
z_p	Reference height of positive curvature profiles (44) (45)
α	Elevation angle of the signal ray, abbreviated as ray angle (41)
α_o	1. Elevation angle of the receiver (6)
	2. Initial ray angle (40)
α_ℓ	Reference ray angle for the logarithmic profile (119)
α_m	Maximum α_o (116)

α_p	Reference ray angle for positive curvature profiles (122)
β	Azimuthal angle (30)
γ	1. Imaginary part of the propagation constant inside the tube resonator (9)
	2. $\gamma = \pi/2 - \beta$ (30)
$\Delta\phi$	Signal phase shift (62)
ε	1. Turbulent energy dissipation rate (34)
	2. Sound speed fluctuation (128)
θ_{noise}	Signal phase jitter due to noise (17)
ϑ	The angle which the average wind makes with the source-receiver line (66)
λ	Signal wavelength (25)
μb: microbar	Unit of signal pressure (dyne/cm^2) (5)
ν	Signal frequency (66)
ρ	Air density (29)
$\sigma_p/\overline{p}$	Root-mean-square fractional amplitude fluctuation (63) (66)
σ_v	Root-mean-square wind fluctuation (34)
σ_{v50}	50 m-level rms wind fluctuation (84)
σ_ϕ	Root-mean-square phase variation (62) (66)
τ	Period of signal variation (66)
Ω	Angular frequency in augmented space (28)
ω	Angular frequency in propagation space (28)

LIST OF FIGURES

LIST OF TABLES

CHAPTER 1. INTRODUCTION

This work concerns the development of an infra-sonic wave probe for investigating meso-scale wind and temperature variations in the lower troposphere. Wind and temperature fluctuations have been measured by research aircraft and meteorological towers, but these direct measurements are limited in either time or space. For continuously monitoring average turbulence properties over a large area, a wave-propagation probe seems to be more suitable. When strong near-surface wind shears or inversion layers are present, one may send an acoustic signal up and receive it some distance away in the downwind direction. The amplitude variations and doppler shifts of the received signal will give information about turbulence in the atmospheric boundary layer. When strong jet streams exist in the upper troposphere, one might also get longer range signal transmissions by using the large wind shear below the jet stream cores. Then the signal variations would give information about perturbing winds due to internal atmospheric gravity waves, which have often been found to accompany atmospheric jet streams.

A quarter wave tube-resonator with resonant frequency of around 13.5 cps was built as an acoustic source. A Globe microphone and a phase lock amplifier were used as the receiver. Field data was collected with signal travel distance only up to 9.2 km. The signal penetrating height was limited by a shear vanishing height which is about 200 m to 600 m above the Earth's surface. From the observed average signal amplitude and weather information, the average ray height was estimated to be about 192 m.

Signal variations with periods of about .5 to 8 min. were mainly caused by the turbulent air motion drifting with the average wind in the atmospheric boundary layer. Wind perturbations due to gravity waves were ruled out, because the few gravity waves which occurred during the measurements did not seem to have large enough fluctuating wind components along the source-receiver line of the probe to cause detectable signal variations. A ray theory for signal propagation in the atmospheric boundary layer was developed to analyze the field data. Formulas for root-mean-square amplitude and phase variations of the probing signal were derived. Then, from the observed periodicity and the average wind component along the source-receiver line, one estimated the horizontal turbulence scale. From the observed phase shift and the estimated horizontal turbulence scale, one inferred the average horizontal wind fluctuation. Finally, from both the phase shift and the amplitude variation, one inferred the vertical turbulence scale. The inferred wind fluctuations and turbulence scales are generally consistent with those obtained from meteorological tower measurements elsewhere. The horizontally elongated shape of the inferred eddies appears to be characteristic of the turbulence in boundary shears.

Signal amplitude variations with periods of .5 to 6 hours suggest diurnal properties of the atmospheric boundary layer, whose wind and temperature structures can be described by 6 fundamental effective wind profiles.

Chapter 2 describes the equipment. This includes, in addition to the signal source and receiver, wind screens and a Daniels pipe for improving the signal-to-noise ratio at the receiver. Chapter 3 presents the theoretical aspect of the probe experiment. It starts with a summary of the general ray theory. Then it introduces the shallow angle approximation, which is proper for signal propagation in the atmospheric boundary layer. This approximation helps considerably in evaluating the ray characteristics of 6 fundamental effective wind profiles. A linear theory of parabolic profile fluctuations is also presented to predict possible amplitude variations and doppler shifts. Finally, in chapter 3, root-mean-square amplitude and phase variations due to boundary layer turbulence are derived, assuming a three-dimensional Gaussian correlation function. Chapter 4 gives experimental results. Firstly, typical examples of field data and its analysis are demonstrated. The accuracy of all analyzed data is estimated. Then wind fluctuations and turbulence scales inferred from all available data are discussed in the light of current status of the research about atmospheric turbulence. The possible signal variations due to gravity waves are discussed. Experimental evidences of diurnal variations of the atmospheric boundary layer are also presented. Chapter 5 summarizes the results of the probe experiment and suggests directions for further improvements. The appendices include the details of experimental results and some algebras of the theory.

CHAPTER 2. THE INFRA-SONIC WAVE PROBE

In order to use the amplitude and frequency information of the probe, one must have a signal source whose power output and frequency are steady. The signal receiver must be sensitive enough to measure the amplitude and frequency variations due to the atmospheric fluctuations that are to be investigated. The signal source was obtained by building a quarter wave tube-resonator and closely controlling the driving frequency. The signal receiver consisted of a Globe microphone and a phase lock amplifier which can measure variations of the acoustic amplitude down to .001 μb (dyne/cm^2) and doppler shifts accurate to .01% of the source frequency. The performance of the signal receiver very much depends on the signal-to-noise ratio at the receiving site. With a fixed source power, an improvement of signal-to-noise ratio can only be obtained by reducing the background noise. Wind screens and a Daniels pipe were found very helpful in this respect.

2-1. The signal source

The signal is produced by a quarter wavelength resonant tube, which is a Sontube 20 feet long and 20 inches in diameter, sitting upright on a base frame 3 feet above the ground. The upper end of the tube is open and its bottom end is closed by a rubber diaphragm. Two aluminum plates, one on each side of the diaphragm, are pinched together as a piston. The piston is driven up and down by a one horsepower DC motor through a linkage, which transfers the rotation of the motor shaft into the vertical motion of the piston.

The apparent source power as determined by a receiver on the ground is 4 times the real source power because of the ground reflection which doubles the signal amplitude at the receiver. If the quarter wavelength resonant tube was situated on a flat plain in a uniform atmosphere, the ground reflection would make the signal source look like a dipole source with a separation of a half wavelength between the real point source and its image (Morse and Ingard 1968, p. 368). The apparent source power to a receiver above the ground would be $4P\cos^2[(\pi/2)\sin\alpha_o]$, where P is the real source power emitted from the top of the tube, and α_o is the elevation angle of the receiver in a coordinate system with the tube bottom as the origin. Therefore, to a receiver on the ground ($\alpha_o = 0$), the apparent source power is 4 P. Throughout this experiment, the receiver is always located on the ground.

At resonance, the real acoustic power from the open end of the tube was determined to be 15 watts. The quality factor (Q) of the resonator, defined as the ratio of the resonant frequency to the frequency width of half-power points on the power versus frequency curve (Fig. 2-1.1), was found to be 30. One can analyze the resonant tube by assuming two plane waves inside the tube, one going upward and the other downward. The lower boundary condition is that the particle velocity is equal to the piston velocity. The upper boundary condition is that the ratio of acoustic pressure to particle velocity is equal to the radiation impedance as given by Morse (1948, p. 333) or Morse & Ingard (1968, p. 473). The results give

Q (the quality factor)

$$= (\pi/4)\rho c/(R_a + R_b),$$

P_o (the open end acoustic power at resonance)

$$= (\pi/2)\, R_a\, (\rho c\, a_p\, u_p)^2 \,/\, (R_a + R_b)^2$$

$$= (8/\pi)\, R_a\, (a_p\, u_p\, Q)^2,$$

and P_p (the piston end acoustic power at resonance)

$$= (\pi/2)\, (\rho c\, a_p\, u_p)^2 \,/\, (R_a + R_b)$$

$$= 2\rho c\, Q\, (a_p\, u_p)^2,$$

where ρc = the characteristic impedance

$= 407$ newton-sec/m^3,

R_a = the radiation resistance at the open end

Fig. 2-1.1 The relative acoustic power vs. frequency of the signal transmitter

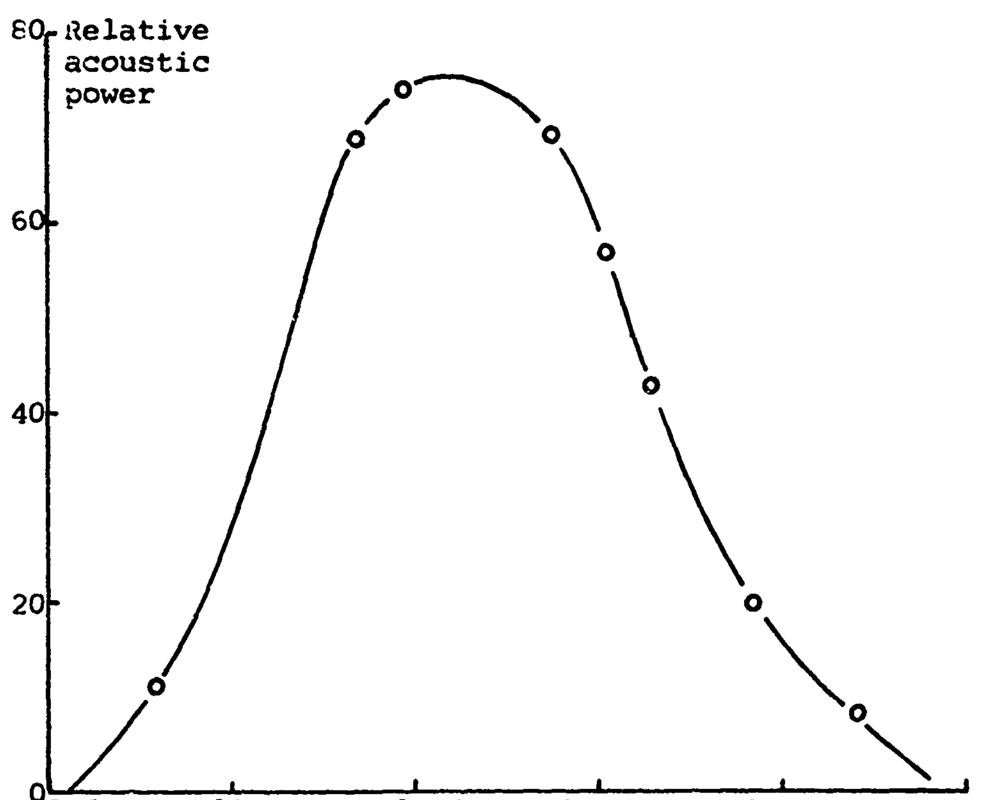

$= (1/2)\, \rho\, c\, (ka)^2$

$= .829$ newton-sec/m^3,

$k = 2\pi/\lambda$,

= the acoustic wavelength

= 25 m,

a = the tube radius

= .254 m,

a_p = the piston radius

= .238 m,

u_p = the piston velocity

= .269 m/s,

$R_b = \gamma L \rho c$,

= the dissipation resistance inside the tube due to air leakages, nonlinear effects, eddy and molecular viscosity, thermal conduction, wall flexibility, etc.

γ = the imaginary part of the propagation constant inside the tube,

L = the effective tube length

$= \lambda/4$.

The calculation results can be illustrated by the numbers listed in Table 2-1.1. The above theory does not explain the observed Q and power output of the transmitter. For an observed acoustic power output of 15 watts, the Q would be 42 instead of the observed 30, which corresponds to an output power of only 7.8 watts. The possible reasons for the

Table 2-1.1 The predicted quality factor, acoustic power, and acoustic pressure of the signal transmitter

Q	P_o (watt)	P_p (watt)	p_p (bar)
25	5.4	84	.035
30	7.8	100	.042
35	11	120	.050
42	15	140	.058
386	1290	1290	.54

Remarks:

Q = the quality factor

P_o = the open end acoustic power in resonance

P_p = the piston end acoustic power in resonance

p_p = the piston end acoustic pressure in resonance

discrepancy between the theory and observations are:

(1) The actual radiation resistance could be greater than what is assumed in the theory, which is derived for a flanged piston.

(2) Some unaccounted process in the system could have lowered the Q, without simultaneously lowering the power output.

(3) The sensitivity of the receiver microphone could be inaccurate so that the signal amplitude has been overestimated.

If there was no dissipation inside the tube, the Q would be 386, the resonant power output 1290 watts, and the acoustic pressure .54 bar, according to the theory. This seems to be not only impossible because of the large acoustic pressure (.54 bar) which could have caused nonlinear dissipation, but also impractical because of the large Q. With a Q of 386, the output power would decrease by 50% when the transmitter frequency deviates from the resonant frequency by .13%, which could easily be effected by an air temperature variation of only .8°C.

Two control modes of the signal transmitter are now available, i.e., resonance control mode, and frequency control mode. In the resonance control mode, the motor speed is fixed at resonance by controlling the piston velocity to be always in phase with the acoustic pressure at the bottom of the tube. Since the resonant frequency varies with the air temperature, the signal source under the resonance control mode does not necessarily have a constant frequency, and, as a result, is not suitable for studying doppler shifts produced by propagation in the atmosphere. In the frequency control mode, the motor speed is controlled to run at a constant frequency, which can be readjusted to be equal to the resonant frequency as the air temperature changes. With a Q of 30, the source power can often be kept within 10% of the resonant power by readjusting the motor speed once to thrice over a whole night. Even during periods with maximum time rates of change of the air temperature on a clear summer day, i.e., about ± 3°C per hour, the source power can still be kept within 15% of the resonant power by readjusting the motor speed once per hour. In this experiment, the frequency control mode was used almost exclusively. The electronic systems for the motor control at the transmitter and for the data processing at the receiver are very similar, both using phase lock amplifiers. A schematic diagram (Fig. 2-2.4) in the next section shows the major constituents of the entire probe. Details of the transmitter control should always be tried out to fit the special purpose, for which the received signal is processed. For example, in the last stage of this experiment, the received doppler shifts were integrated to directly record signal phase shifts originated by atmospheric turbulence (Section 2-2). To design the proper transmitter control for such an operation should minimize deviations of the integrated frequency error.

The transmitter frequency can usually be controlled to stay within .005% of the average frequency (Figs 2-1.2 and 2-1.3). Fig. 2-1.2 compares the source frequency and amplitude with the signal frequency and amplitude received on the ground, about 20 m away from the transmitter. The source frequency and amplitude were monitored by suspending a ceramic microphone near the piston end of the tube resonator. The sensitivity of the ceramic microphone has not yet been calibrated. Therefore, the source amplitude is expressed in an arbitrary scale. In Fig. 2-1.2, the frequency records of the transmitter and the receiver look almost identical, with the

Fig. 2-1.2 An example of source frequency and amplitude compared with receiver records (Y = 20m)

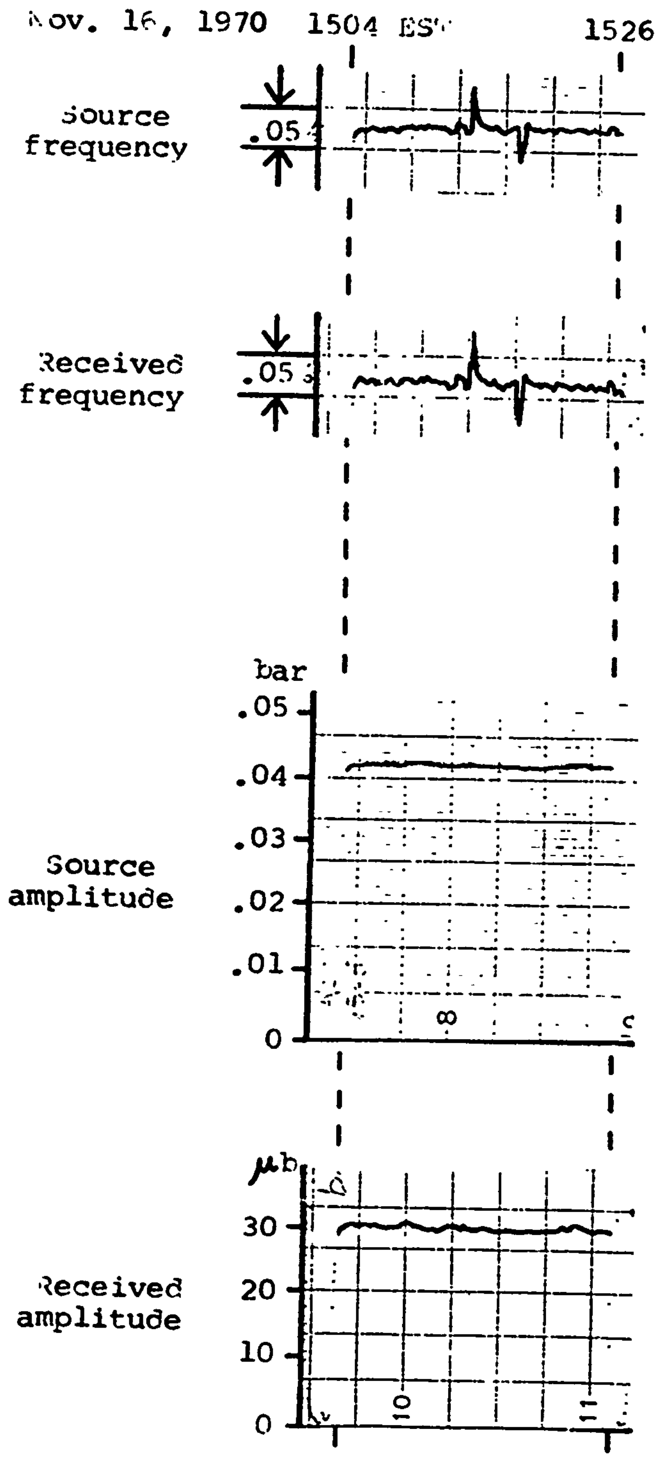

Fig. 2-1.3 An example of source frequency compared with receiver records (Y = 9200 m)

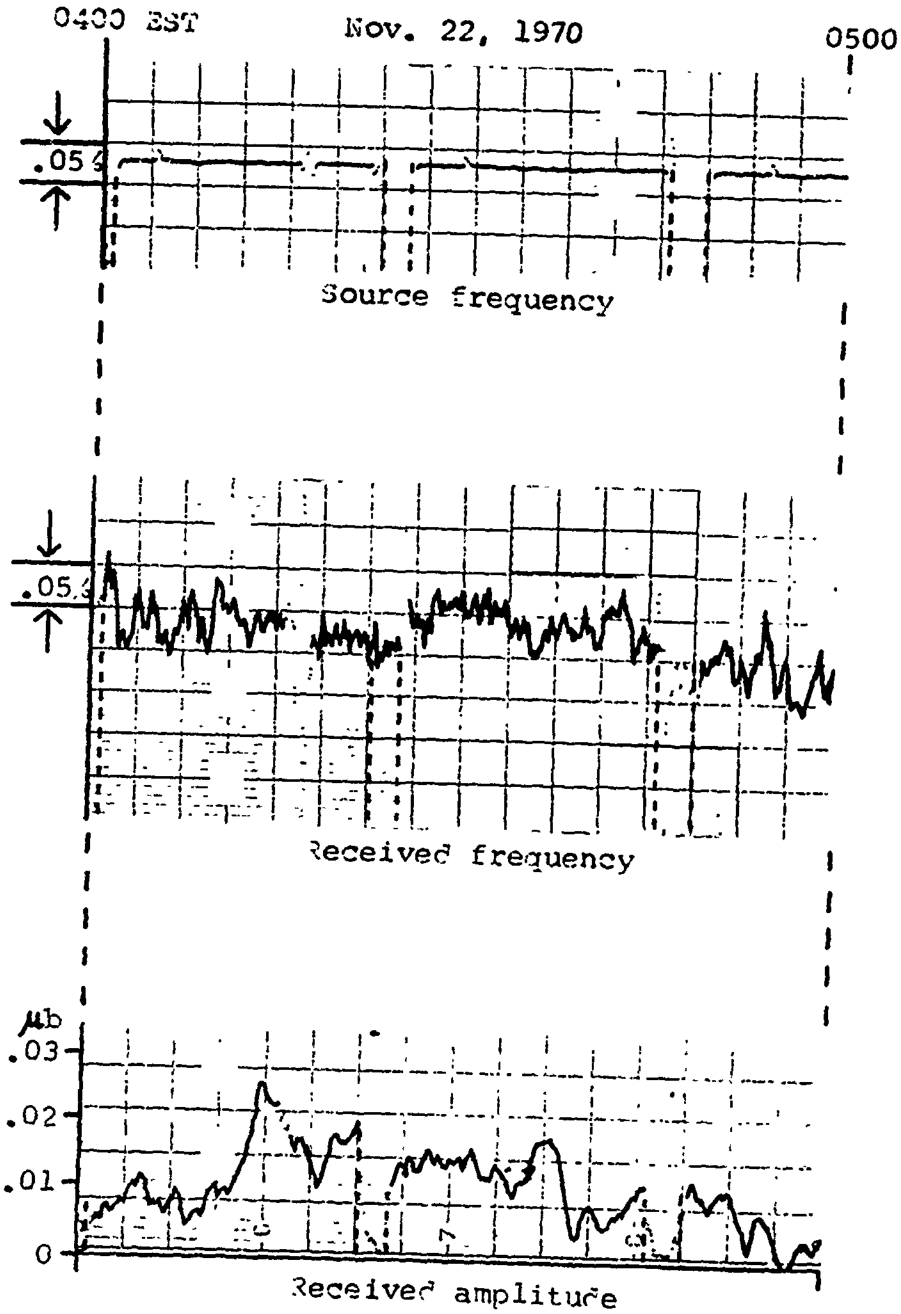

receiver so close to the source. Large deviations of the transmitter frequency can be caused by the wind blowing over the mouth of the acoustic resonator, electric surges in the power line to the transmitter control system, etc. Therefore, to interpret the received doppler (or phase) shifts, one should always first compare them with the source frequency record and count out any variations which are due to the source. Fig. 2-1.3 compares the source frequency with the signal frequency and amplitude, which were received 9200 m to the SE of the source. In order to determine the background noise, the transmitter was scheduled to be on for 22 min. and off for 2 min., with a cycle per 24 min. After being corrected for source frequency deviations, the received frequency variations can be either due to medium fluctuations or due to the background noise. Reliable doppler shifts, which are caused by wind and temperature fluctuations, can only be determined after one fully understands noise effects on the receiver behavior.

2-2. The signal receiver

The signal receiver includes three major components: a Globe microphone, a filter-amplifier and a phase lock system.

The Globe microphone is a sensitive capacitor microphone. Its frequency response is flat within 3 db from .1 cps to 450 cps. It has a sensitivity of .0225 $v/\mu b$. The microphone output is sent to the filter-amplifier.

The filter-amplifier had a 4 cps-bandwidth centered at 13.5 cps. Later the bandwidth was narrowed to 1 cps. Its amplification gain ranges from 10 to 5000. The filter output is rectified and averaged. This output is denoted as the A.C. level, which represents the total level of the signal and the noise within the 4 cps- or 1 cps-bandwidth. The filter output is also sent to the phase lock system.

The phase lock system phase-detects the signal against a relaxation oscillator. The phase error is integrated to produce a frequency error signal. This error signal is used to keep the relaxation oscillator in step with the signal and is also used as a monitor of the signal frequency. The relaxation oscillator also operates a synchronous detector through which the audio signal is passed. The output of this detector is averaged and denoted as the synchronous output. In a later stage, the error signal was integrated to give the phase shift of the received signal. The theoretical characteristics of the receiver phase lock loop are the following (Gardner 1967):

The effective bandwidth of synchronous output

= .05 cps.

The amplitude of synchronous output

= (signal amplitude) $\langle \cos(\theta_{noise}) \rangle$,

where (θ_{noise}) = the signal phase jitter due to noise.

The mean square phase jitter due to noise

$= (\theta_{noise})^2$

$= (P_{noise}) / (30\ P_{signal})$,

where (P_{noise}) = the noise power,

(P_{signal}) = the signal power.

The maximum doppler shift rate that can be tracked when

$(P_{signal}) > (P_{noise})$

= .012 cps/sec.

The minimum signal-to-noise ratio for lock

= 1/5.

The receiver has been constantly under improvement. For the experimental results presented in this work, one can distingnish three stages of the receiver condition:

1) From May 8 to Nov. 16 in 1970. the receiver had a wide band (4 cps) filter and recorded frequency shifts.

2) From Nov. 16 to Nov. 24 in 1970, the receiver had a narrow band (1 cps) filter and still recorded frequency shifts.

3) From Nov. 24, 1970 to Jan. 7, 1971, the receiver had a narrow band filter and recorded phase shifts.

The receiver characteristics are demonstrated in Figs. 2-2.1 to 2-2.3 for the three different stages. For signal-to-noise ratios of about 1, the frequency is steady over periods of more than 1 min., although over periods of less than 1 min., there are frequency fluctuations due to the noise. Therefore, the minimum signal-to-noise ratio for detecting frequency (or phase) shifts with periods longer than 1 min. is about unity for all three stages.

The entire probe system is schematically shown in Fig. 2-2.4.

Fig. 2-2.1 Receiver characteristics
(4 cps-bandwidth and doppler shifts)

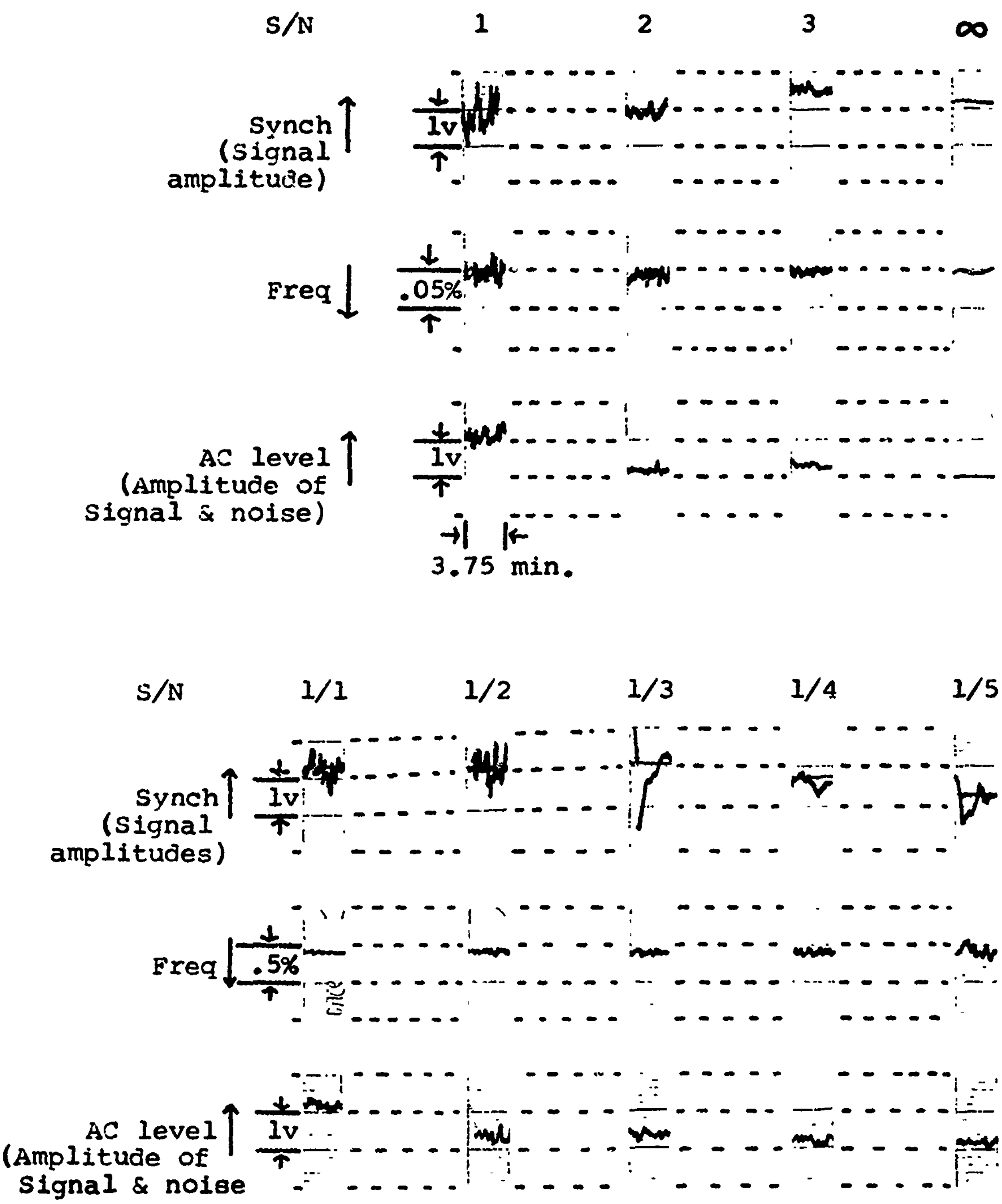

Fig. 2-2.2 Receiver characteristics
(1 cps-bandwidth and doppler shifts)

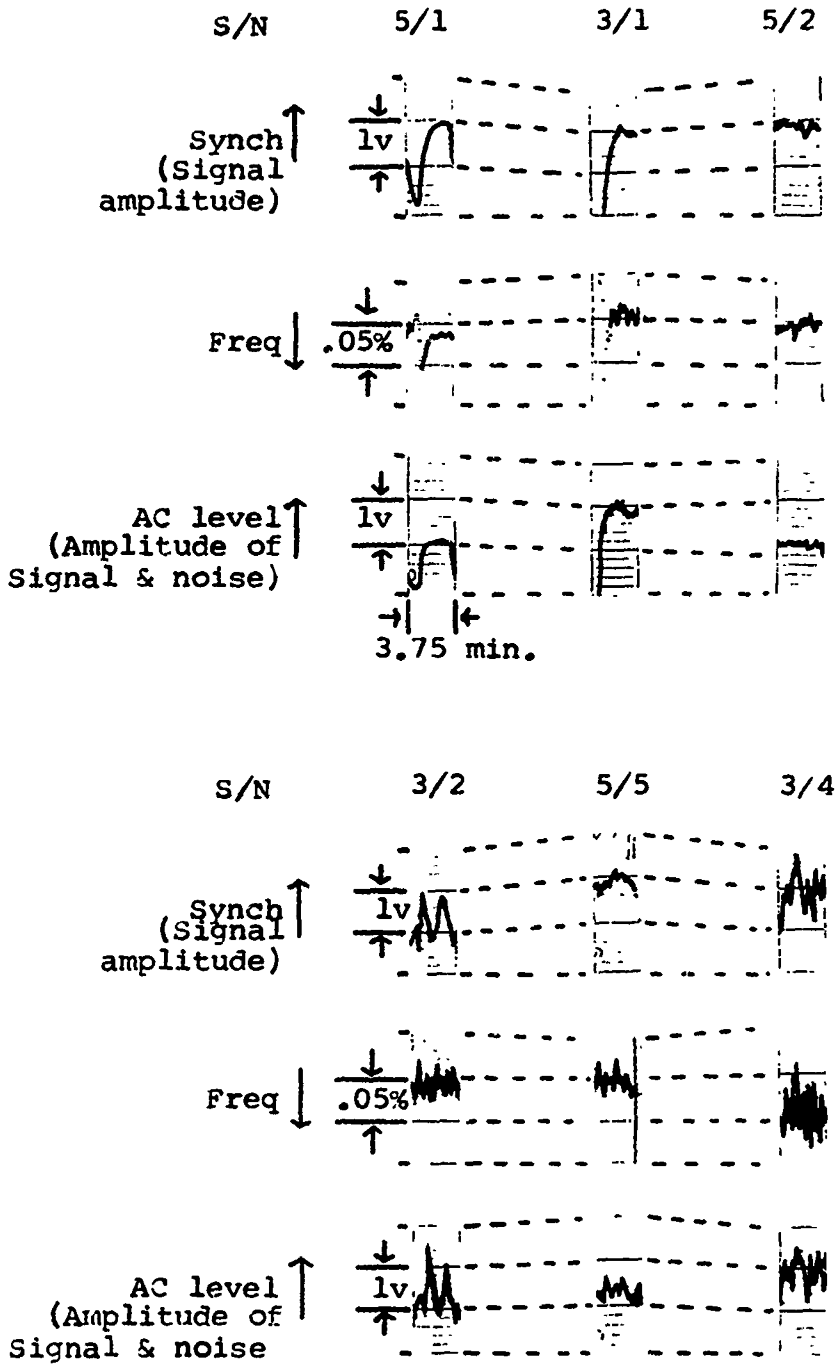

Fig. 2-2.3 Receiver characteristics
(1 cps-bandwidth and phase shifts)

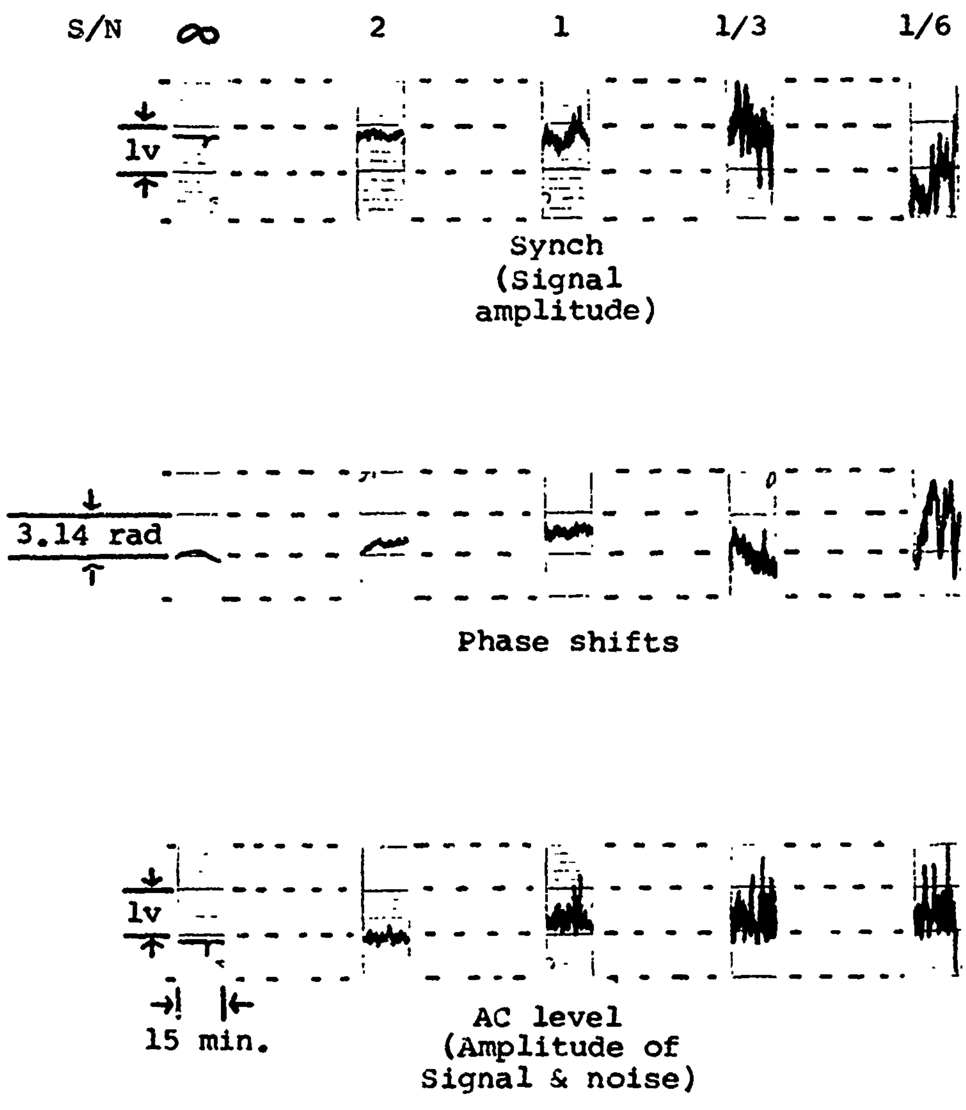

Fig. 2-2.4 Flow diagram of the probe

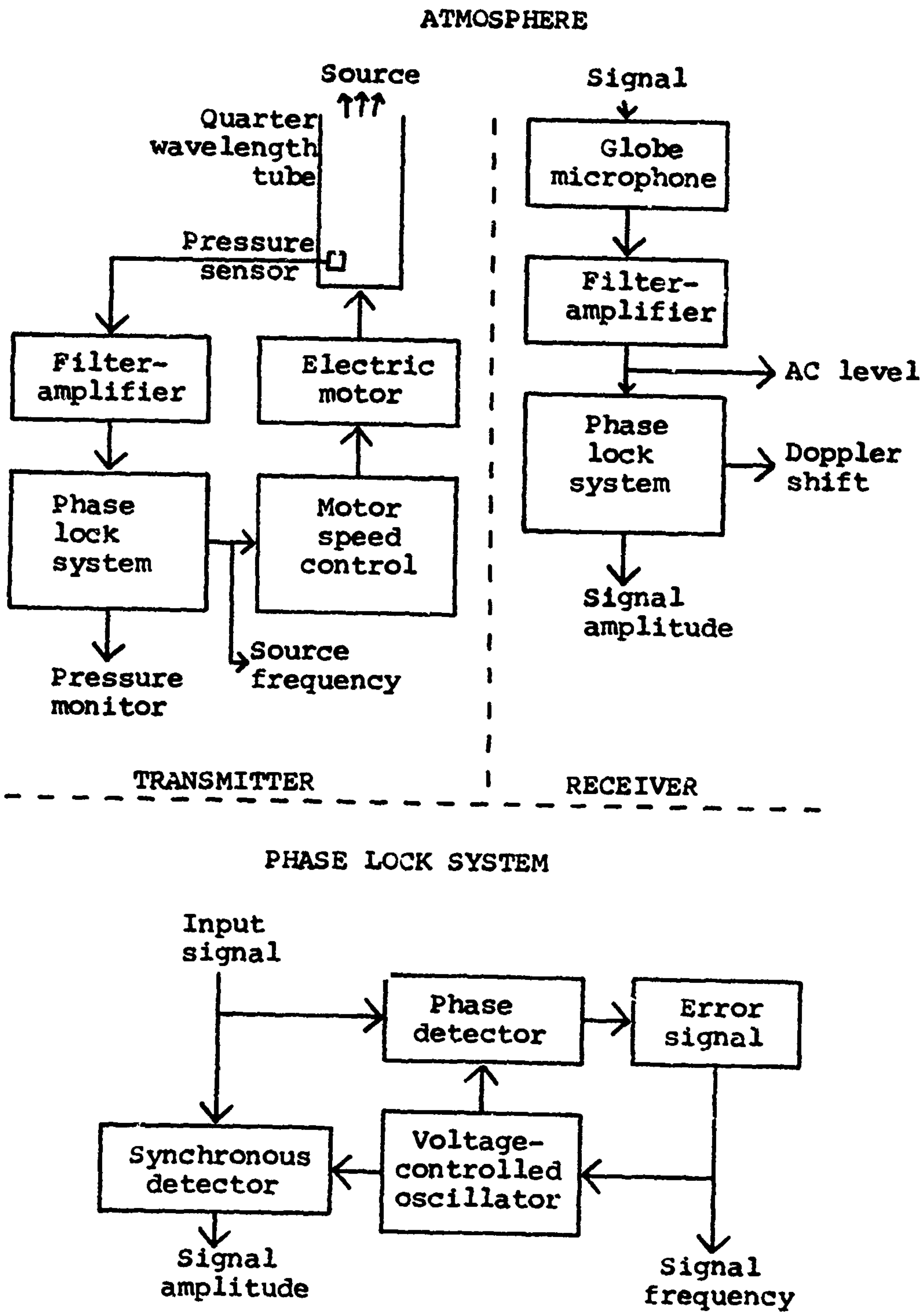

2-3. Wind screens and the Daniels pipe for improving the signal-to-noise ratio at the receiver

The improvement of the signal-to-noise ratio at the receiver is imperative in carrying out the experiment successfully. In addition to the electronic phase lock technique, which proves to be unique in tracking the signal, some mechanical devices are still necessary to reduce the background noise at the receiver. There are two kinds of background noise: the random noise and the acoustic noise. The random noise is mainly caused by the local wind. The acoustic noise is mainly caused by the high speed automobile traffic. Wind sreens made of silk can reduce the wind noise by inhibiting the air flow. A Daniels pipe (Daniels 1959) with wind screens can reduce both random and acoustic noises.

A portable wind screen made of two cylindrical silk layers, one outside the other, has been used for exploratory field trips. The outer cylinder is 2 feet high and 2.5 feet in diameter, and the inner one is 1.5 feet high and about 1 foot in diameter. The exact gain of the wind screen is yet to be measured. The noise reducing capability seems to depend on the wind speed. The signal is unattenuated by the screen.

The Daniels pipe, which acts as a line microphone, is a plastic pipe 25 meters long with an inside diameter of 1 inch. One end of the pipe is fitted to the Globe microphone of the receiver, and the other end pointed at the signal source. Evenly distributed along the pipe are 25 leaks, which are made of capillary tubes of different sizes. The leaks at the source end of the pipe have larger diameters and smaller lengths than the leaks at the microphone end, so that the waves coming through all the leaks will arrive at the microphone with approximately the same amplitude. The sound speed in the pipe is equal to that in the air. Therefore, for the signal travelling in the direction of the pipe, each leak admits a wave which is in phase with the waves from all the other leaks. The wind noise, however, because of its limited spacial coherence is incoherently summed in the pipe. Also the acoustic noise coming from other directions is attenuated because the waves picked up at different leaks are out of phase. The theoretical amplitude response as a function of the direction is shown in Fig. 2-3.1 (Olson 1947, p. 280). The Daniels pipe as well as the Globe microphone are buried and the leaks are covered with small wind screens. This system reduces the background noise by a factor of about 3. The signal is essentially unattenuated by the Daniels pipe.

Fig. 2-3.1 The amplitude response curve of the Daniels pipe (Length = 1 λ)

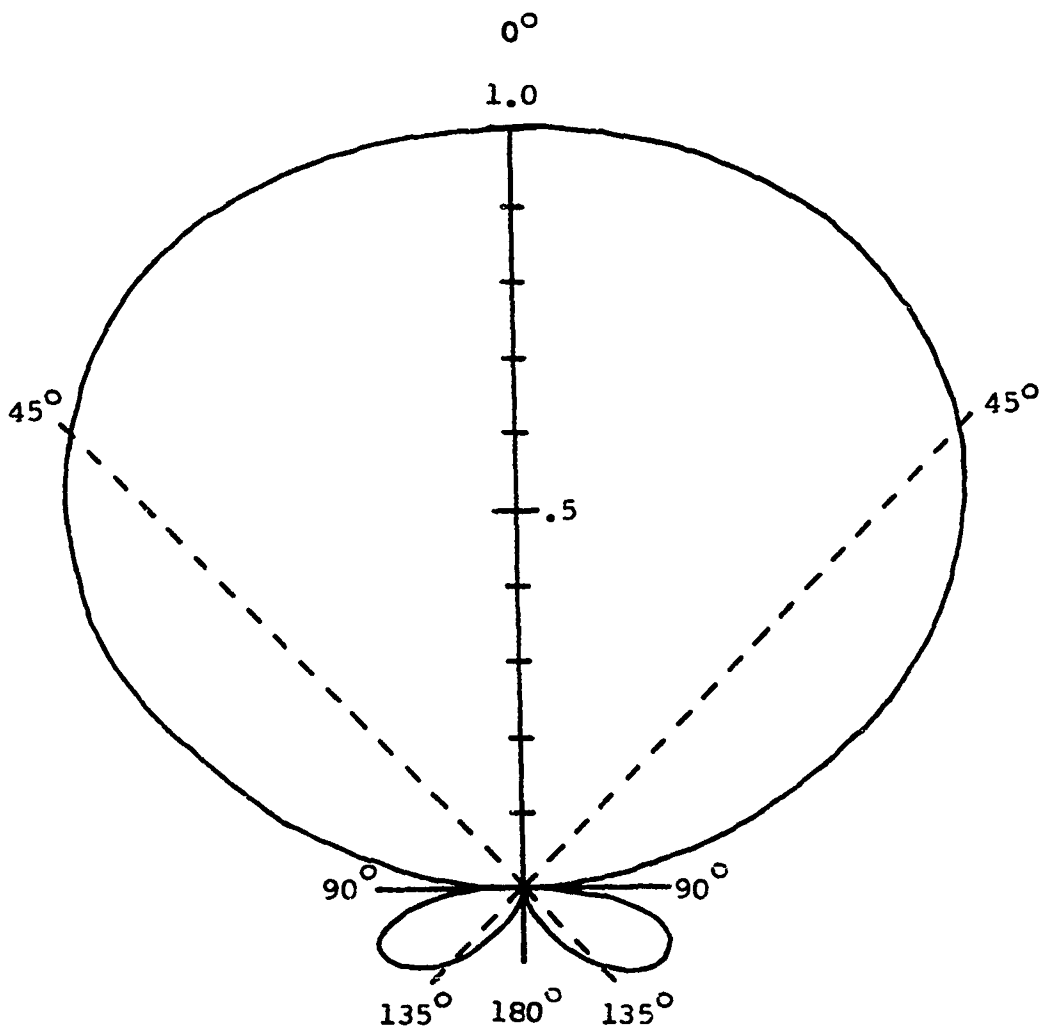

The radial distance to the curve is the amplitude response normalized by the 0° response to the acoustic wave coming in that direction.

CHAPTER 3. A RAY THEORY FOR SIGNAL PROPAGATION IN THE ATMOSPHERIC BOUNDARY LAYER

A simple ray theory is developed to analyze the field data of the experiment. With horizontal travel distances of 5 to 10 km, the signal penetrating height is limited by the atmospheric boundary shear, which is 200 to 600 m thick. Because of the small elevation angles of the propagating ray ($\alpha < .3$ rad.), the theory adopts a shallow angle approximation. One-dimensional effective wind profiles are proposed to interpret long-period signal amplitude variations with periods of .5 to 6 hours. From these models, the average ray trajectories and penetrating heights can be estimated. Superposed on the long-period atmospheric variations are short-period wind and temperature fluctuations with periods of .5 to 8 min., which cause short-period amplitude variations and phase (or doppler) shifts. Horizontal wind fluctuations and turbulence scales can be inferred from the short-period signal variations by a three-dimensional fluctuation model.

The first section of this chapter (Section 3-1) summarizes the general ray theory, whose details can be found in Hayes (1970) and Lighthill (1965). Section 3-1 also discusses various signal attenuating processes in the atmosphere, different ways of evaluating ray integrals, and finally the multipath ray interference. Section 3-2 introduces one-dimensional atmospheric models and the shallow angle approximation. These help simplify the algebra of integrations. Section 3-3 presents fundamental effective wind profiles which are suggested from the long-period experimental results (Section 4-4). Section 3-3 also summarizes the ray characteristics of these fundamental profiles. Section 3-4 is a linear theory of profile fluctuations which illustrates the relation between amplitude variations and doppler shifts. Section 3-5 deals with signal variations due to short-period wind fluctuations.

3-1. Ray theory

The important results of general ray theory can be summarized in the following three statements.

a) The group velocity, which describes the ray trajectory, is the gradient of frequency with respect to wave vector in the augmented space (Hayes 1970). The augmented space, which comprises wave vector $\vec{k}$, position vector $\vec{r}$, and time t, is distinguished from the propagation space ($\vec{r}$, t). The frequency in the augmented space is denoted by $\Omega(\vec{k}, \vec{r}, t)$, and that in the propagation space by $\omega(\vec{r}, t)$. The dispersion relation is then

$$\omega = \Omega(\vec{k}, \vec{r}, t), \tag{1a}$$

which, for the acoustic wave in a moving medium, is

$$\omega = kC + \vec{k}\cdot\vec{V}, \tag{1b}$$

where C = sound speed,

$\vec{V}$ = wind,

and both C and $\vec{V}$ are functions of $\vec{r}$ and t. Therefore the acoustic group velocity is

$$\frac{d\vec{r}}{dt} = \vec{n}C + \vec{V}, \tag{2}$$

where $\vec{n}$ = unit wave vector.

b) The time derivative of wave vector along the ray is the negative gradient of frequency with respect to position vector in the augmented space, i.e.,

$$\frac{d\vec{k}}{dt} = -\Omega_r, \tag{3}$$

where $\frac{d}{dt} = \frac{\partial}{\partial t} + \frac{d\vec{r}}{dt} \cdot \nabla_r$.

c) The time derivative of frequency along the ray is the partial derivative of frequency with respect to time in the augmented space, i.e.,

$$\frac{d\omega}{dt} = k \frac{\partial c}{\partial t} + \vec{k} \cdot \frac{\partial \vec{V}}{\partial t} . \quad (4)$$

The coordinate system used for the probe is illustrated in Fig. 3-1.1. The wave vector magnitude and components are,

$$k = \frac{\omega}{C + V_x \cos\alpha \cos\beta + V_y \cos\alpha \sin\beta + V_z \sin\alpha}, \quad (5)$$

$$k_x = k \cos\alpha \cos\beta ,$$

$$k_y = k \cos\alpha \sin\beta ,$$

$$k_z = k \sin\alpha .$$

The signal amplitude is calculated by considering the geometrical spreading of the rays. The doppler shift, which is usually less than .1% of the source frequency, can be neglected in evaluating ray trajectories. The apparent source power is 4 times the real power output, P, of the signal transmitter because of the ground reflection at the receiver (Section 2-1). Then the power emitted in the solid angle element $\cos\alpha_o \, d\alpha_o \, d\beta_o$ is $(P/\pi) \cos\alpha_o \, d\alpha_o \, d\beta_o$, which, according to the law of energy conservation, should be equal to $[p^2/(2\rho c)] \left| \vec{n} \cdot \frac{\partial \vec{R}}{\partial \alpha_o} \times \frac{\partial \vec{R}}{\partial \beta_o} \right| d\alpha_o \, d\beta_o$ at the receiver, where p is the peak amplitude of acoustic pressure, ρ the air density, and $\left| \vec{n} \cdot \frac{\partial \vec{R}}{\partial \alpha_o} \times \frac{\partial \vec{R}}{\partial \beta_o} \right| d\alpha_o \, d\beta_o$ the cross-section of

Fig. 3-1.1 The coordinate system used for the probe

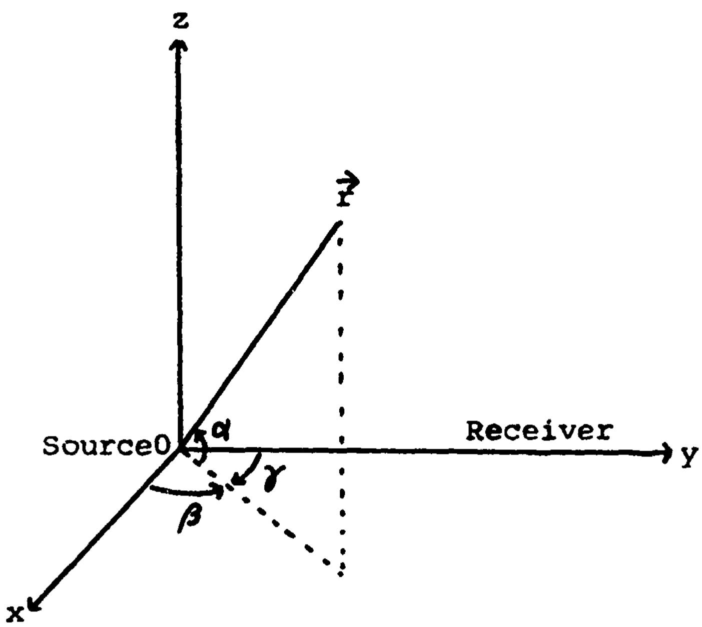

Remarks:

Source at (0, 0, 0)
Receiver at (0, Y, 0)
x = the axis perpendicular to the source-receiver line
v = the coordinate along the source-receiver line
z = the vertical coordinate
α = the elevation angle
$\gamma = \pi/2 - \beta$

the ray tube. Hence the signal peak amplitude is

$$p = \left[2P\rho c \cos\alpha_o / (\pi \left| \vec{n} \cdot \frac{\partial\vec{R}}{\partial\alpha_o} \times \frac{\partial\vec{R}}{\partial\beta_o} \right|) \right]^{\frac{1}{2}}. \qquad (6)$$

A convenient way to express the signal amplitude received away from the source is to specify its focusing factor, which is defined as the ratio of the actual amplitude to the amplitude one would receive if the medium was uniform and the signal could propagate along a straight line, i.e.,

$$f = R \Big/ \left| \vec{n} \cdot \frac{\partial\vec{R}}{\partial\alpha_o} \times \frac{\partial\vec{R}}{\partial\beta_o} \right|^{\frac{1}{2}}. \qquad (7)$$

The signal can be attenuated by other processes than the geometrical spreading, which are, in the order of importance to this experiment: vibrational relaxation of atmospheric molecules, turbulence scattering, relaxation effects of fogs, and classical absorption due to viscous forces and heat conduction. The amplitude attenuation caused by these processes is estimated according to theoretical studies and laboratory tests reported in the literature.

The major signal-attenuating relaxation process in the atmosphere is due to the vibrational mode of oxygen molecules (Kneser 1965). The water vapor content decisively controls the absorption as shown in Fig. 3-1.2. For example, the maximum amplitude loss of 33% over a 9.2 km path occurs approximatly at -10^{o}C with a relative humidity of 100%, at 0^{o}C with a relative humidity of 50%, or at 10^{o}C with a relative humidity of 20%.

Fig. 3-1.2 Sound attenuation due to the vibrational relaxation of atmospheric molecules (Y = 9200 m, frequency = 13.5 cps)

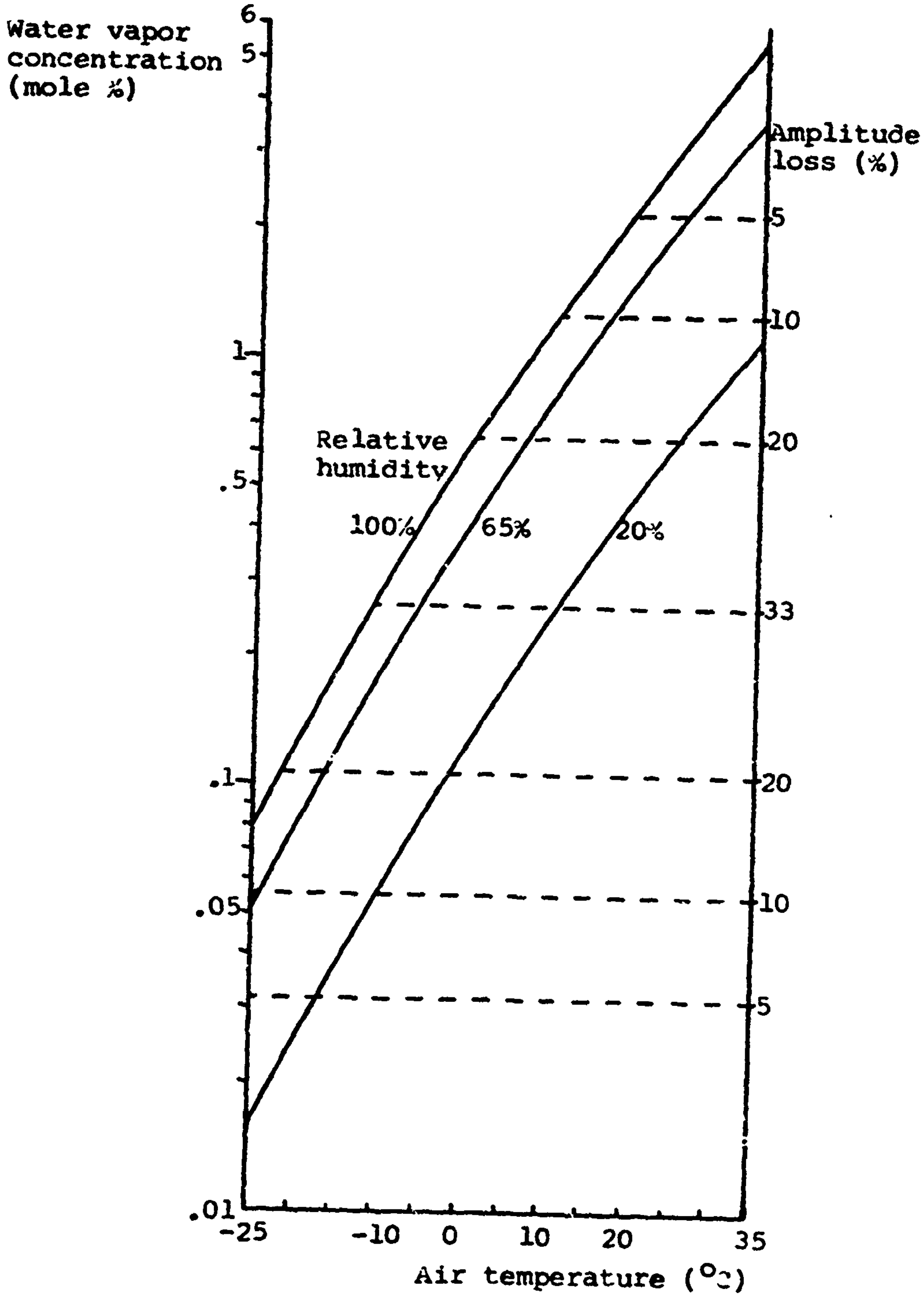

The amplitude loss due to turbulence scattering depends on the intensity of boundary turbulence, which can be estimated from the 3 m-level wind fluctuation. The estimated signal amplitude losses for three turbulent conditions are listed in Table 3-1.1. For a travel distance of 9.2 km, the signal amplitude can lose 17% in a severe turbulence (i.e., with a rms wind fluctuation of 1.5 m/s at 3 m).

The signal is attenuated in fogs because of an irreversible energy transfer from the signal wave to water droplets and the saturated air, similar to the relaxation attenuation by molecular vibrational modes. According to a theoretical study by Cole and Dobbins (1970), the energy attenuation of waves with frequencies less than 130 cps is about 8×10^{-4} neper/m when the visibility in the fog is 24 m. Therefore the amplitude loss over 9.2 km in a dense fog will be almost total. This might have actually happened to the probing signal in the night of Oct. 9-10, 1970, when the signal amplitude received at the 9.2 km site gradually vanished as the visibility in the fog decreased to about 24 m. However the loss of signal that night could also be interpreted as due to the loss of wind shear which was recorded. The rest of the field data analyzed in this work was collected without significant fogginess.

The amplitude loss due to viscous forces and heat conduction of the air is estimated to be about only .003% over a 9.2 km path (Piercy 1969), and is, therefore, unimportant.

Table 3-1.1 Signal amplitude loss due to turbulence scattering

σ_V	(m/s)	.5	1.	1.5
ε	(m^2/s^3)	.0013	.0053	.012
Signal amplitude loss	(Y = 4.5 km)	2%	5%	9%
	(Y = 9.2 km)	4%	10%	17%

Remarks:

1. σ_V = the rms wind fluctuation at 3 m-level.
2. ε = the turbulent energy dissipation rate.

   $= u^{*2} \frac{\partial V}{\partial z}$,

   where u^* = the friction velocity

   $= \sigma_V/2.5$,

   and $\frac{\partial V}{\partial z}$ = the vertical wind shear

   $= .033\ \text{sec}^{-1}$.
3. Y = the travel distance.
4. The signal amplitude loss is estimated by assuming a homogeneous isotropic turbulence with outer scale of 200 m, a temperature of 10°C, and turbulent energy dissipation rates estimated above. The formulas can be found in Batchelor (1957) and Tatarski (1961).

To evaluate the ray trajectory and the ray parameters, e.g., $\vec{R}$, $\vec{k}$, ω, $\frac{\partial \vec{R}}{\partial \alpha_o}$ and $\frac{\partial \vec{R}}{\partial \beta_o}$, there are three different ways of integration. They are time-integration, z-integration, and y-integration.

Time-integration, as described by Wesson (1970), is suitable in numerical calculation.

Z-integration is preferred for obtaining analytical expressions, when atmospheric parameters are assumed to be functions of z only. Since Ω is now not an explicit function of x and y, one gets from Eq. (3)

$$k_x = k_{ox} = \text{constant,} \tag{8a}$$

and $$k_y = k_{oy} = \text{constant,} \tag{8b}$$

for each ray. Also as a matter of fact, the doppler shift is usually less than .1% of the source frequency. Therefore, the frequency can be practically considered as constant when ray trajectories are evaluated, i.e.,

$$\omega = \omega_o = \text{constant.} \tag{9}$$

From Eqs. (8) and (9), the Snell's law in a moving medium is obtained as

$$\frac{c}{\cos\alpha} + v_y = \frac{c_o}{\cos\alpha_o} + v_{yo}. \tag{10}$$

The vertical component of the wind, V_z, is negligible in determining the ray trajectory. Z-integration is used in Sections 3-2 through 3-4.

Y-integration is preferred for calculating the root-mean-square value of signal variations due to random medium fluctuations and is, therefore, used in Section 3-5.

One should beware of the possiblity of receiving multi-path rays. For example, with a two-layer atmosphere model, one often predicts two rays with different initial elevation angles landing at the same receiving site (Fig. 3-3.4). The multi-path rays could interfere with each other. However, from the experimental results (Chapter 4), one finds that the multi-path ray interference is negligible in this experiment. There are two reasons for this:

(a) Firstly, observed phase shifts (in radians) are mostly much greater than observed fractional amplitude variations (Tables A-1.1 to A-1.9), while, for the multi-path ray interference, one would predict phase shifts to be only slightly greater than or equal to fractional amplitude variation. For example, one considers the interference of two rays with amplitudes respectively of 1 and r, where r is smaller than 1. Their phase difference is assumed to vary randomly between 0 and 2π. Then, according to vector summation, one gets the rms phase shift as

$$\sigma_{\phi} = (r / 2^{\frac{1}{2}})\ (1 + r^2 / 8),$$

and the rms fractional amplitude variation as

$$\sigma_p/\bar{p} = (r / 2^{\frac{1}{2}})\ (1 - r^2 / 32).$$

Hence, for the double ray interference, phase shifts are predicted to be only slightly greater than fractional amplitude variations. When the number of interfering rays becomes infinitely large, the signal variations could possibly be predicted by the diffraction theory for signal propagation in a random medium (Tatarski 1961, p. 185), and phase shifts likely tend to be equal to fractional amplitude variations. However, experimental results give phase shifts to be mostly much greater than fractional amplitude variations (Fig. 3-1.3). In average, phase shifts are measured to be twice as large as fractional ampliutde variations. Therefore, the multi-path ray interference seems to be negligible in this experiment.

(b) Secondly, because of the topography of the experiment site (Fig. 4.1), rays reflected from the ground surface at closer distances often restart with greater elevation angles than their trapping angles, and are unlikely to bend down again so as to interfere with the direct ray at the receiver.

Therefore, to the first approximation, one can neglect the interference of multi-path rays, and consider only one direct ray.

Due to atmospheric inhomogeneities, the receiver can also have scattered rays, which interfere with the direct ray and cause diffraction. One will see in Section 4-1. that the field data of this experiment can still be analyzed by the ray theory and that the effect of diffraction phenomena on these results can be estimated. The horizontal wind fluctuation inferred with the ray theory is possibly smaller than

Fig. 3-1.3 Observed amplitude and phase variations

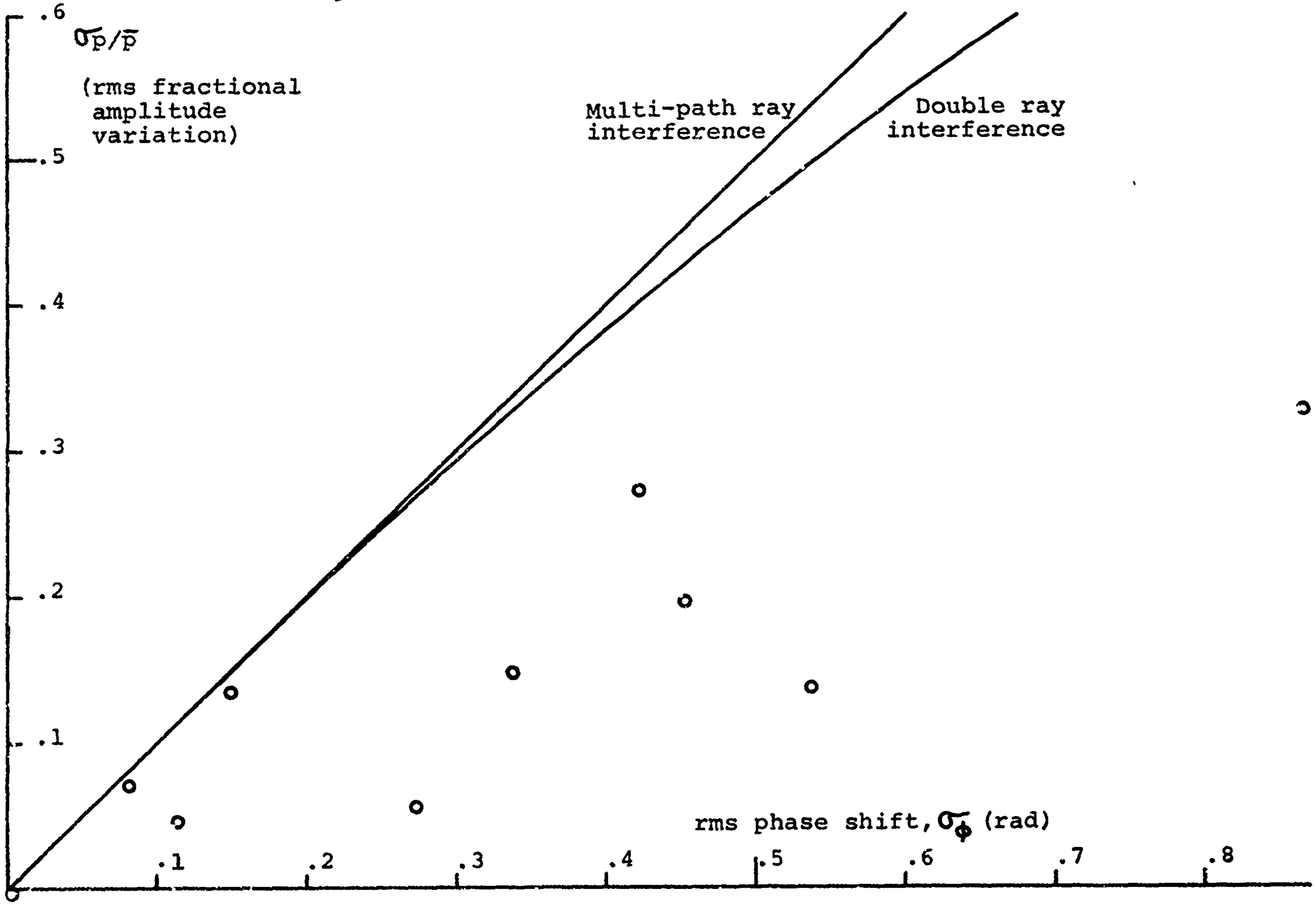

the true value by 33%. The accuracy of inferring the vertical turbulence scale with the ray theory is generally good except for a few cases where the phase shift is almost equal to the fractional amplitude variation.

3-2. One-dimensional atmospheric model and shallow angle approximation

Atmospheric temperature and wind are mainly functions of height. Therefore, to study average signal amplitude and long-period signal variations, a one-dimensional model can be used. The signal penetrating height depends on the wind shear and the temperature gradient in the atmospheric boundary layer as well as the source-receiver distance. With a horizontal travel distance of 9.2 km, the signal penetrates almost to the top of the boundary shear, which is 200 m to 600 m above the surface. The signal ray angle, α, which the ray makes with the horizontal surface, is always small (less than .3 rad). To take advantage of this fact, a shallow angle approximation is used in evaluating ray integrals.

As a result of one-dimensional model and shallow angle approximation, one can write

$$\cos\alpha = 1 - \alpha^2/2, \tag{1a}$$

$$\cos\alpha_o = 1 - \alpha_o^2/2, \tag{1b}$$

and

$$1/C = 1/C_o - (C-C_o)/C_o^2, \tag{1c}$$

by Taylor's expansion and retaining terms up to the first order. Then the substitution of Eqs. (1) into Eq. (10) in the previous section transforms the Snell's law into the simplified form

$$\alpha^2 = \alpha_o^2 - 2\,(C - C_o + V_y - V_{yo})/C_o, \tag{2a}$$

where the subscript "o" denotés the ground value.

By defining the effective wind as

$$V_e = C - C_o + V_y - V_{yo}, \tag{2b}$$

the Snell's law is conveniently written as

$$\alpha^2 = \alpha_o^2 - 2V_e/C_o . \tag{3}$$

Then the integral of ray trajectory becomes

$$\begin{aligned} y &= \int_o^z (dz/\alpha) \\ &= \int_o^z \left\{ dz \Big/ \left[\pm \left(\alpha_o^2 - 2\, V_e/C_o \right)^{\frac{1}{2}} \right] \right\}, \end{aligned} \tag{4}$$

where α is positive in the first half trajectory (from the source to the turning point) and is negative in the second half trajectory (from the turning point to the landing point). The penetrating height, H, is the value of z which makes α vanish.

Let the receiver location be y = Y and z = Z = 0. Then the horizontal travel distance is

$$\begin{aligned} Y &= 2 \int_o^H (dz/\alpha) \\ &= 2 \int_o^H \left[dz/\left(\alpha_o^2 - 2\, V_e/C_o \right)^{\frac{1}{2}} \right], \end{aligned} \tag{5}$$

where H = the signal penetrating height.

The ray propagation height averaged over the horizontal travel distance is called the average ray height, i.e.,

$$H_{av} = (2/Y) \int_o^{Y/2} z\,dy = (2/Y) \int_o^H (z\,dz/\alpha). \tag{6}$$

The amplitude and focusing factor with the shallow angle approximation become respectively

$$p = \left[2P\rho c / \left(\pi\, \alpha_o\, Y \left| \frac{\partial Y}{\partial \alpha_o} \right| \right) \right]^{\frac{1}{2}}, \qquad (7)$$

and $$f = \left[Y \Big/ \left(\left| \frac{\partial Y}{\partial \alpha_o} \right| \alpha_o \right) \right]^{\frac{1}{2}}. \qquad (8)$$

3-3. Fundamental effective wind profiles in the atmospheric boundary layer

The diurnal variations of the average signal amplitude (see Section 4-5 for the experimental evidence) suggest 6 fundamental effective wind profiles which are applicable in different times of the day. They are:

1) The negative shear profile.

$$V_e = - Sz, \tag{1}$$

where S is a positive constant. It occurs from about noon until sunset. No signal transmission is possible with this profile.

2) The parabolic profile.

$$\begin{aligned} V_e &= (2V_m\, z/z_m)\,[1 - z/(2z_m)] \\ &= S_o\, z\,[1 - z/(2z_m)]\,, \end{aligned} \tag{2}$$

where z_m = the shear vanishing height,

V_m = the wind at z_m,

S_o = the surface shear.

It is applicable mostly at night, when the penetrating height is close to the shear vanishing height and the focusing factor is small. The parabolic profile can be derived by Taylor's expansion of the effective wind at the shear vanishing height, i.e.,

$$V_e = V_m + \left.\frac{d^2\, V_e}{dz^2}\right|_{z_m} (z - z_m)^2. \tag{3}$$

Since the effective wind vanishes at the surface, the coefficient of the second term is determined as

$$\left.\frac{d^2 V_e}{dz^2}\right|_{z_m} = - V_m/z_m^2, \qquad (4)$$

which is a negative curvature. Then the substitution of Eq. (4) into Eq. (3) gives Eq. (2).

3) The logarithmic profile.

$$V_e = V_\ell \ \ln (z/z_o) \qquad (5)$$

where z_o = roughness length = 1 m,

V_ℓ = the wind at 3 m-level.

This profile is predicted assuming a strong turbulent boundary shear in neutral air (Lumley & Panofsky 1964, pp.103, Thuillier & Lappe 1964). It is applicable for short-distance propagation ($Y \lesssim 2$ km) in the daytime and for longer distances at night. The focusing factor is usually small.

4) The linear profile.

$$V_e = Sz. \qquad (6)$$

It is applicable at night, when the penetrating height is in the lower part of a strong boundary shear and the focusing factor is about 1.

5) The positive curvature profile. This has three types according to the surface shear, which can be positive, zero, or negative.

$$V_e = S_o z \left[1 + z/(2z_p) \right], \qquad \text{(Type a)} \qquad (7a)$$

$$V_e = S_o z^2/(2z_p), \qquad \text{(Type b)} \qquad (7b)$$

$$V_e = S_o\, z \left[-1 + z/(2z_p) \right], \qquad \text{(Type c)} \qquad (7c)$$

where S_o/z_p is the curvature and the surface shears are $+ S_o$, 0 and $- S_o$. These profiles are applicable when the signal penetrates the lower part of strong boundary shears. The focusing factor is greater than 1.

6) The elevated shear profile. This is a two-layer model. The lower layer is one of the positive curvature profiles, while the upper layer is a shear with negative curvature. The interface of the two layers is an inflection point. The elevated shear is believed to be responsible for the strong signals which are observed in the beginning as well as at the end of the daily receiving period (Fig. 4-4.1).

The signal properties for parabolic, logarithmic, linear, and positive curvature profiles can be evaluated analytically (Appendix 2). The results are shown below with

Y = the travel distance,

H = the penetrating height,

H_{av} = the average ray height, and

f = the focusing factor.

PARABOLIC PROFILE

Trajectory:

$$z = z_m \left[(\alpha_o/\alpha_m) \sinh (\alpha_m y/z_m) + 1 - \cosh (\alpha_m y/z_m) \right]$$

$$Y = (2z_m/\alpha_m) \tanh^{-1} (\alpha_o/\alpha_m)$$

$$H = z_m \left\{ 1 - \left[1 - (\alpha_o/\alpha_m)^2 \right]^{\frac{1}{2}} \right\}$$

$$H_{av} = z_m \left[1 - (\alpha_o/\alpha_m)/\tanh^{-1} (\alpha_o/\alpha_m) \right]$$

$$f = \left[\frac{\alpha_m Y}{2z_m} \right]^{\frac{1}{2}} \left\{ \coth \left[\frac{\alpha_m Y}{2z_m} \right] - \tanh \left[\frac{\alpha_m Y}{2z_m} \right] \right\}^{\frac{1}{2}}$$

$$\alpha_m = (S_o\, z_m/C_o)^{\frac{1}{2}} = (2\, V_m/C_o)^{\frac{1}{2}}$$

LOGARITHMIC PROFILE

Trajectory:

$$y = \left[\pi^{\frac{1}{2}} z_o \exp (G_o^2)/\alpha_\ell \right] \left[\text{erf} (G_o) \mp \text{erf} (G) \right]$$

$$Y = 2\ \pi^{\frac{1}{2}} z_o \exp (G_o^2) \text{ erf } (G_o)/\alpha_\ell$$

$$H = z_o \exp (G_o^2)$$

$$H_{av} = z_o \exp (G_o^2) \text{ erf } (2^{\frac{1}{2}} G_o)/ \left[2^{\frac{1}{2}} \text{ erf } (G_o) \right]$$

$$f = \left\{ \frac{\pi^{\frac{1}{2}} \exp (G_o^2) \text{ erf } (G_o)}{2\, G_o \left[1 + \pi^{\frac{1}{2}} G_o \exp (G_o^2) \text{ erf } (G_o) \right]} \right\}^{\frac{1}{2}}$$

$$G_o = \alpha_o\, C_o^{\frac{1}{2}}/(2\, V_\ell)^{\frac{1}{2}}$$

$$\alpha_\ell = (2\, V_\ell /C_o)^{\frac{1}{2}}$$

$$G = \left[G_o^2 - \ln (z/z_o) \right]^{\frac{1}{2}}$$

LINEAR PROFILE

Trajectory:

$$(y - C_o \alpha_o/S)^{\frac{1}{2}} = (2\, C_o/S) \left[C_o \alpha_o^2/(2S) - z \right]$$

$$Y = 2\, C_o \alpha_o/S$$

$H_{av} = (2/3)\ H$

$f = 1$

POSITIVE CURVATURE TYPE A (positive surface shear)

Trajectory:

$$z = z_p \left[(\alpha_o/\alpha_p) \sin (\alpha_p y/z_p) - 1 + \cos (\alpha_p y/z_p) \right]$$

$$Y = (2\ z_p/\alpha_p) \tan^{-1} (\alpha_o/\alpha_p)$$

$$H = z_p \left\{ \left[1 + (\alpha_o/\alpha_p)^2 \right]^{\frac{1}{2}} - 1 \right\}$$

$$H_{av} = z_p \left[(\alpha_o/\alpha_p)/\tan^{-1} (\alpha_o/\alpha_p) - 1 \right]$$

$$f = \left[\frac{\alpha_p Y}{2\ z_p} \right]^{\frac{1}{2}} \left\{ \cot \left[\frac{\alpha_p Y}{2\ z_p} \right] + \tan \left[\frac{\alpha_p Y}{2\ z_p} \right] \right\}^{\frac{1}{2}}$$

$$\alpha_p = (S_o\ z_p/C_o)^{\frac{1}{2}}$$

POSITIVE CURVATURE TYPE B (zero surface shear)

Trajectory:

$$z = (\alpha_o\ z_p/\alpha_p) \sin (\alpha_p y/z_p)$$

$$Y = \pi\ z_p/\alpha_p$$

$$H = \alpha_o\ z_p/\alpha_p$$

$$H_{av} = (2/\pi)\ H$$

$$f = \infty$$

POSITIVE CURVATURE TYPE C (negative surface shear)

Trajectory:

$$z = z_p \left[(\alpha_o/\alpha_p) \sin (\alpha_p\, y/z_p) + 1 - \cos (\alpha_p y/z_p) \right]$$

$$Y = (2\, z_p/\alpha_p) \left[\pi/2 + \cot^{-1} (\alpha_o/\alpha_p) \right]$$

$$H = z_p \left\{ 1 + \left[1 + (\alpha_o/\alpha_p)^2 \right]^{\frac{1}{2}} \right\}$$

$$H_{av} = z_p \left\{ 1 + (\alpha_o/\alpha_p)/ \left[\pi/2 + \cot^{-1} (\alpha_o/\alpha_p) \right] \right\}$$

$$f = (\alpha_p/\alpha_o)^{\frac{1}{2}} \left[1 + (\alpha_o/\alpha_p)^2 \right]^{\frac{1}{2}} \left[\pi/2 + \cot^{-1} (\alpha_o/\alpha_p) \right]^{\frac{1}{2}}$$

When the focusing factor is small at night, either parabolic or logarithmic profile is possible. The best way to distinguish between these two would be to have several receivers located at different distances and aligned with one source, and to measure the focusing factor as a function of distance. Fig. 3-3.1 compares the characteristics of parabolic and logarithmic profiles. Both profiles have a wind of 10 m/s at 400 m. The focusing factor of the logarithmic profile drops very fast within the first kilometer, and then decreases very slowly, having a value near .3 for the next 8 km. The focusing factor of the parabolic profile is almost unity in the first kilometer (behaving like that of the linear profile,) and then decreases fast with distance. Fig. 3-3.2 depicts f-contours in the log z_m vs. log V_m diagram for Y = 9.2 km and C_o = 331 m/s, which helps one determine the appropriate parabolic profile. The penetrating heights and average ray heights as fractions of z_m of the parabolic profile are plotted vs. f in Fig. 3-3.3.

The focusing factor of the linear profile is almost

Fig. 3-3.1 Comparison of parabolic & logarithmic profiles

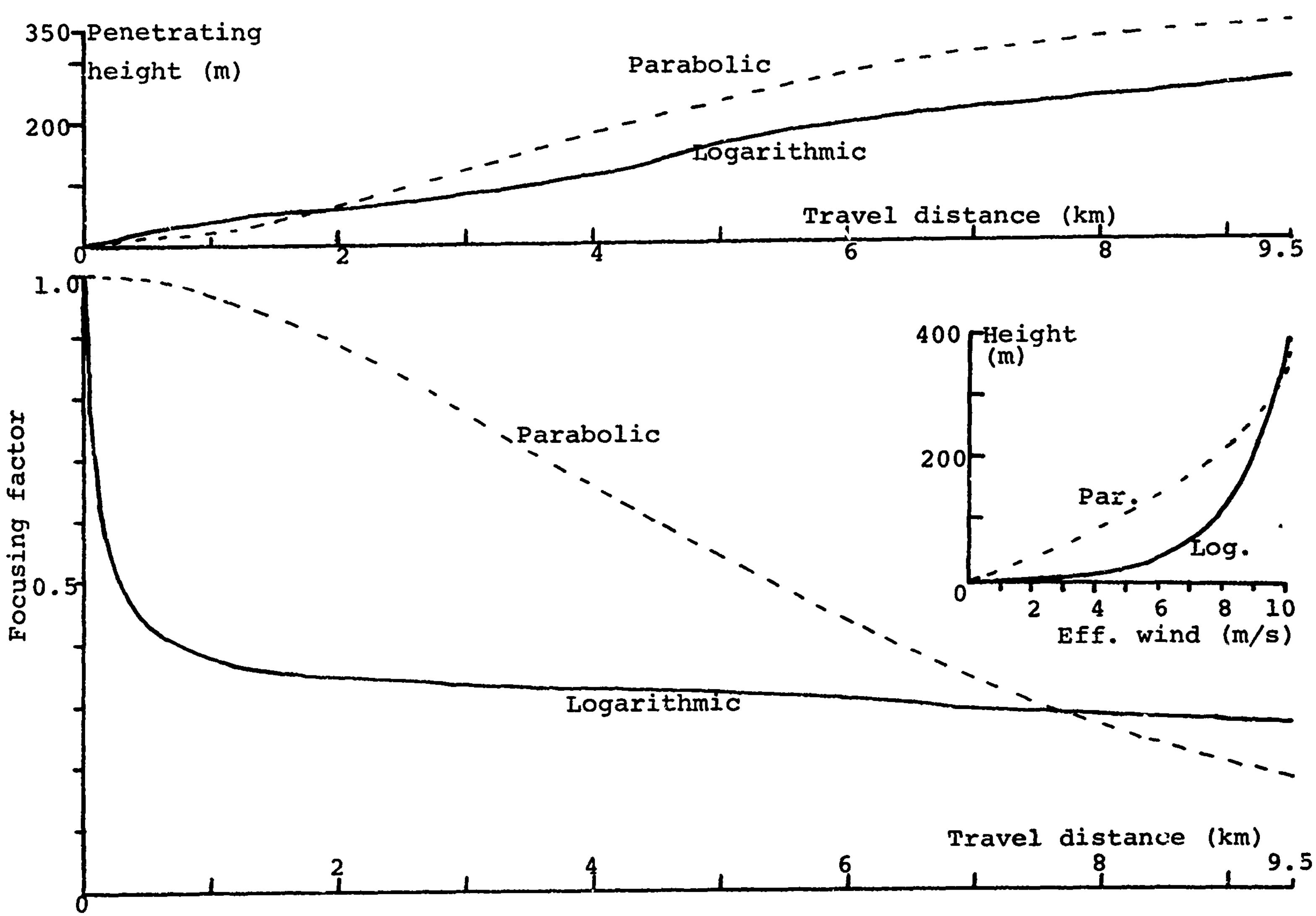

Fig. 3-3.2 f-contours in the log z_m vs. log V_m diagram for the parabolic profile

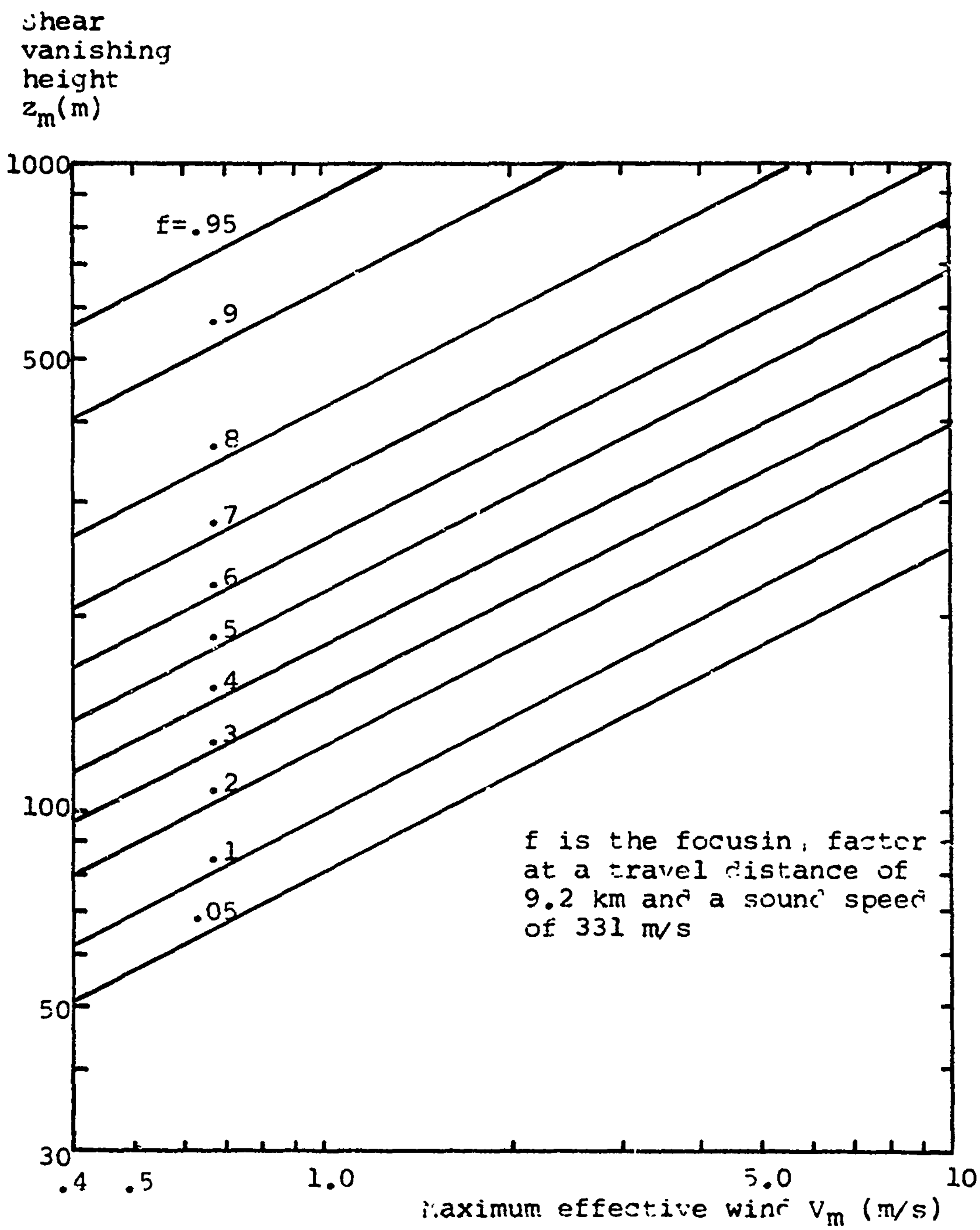

Fig. 3-3.3 H/z_m & H_{av}/z_m vs. f of the parabolic profile

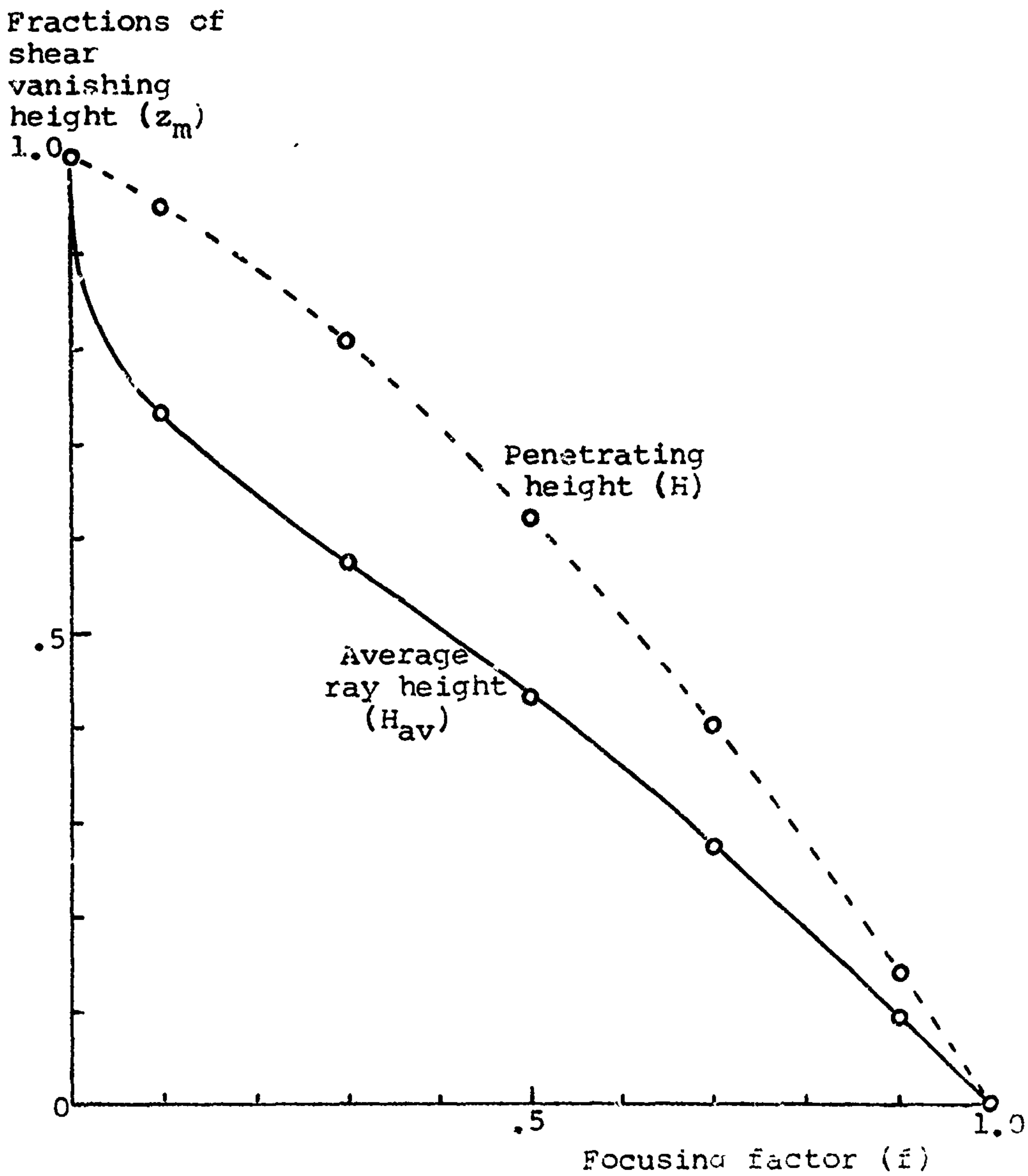

unity, decreasing slowly with the travel distance (Appendix 2). The focusing factor of the positive curvature profile is greater than unity. Travel distances of positive curvature profiles are restricted within the following limits, which are also caustic distances except for the origin:

$$0 < Y < \pi z_p / \alpha_p, \qquad \text{(Type a)}$$

$$Y = \pi z_p / \alpha_p, \qquad \text{(Type b)}$$

$$\pi z_p / \alpha_p < Y < 2\pi z_p / \alpha_p. \qquad \text{(Type c)}$$

In reality, the finite thickness of the atmospheric layer, where the profile is valid, limits the travel distance.

Fig. 3-3.4 shows schematically the signal penetrating heights and focusing factors vs. the travel distance for the elevated shears. An elevated shear predicts a large focusing factor when the penetrating height is near the point of inflection of the profile. Elevated shear type b or c predicts a skip distance Y_{mini} which is also the caustic distance. Y_{mini} can be estimated by assuming the elevated shear to be constant (Appendix 2). Thus one gets for type b,

$$Y_{mini} = 4 \, (C_o \, h_b/S_2)^{\frac{1}{2}}, \qquad (9)$$

where h_b = the thickness of the lower constant velocity layer,

S_2 = the constant elevated shear,

and for type c,

$$Y_{mini} = 2 \, (2 \, C_o \, h_c/S_1)^{\frac{1}{2}} \left[(1 + S_1/S_2)^2 - 1 \right]^{\frac{1}{2}}, \qquad (10)$$

Fig. 3-3.4 Penetrating heights and focusing factors with elevated shears

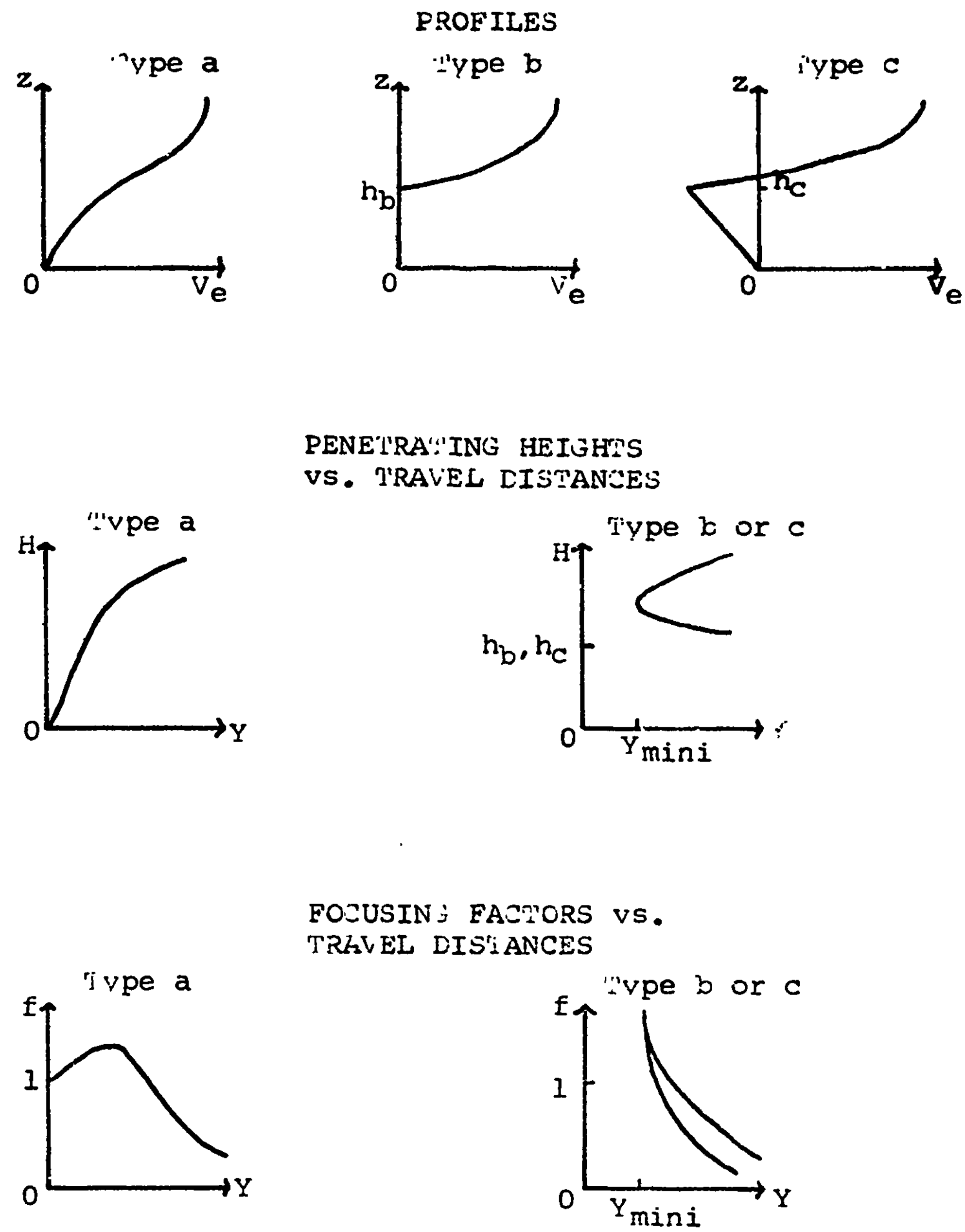

where h_c = the thickness of the lower negative shear layer,

S_1 = the magnitude of the negative shear,

S_2 = the constant elevated shear.

3-4. Amptitude variations and doppler shifts due to parabolic profile fluctuations

A linear theory is developed to calculate the variations of both amplitude and frequency due to fluctuations of the parabolic effective wind profile. With this theory, the effects of individual profile parameters on the signal variation are linearly added. The parameters for parabolic profile are S_o (surface shear) and z_m (shear vanishing height). The results of the calculation (Appendix 3) are the following. The predicted time rate of fractional change of amplitude due to the profile fluctuation is

$$f_a = \left[\frac{d}{dt}(\ln S_o)\right](-1 + Q)\,A, \tag{1}$$

where

$$\frac{d}{dt}(\ln S_o) = \text{the time rate of fractional change of } S_o,$$

$$Q = d(\ln z_m)/d(\ln S_o)$$

= the ratio of fractional variations of z_m and S_o,

and

$$A = (\tfrac{1}{4})\left\{\left[S_o\,Y/(2\,C_o\,\alpha_o)\right]\left[1 + (\alpha_o/\alpha_m)^2\right] - 1\right\}$$

= the ratio of fractional variations of signal amplitude and z_m.

The predicted fractional doppler (shift) due to the profile fluctuation is

$$f_d = \left[\frac{d}{dt}(\ln S_o)\right](D_{So} + Q\,D_{zm}), \tag{2}$$

where

$$D_{So} = [z_m \alpha_o/(2C_o)]\{[S_o Y/(2C_o \alpha_o)][1 + (\alpha_o/\alpha_m)^2] - 1\}$$

= the doppler due to variations of S_o,

$$D_{zm} = [3 z_m \alpha_o/(2C_o)]\{[S_o Y/(2C_o \alpha_o)][1 - (\alpha_o/\alpha_m)^2/3] - 1\}$$

= the doppler due to variations of z_m.

One can infer the profile fluctuation from the observed long-period signal variations. Let the observed time rate of fractional change of amplitude due to the profile fluctuation be F_a, the associated fractional doppler be F_d, and the ratio of F_a/F_d be F. Then, by equating the observed F_a and F_d to the predicted f_a and f_d respectively, one obtains the inferred ratio of fractional variations of z_m and S_o as

$$Q = (FD_{So} + A)/(-FD_{zm} + A), \quad (3)$$

and the inferred time rate of fractional change of S_o as

$$\frac{d}{dt}(\ln S_o) = (F_a/A)/(-1+Q) = F_d/(D_{So} + Q D_{zm}). \quad (4)$$

Finally, one gets the inferred profile fluctuation (peak amplitude) as

$$\Delta V_e = (\tau/4)\left[\frac{d}{dt}(\ln S_o)\right]\{S_o z[1 - (1 - Q)z/(2 z_m)]\}, \quad (5)$$

where τ = the period of variation.

Schematic diagrams in Fig. 3-4.1 illustrate all possible variations of parabolic profiles according to the linear theory. The eminent properties of these variations are listed in Table 3-4.1, where $z_{am} = z_m/(1 - Q)$ denotes the height of

Fig. .-4.1 Fluctuations of parabolic profiles

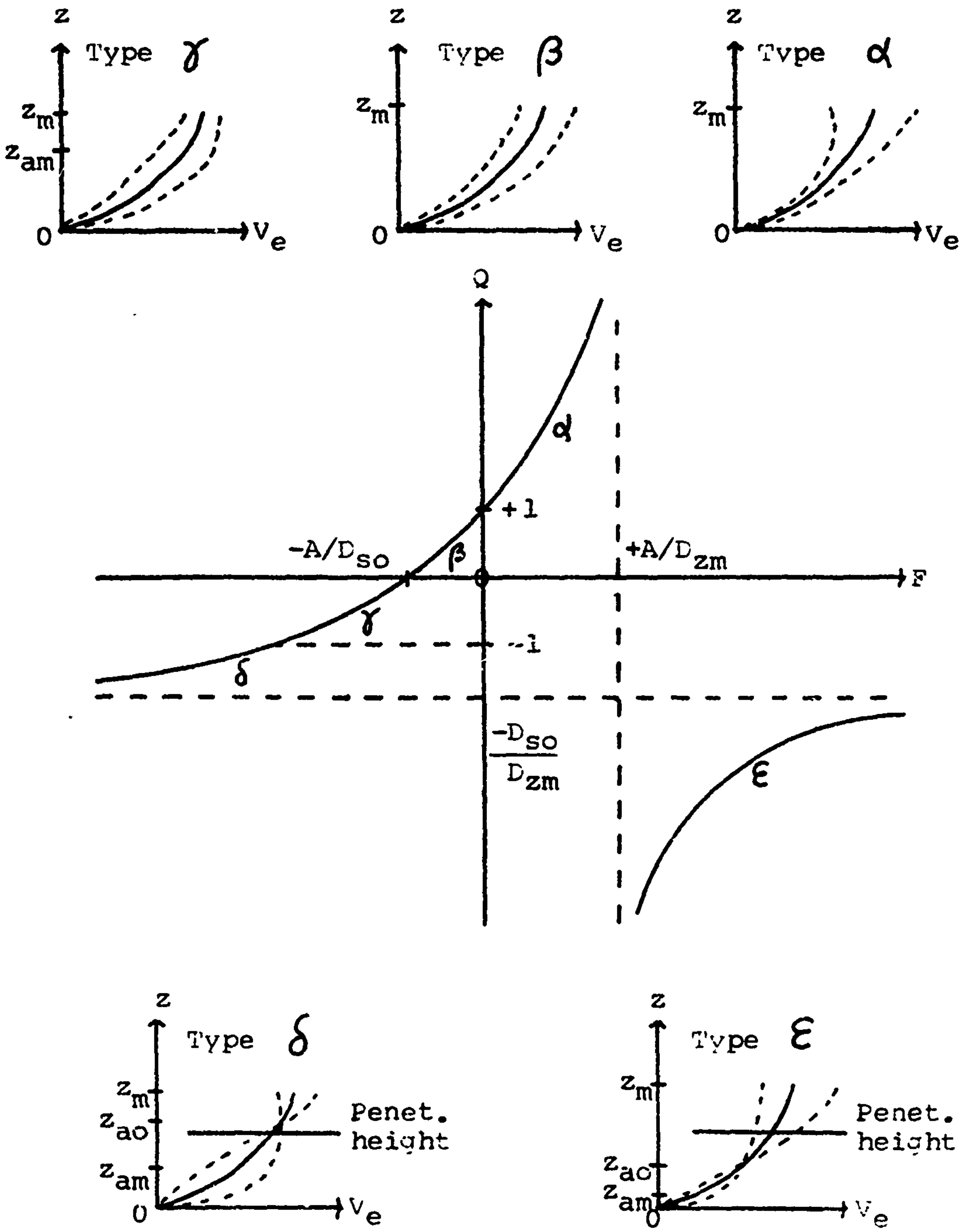

Table 3-4.1 Characteristics of parabolic profile fluctuations

Fluctuation type	α	β	γ	δ	ε
Q	+	+	-	-	-
F	+	-	-	-	+
z_{am}	-	+	+	+	+
z_{ao}	-	+	+	+	+
$(\Delta p)(\Delta V)$	+	-	-	$\pm$	$\pm$

Remarks:

1. The fluctuation type is determined by values of Q and F as shown in Fig. 3-4.1.

2. Q is the ratio of fractional variations of z_m and S_o of the profile, i.e., $d(\ln z_m)/d(\ln S_o)$.

3. F is the observed ratio of the time rate of fractional amplitude change to the fractional doppler shift.

4. $z_{am} = z_m / (1 - Q)$ is the height where the fluctuating wind is relatively maximum.

5. $z_{ao} = 2\, z_{am}$ is the height where the fluctuating wind is zero.

6. $(\Delta p)(\Delta V)$ is the product of the signal amplitude change and the wind change in the boundary layer. When alternative signs are possible, the positive sign is for $z > z_{ao}$ and the negative sign for $z < z_{ao}$.

a relatively maximum fluctuation and $z_{ao} = 2\ z_{am}$ denotes the zero fluctuation height. Also listed in Table 3-4.1 is the sign of the product of the signal amplitude change and the wind change, i.e., $(\Delta p)(\Delta V)$. For fluctuation type α, it is positive, wh h means that an amplitude increase accompanies wind increases at all levels in the boundary layer. For types β and γ, $(\Delta p)(\Delta V)$ is negative. For types δ and ϵ, the sign depends on the height where the wind is recorded. The observed signs of $(\Delta p)(\Delta V)$ and F should help identify the possible types of profile fluctuation which cause the signal variations.

For the theory of profile fluctuations to be applicable, the period of signal variations must be long enough to insure a practical uniformity of associated wind variations over the source-receiver line, since the theory is based on a one-dimensional atmosphere model. If the fluctuating wind system drifts with the average wind, which blows at 5 m/s along the 9 km source-receiver line, for example, then the period of observed profile fluctuations must be at least 30 min. If the profile fluctuation wind is caused by gravity waves, which have a phase velocity component of 50 m/s along the 9 km source-receiver line, for example, then the signal period must be at least 3 min. The periods of all doppler shift data in this experiment are not more than 15 min. One might hope to get profile fluctuations due to gravity waves. Correlations among the probe signal variation, the microbarograph array data, and the wind records were searched for, but no definite correlation was found. A theory seems to be needed to predict characteristics of gravity waves in atmospheric boundary shears, and is not yet available.

In order to get a rough idea of what profile fluctuations might possibly be inferred from the field data, the long-period signal variations on Nov. 21-22, 1970 (Table A-1.6) were analyzed, and the following types of profile fluctuations were obtained:

1) Profile fluctuation type δ ($F = -32\ sec^{-1}$, $Q = -1.4$), for which the maximum wind fluctuation has a peak amplitude of .32 m/s at 123 m.
2) Profile fluctuation type ε ($F = +32\ sec^{-1}$, $Q = -2.9$), which has the maximum wind fluctuation of .12 m/s (peak amplitude) at 76 m.

The average ray height that night was 168 m.

3-5. Short-period fluctuations

When fluctuation periods are from about .5 to 8 min., the turbulence scale is small compared with the signal travel distance, and three-dimensional wind fluctuation models should be considered. Although there has been much work in the literature about wave propagation in a random medium (e.g. Chernov 1960, Tatarski 1961), signal fluctuations in the random medium with average shear structures do not seem to have been studied before. In this section, amplitude variations and phase shifts of the signal propagating in turbulent boundary shears according to ray theory will be presented. To apply the formulas, one should beware of limitations of the theory. Scattered rays due to atmospheric inhomogeneities may interfere with the direct ray when the propagation distance relative to inhomogeneity size scales exceeds a certain limit. After analyzing the field data of probe measurements, one will see that diffraction phenomena are not negligible in this experiment. For transmissions to the 9.2 km site, the wave parameter, which serves as the criterion dividing ray and diffraction regimes (Chernov 1960, p. 74), is found to be of the order of 10. The field data is on the diffraction side, not far from the border of ray and diffraction regimes. However, no full-wave solution, which covers both ray and diffraction, has yet been available for signal propagation in a turbulent boundary layer. Therefore, the field data of short-period fluctuations will be interpreted by the ray theory formulas, and possible corrections for diffraction will be estimated (Section 4-1).

Details of deriving ray theory formulas are described in Appendix 4. The shallow angle approximation is used. The atmosphere is assumed to have a one-dimensional effective shear and three-dimensional wind fluctuations, whose correlation function has a three-dimensional Gaussian form, i.e.

$$\overline{\Delta v_e (x_1, y_1, z_1) \Delta v_e (x_2, y_2, z_2)}$$

$$= \overline{(\Delta v_e)^2} \exp \left\{ - \left[\frac{x_2 - x_1}{a_x} \right]^2 - \left[\frac{y_2 - y_1}{a_y} \right]^2 - \left[\frac{z_2 - z_1}{a_z} \right]^2 \right\}, \quad (1)$$

where a_x, a_y and a_z are the correlation scales along three coordinate axes. The results of the derivation are the following.

The mean square phase shift is

$$\overline{(\Delta \Phi)^2} = (\pi^{1/2} \omega^2 a_y Y/\bar{C}^4) \overline{(\Delta v_e)^2} \quad (2)$$

where ω = the angular frequency of the signal,

a_y = the scale along the source-receiver line,

$\bar{C}$ = the average sound speed,

$\overline{(\Delta v_e)^2}$ = the mean square effective wind fluctuation.

With the shallow angle approximation, phase shifts due to effective wind fluctuations do not depend on average effective wind profiles. The phase shift is directly proportional to the effective wind fluctuation and the square root of a_y, and is independent of a_z and a_x.

The mean square fractional amplitude variation varies with the average effective wind profile. For the linear profile,

$$\overline{(\Delta p)^2} / \bar{p}^2 = \left[\overline{(\Delta v_e)^2}\, a_y/\bar{c}^2 \right] \cdot$$

$$\cdot \left[(\pi^{\frac{1}{2}} Y^3/10)/a_z^4 + (\pi^{\frac{1}{2}} Y^3/15)/(a_z^2\, a_x^2) + (\pi^{\frac{1}{2}} Y^3/10) / a_x^4 \right], \qquad (3)$$

which, for equal a_x, a_y, and a_z, becomes

$$\overline{(\Delta p)^2} / \bar{p}^2 = (4/15)\, \pi^{\frac{1}{2}}\, Y^3 \left[\overline{(\Delta v_e)^2} / a^3\, \bar{c}^2 \right], \qquad (4)$$

where $a = a_x = a_y = a_z$. In comparison with a plane wave source (Chernov 1960), the mean square amplitude fluctuation of a point source in a linear profile is 10 times smaller. The result of Eq. (4) is the same as for a spherical wave in a uniform average medium (Tatarski 1961). For the parabolic profile,

$$\overline{(\Delta p)^2} / \bar{p}^2 = \left[\overline{(\Delta v_e)^2}\, a_y/\bar{c}^2 \right] \cdot$$

$$\cdot \left[K_1/a_z^4 + K_2/(a_z^2\, a_x^2) + K_3/a_x^4 \right]. \qquad (5)$$

The coefficient K_3 ($=\pi^{\frac{1}{2}} Y^3/10$) is the same as for the linear profile. Coefficients K_1 and K_2 are essentially functions of the focusing factor for a given Y (the travel distance). When the focusing factor becomes unity, K_1 and K_2 become the corresponding coefficients of the linear profile, i.e.,

$$K_1 \longrightarrow \pi^{\frac{1}{2}} Y^3/10,$$

and $K_2 \longrightarrow \pi^{1/2} Y^3/15$, as $f \longrightarrow 1$.

Fig. 3-5.1 plots the coefficients K_1, K_2, K_3 as well as the sum of the three, K_S, vs. the focusing factor f.

Now the way of inferring the magnitudes and scales of effective wind fluctuations from the field data is described. The turbulence scale or average eddy size is given by the integral (Taylor 1935)

$$L = \int_0^\infty R(s)\, ds, \tag{6}$$

where L = the integral scale,

$R(s) = \overline{v(r)v(r+s)} \, / \, \overline{v^2}$

= the normalized one-dimensional correlation function of wind fluctuations,

s = the separation coordinate.

For the three-dimensional Gaussian correlation function, the turbulence scales are

$L_x = (\pi^{1/2}/2)\, a_x$ (The horizontal scale perpendicular to the source-receiver line), (7a)

$L_y = (\pi^{1/2}/2)\, a_y$ (the horizontal scale along the source-receiver line), (7b)

$L_z = (\pi^{1/2}/2)\, a_z$ (the vertical scale). (7c)

From the field data, one obtains:

Period of signal variation = τ (sec)

Fractional rms amplitude variation = $\sigma_p/\bar{p}$

rms phase shift = σ_ϕ (rad)

Fig. 3-5.1 Amplitude variation coefficients vs. f for the parabolic profile (Y = 9200 m)

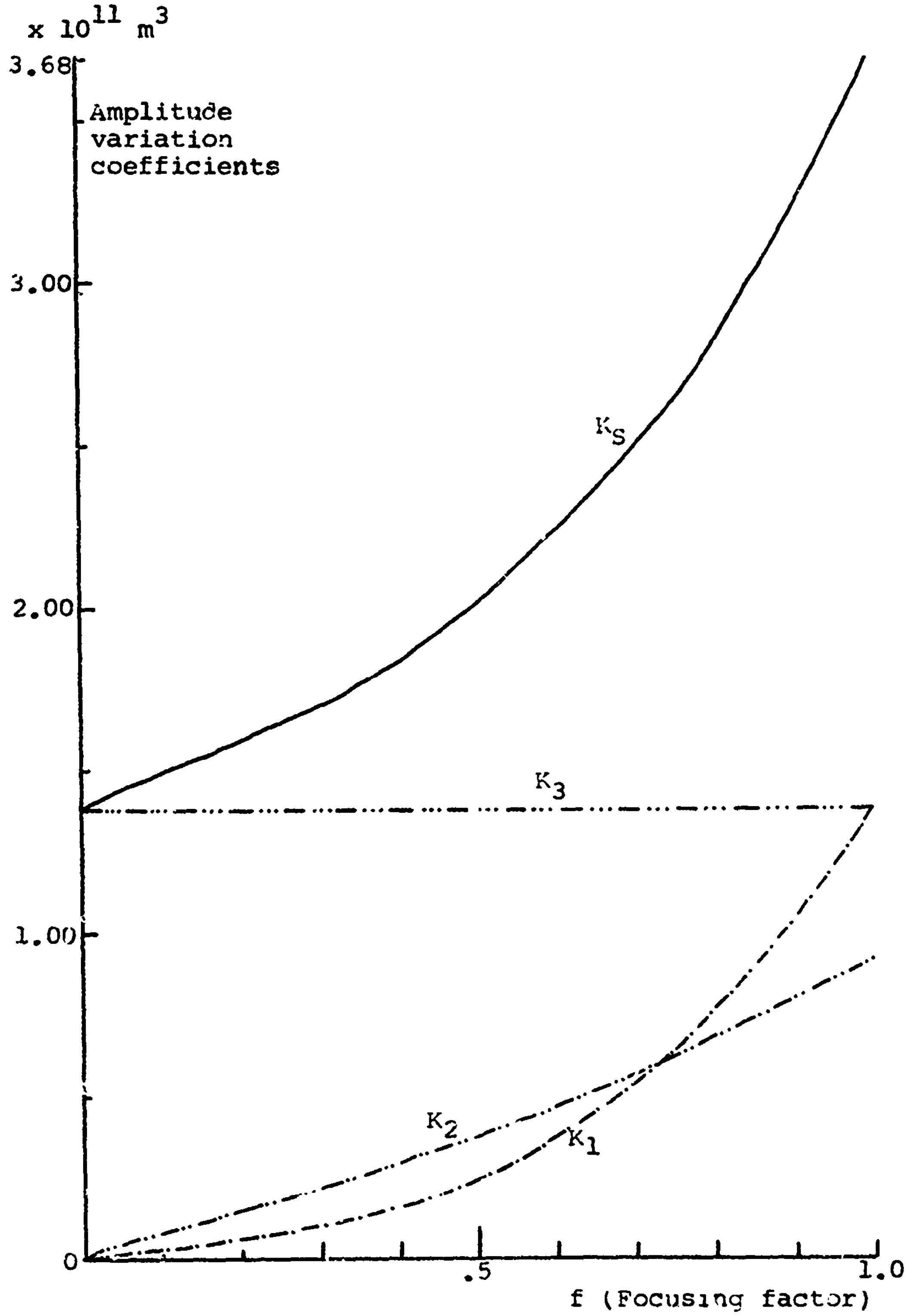

Focusing factor = f

Some data gives the doppler $\Delta\nu$ instead of the phase shift $\Delta\phi$. The conversion formula is

$$\Delta\phi = \tau \, \Delta\nu \, . \tag{8}$$

An appropriate parabolic profile can be chosen from the focusing factor and the synoptic weather information.

To estimate the horizontal turbulence scale, one assumes that the turbulence is horizontally isotropic. In other words, the horizontal turbulence scale along the source-receiver line, i.e., L_y, is assumed to be equal to the horizontal turbulence scale perpendicular to the source-receiver line, i.e., L_x. Since short-period signal variations are mainly caused by the turbulent air motion, drifting with the average wind across the source-receiver line, the horizontal turbulence scale is approximately the product of the period of signal variation and the cross wind component, i.e.,

$$a_y = a_x = (2/\pi^{1/2}) \, \tau \, V_{xav}, \tag{9}$$

where V_{xav} = the magnitude of the horizontal wind component perpendicular to the source-receiver line at the average ray height (H_{av}).

Then the rms wind fluctuations is

$$\sigma_v = \sigma_\phi \bar{c}^2 \, / \, (\pi^{1/4} \, \omega \, a_y^{1/2} \, Y^{1/2}). \tag{10}$$

By taking the ratio of phase and amplitude variations given by the field data, one gets from Eqs. (2) and (5)

$$\sigma_\phi / (\sigma_p/\bar{p}) = (\pi^{1/4}\, \gamma^{1/2}\, \omega / \bar{c})$$

$$/ \left[K_1/a_z^{\,4} + K_2/(a_z^{\,2}\, a_x^{\,2}) + K_3/a_x^{\,4} \right]^{1/2}. \quad (11)$$

From this equation, one can determine a_z and a_x, if the ratio of a_x/a_z (=M) is given, i.e.,

$$a_z = K_{SM}^{\;1/4}\, \bar{c}^{\,1/2}\, \sigma_\phi^{\,1/2} / \left[\pi^{1/8}\, \gamma^{1/4}\, \omega^{1/2}\, (\sigma_p/\bar{p})^{1/2}\right] \quad (12a)$$

$$a_x = M\, a_z, \quad (12b)$$

where $K_{SM} = K_1 + K_2 / M^2 + K_3 / M^4$. (12c)

First of all, isotropic eddies ($a_x = a_y = a_z$) are assumed. One puts $M = 1$, and evaluates a_x ($=a_z$) by Eqs. (12). The a_x thus obtained is supposed to be of the same order as a_y, which is determined by Eq. (9). Otherwise, horizontally isotropic eddies ($a_x = a_y \neq a_z$) are assumed. One should try various values of M until a_x is of the same order as a_y. From the experimental results, the values of a_z are found to be either of the same order of or smaller than the values of a_x, i.e., $M \geq 1$ (Section 4-3). As M inceases, the contributions of K_2 and K_3 to K_{SM} decrease very fast, and that of K_1 remains the same. When $M \gtrsim 3$, K_{SM} almost equals K_1.

CHAPTER 4. EXPERIMENTAL RESULTS

Most of the field data were received at 9.2 km to the SE with the Daniels pipe as the noise reducing device. For longer travel distances, signal has been received at 11 km to the NE and at 20 km to the E on exploratory field trips using wind screens, but the information about signal variabilities is not useful because of poor signal-to-noise ratio. For a travel distance of 4.5 km to the E, there is some good field data obtained with only wind screens.

There is a small hill between the source and the receiver at 9.2 km to the SE as shown in Fig. 4.1. The direct ray must have an initial elevation angle of at least .37 deg in order to be received. Transmission experiments to the 9.2 km receiver were frequently carried out from June 29 through Dec. 30, 1970. The field data collected during this half year has two types of signal variation. The variations with shorter periods of .5 to 8 min have both amplitude and doppler (or phase) information. The variations with longer periods of .5 to 6 hours have only amplitude information.

Section 4-1 gives examples showing how to analyze short-period field data to infer wind fluctuations and turbulence scales, and estimates possible errors induced by the inaccuracy of the ray theory and analyzing methods. In order to investigate diffraction effects, working formulas are derived for predicting amplitude variations and phase shifts of the signal propagating in turbulent boundary shears with wave

Fig. 4.1 Map of the experiment area

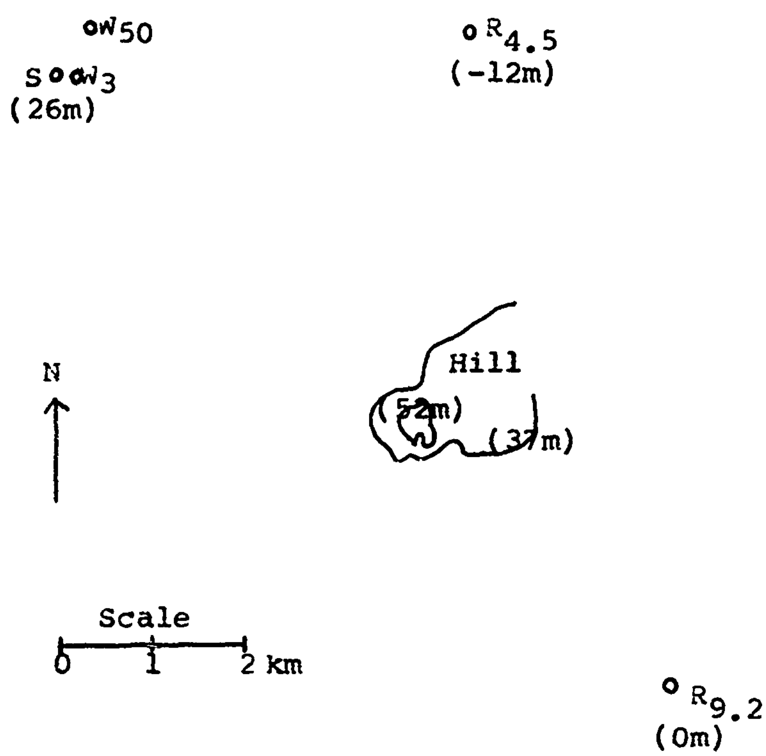

S: signal source

W_3: 3m-level wind sensor

W_{50}: 50m-level wind sensor

$R_{4.5}$: receiver 4.5 km to the E (or 84°)

$R_{9.2}$: receiver 9.2 km to the SE (or 134°)

(*m): * is the elevation above $R_{9.2}$ in meters parameters of the order of 10. Sections 4-2 and 4-3 show the characteristics of wind fluctuations and the shape of eddies in the atmospheric boundary layer. Section 4-4 discusses possible signal variations due to gravity waves. The most notable long-period phenomenon of the atmospheric boundary layer is the diurnal variation. This is presented in Section 4-5, which is also the experimental evidence for fundamental effective wind profiles discussed in the previous chapter.

The wind speeds at 3 m- and 50 m-levels were usually recorded when the probe was operated. The locations of the anemometers are all near the signal source as shown in Fig. 4-1. The wind direction and surface temperature can be estimated from the hourly weather reports of Bedford, Mass., which is about 20 km to the SE. Regular upper air soundings are taken twice a day (0700 and 1900 EST) at Albany, N.Y., Nantucket, Mass. and Portland, Maine, which sometimes indicate the air mass characteristics overhead. These weather stations are about 180 km away from the experiment area. The wind profile in the lowest 1 km layer can sometimes be obtained from pibal soundings at Boston, Mass., which is about 40 km to the SE.

4-1. Short-period amplitude variations and doppler shifts (or phase shifts) of the received signal and their analysis

The phase shifts and their associated amplitude variations of the probing signal with periods of .5 to 8 min. allow one to infer effective wind fluctuations and turbulence scales. The effective wind, as a convenient concept for signal propagation in the atmospheric boundary layer, simplifies the theory. However, with a single receiver as used in this experiment, one can not distinguish between temperature and wind fluctuations. To the first approximation, the experimental results are analyzed by assuming that signal fluctuations are solely due to horizontal wind fluctuations. This assumption is based on the following three reasons. Firstly, the temperature fluctuation is less efficient in affecting sound propagation than the wind fluctuation. One degree centigrade of temperature difference corresponds to only .6 m/s of sound speed difference. Secondly, the temperature inhomogeneity is very efficient in producing the wind. According to the thermal wind formula (Haurwitz 1941, p. 149), for example, one degree centigrade of temperature difference over one km of horizontal distance gives a vertical wind shear of .3 sec^{-1}, i.e., 30 m/s of horizontal wind variation per 100 m of vertical distance. Therefore, temperature fluctuations seem to affect the signal propagation rather indirectly by producing wind fluctuations than directly by presenting sound speed fluctuations. Thirdly, one will see, after analyzing the field data, that there is no significant difference of the wind fluctuation magnitude between the night data and the data collected in early stages of convective periods (Table 4-1.1), although one would expect more temperature fluctuations during convective periods.

Three examples of short-period signal variations, one for each stage of equipment condition, will be presented in this section to show how wind fluctuations and turbulence scales are inferred from the field data. The three stages of equipment are, as mentioned in Section 2-2, characterized by: 1) a 4 cps-bandwidth preamplifier filter and recording doppler (shifts), 2) a 1 cps-bandwidth filter and still recording doppler, and 3) a 1 cps-bandwidth filter and recording phase shifts.

The first example typical for the first stage of equipment is taken from the June 30 data (Fig. 4-1.1). It was a turbulent night as indicated by the 3 m-level wind. The recorder for 50 m-level wind had not been installed at that time. There was a thunder shower later that night at about 0420 EST. The signal variations shown on Fig. 4-1.1 must have been caused by the boundary layer turbulence before a thunder shower. The wind was blowing from 235°, and makes an angle of 79° with the source-receiver line. The signal source was scheduled to be on for 14 min and off for 2 min, with a cycle every 16 min. The broken line on the signal records shows the on or off switching time. One can easily read the

Fig. 4-1.1 An example of field data
on June 30, 1970

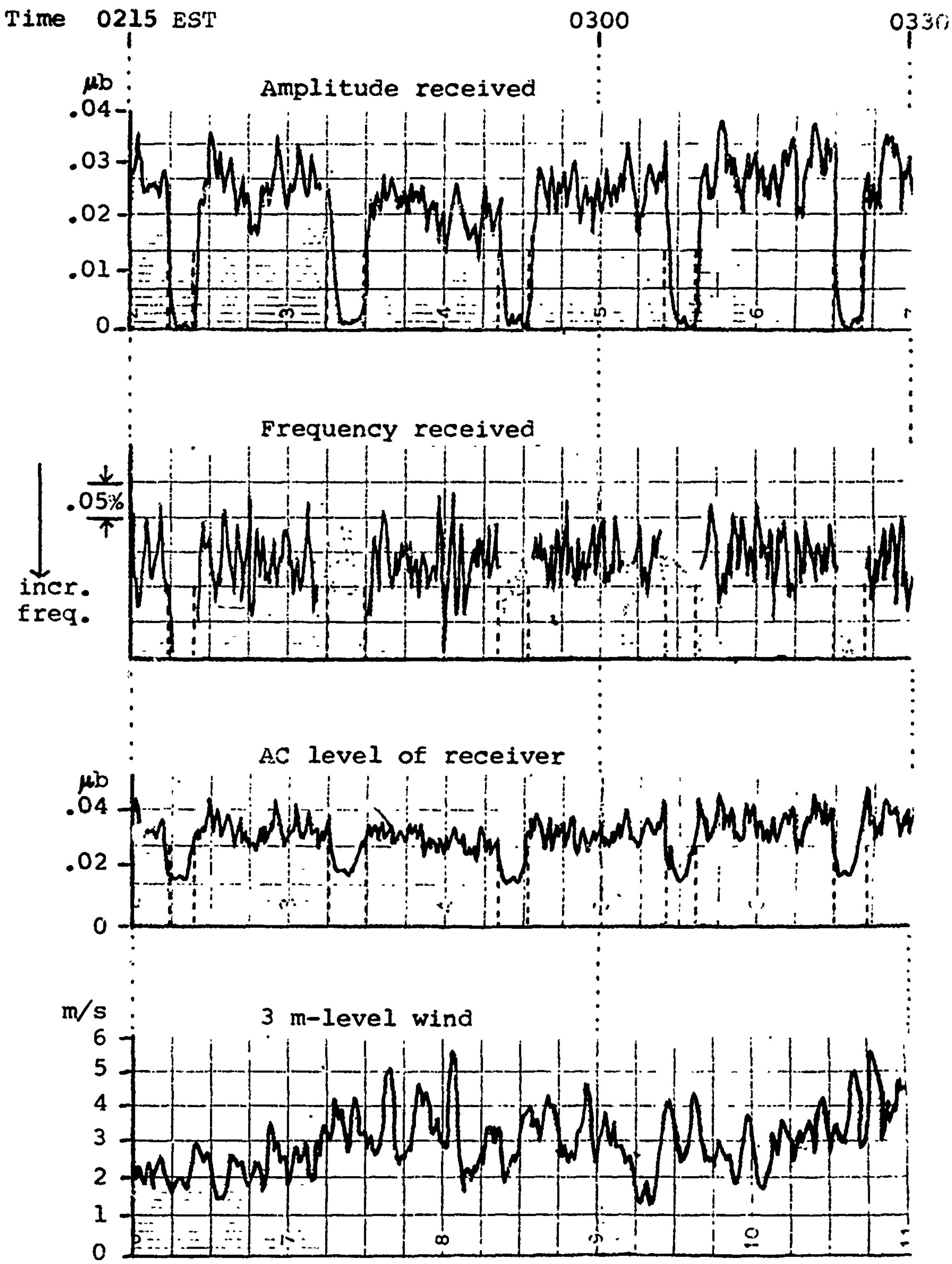

signal-to-noise ratio by comparing AC levels of on- and off-periods. The average signal-to-noise ratio is about 2, which is enough for reliable doppler shifts. The average period, amplitude variation and phase shift are:

$\tau = 52$ sec, (the period of variation)

$\sigma_p/\bar{p} = .147$, (the rms fractional amplitude variation)

$\sigma_\phi = .312$ rad. (the rms phase shift)

The parabolic wind profile appropriate for that night has the parameters:

$z_m = 300$ m, (the shear vanishing height)

$V_m = 2.25$ m/s, (the effective wind component at z_m)

$H = 201$ m, (the signal penetrating height)

$V_{xav} = 9.3$ m/s (the cross wind component at the average ray height)

$K_S = 1.93 \times 10^{11}$ m^3. (the coefficient of amplitude variation)

Therefore the wind fluctuation and turbulence scales are

$\sigma_v = .138$ m/s (the rms wind fluctuation)

$L_x = 941$ m, (the horizontal turbulence scale perpendicular to the source-receiver line)

$L_z = 95$ m. (the vertical turbulence scale)

(Wind is from 235°.)

The second example typical for the second stage of equipment is taken from the Nov. 23 data (Fig. 4-1.2). It is also an example of convective data. Although a passing cold weather front obscured some of the regular convective phenomena, the strong signal amplitude between 0912 and 0934 EST remains to be the familiar feature associated with an elevated shear of

Fig. 4-1.2 An example of field data on Nov. 23, 1970

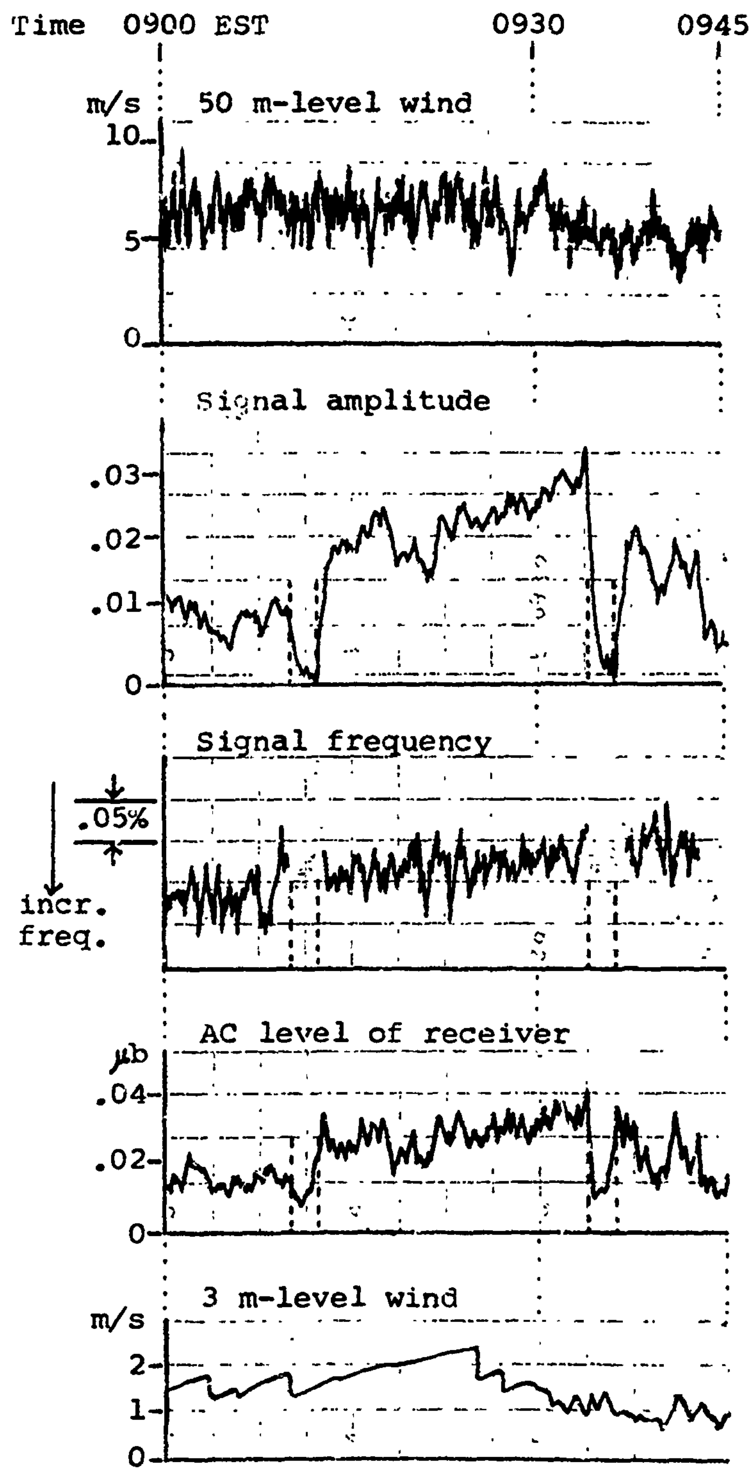

the early convective period (Section 4-5). The doppler shifts are reliable, because the variations of amplitude, frequency and AC level are all well correlated and the average signal-to-noise ratio is about 3, which is greater than the minimum requirement of 1. The average period, amplitude variation and phase shift are:

τ = 43 sec,

$\sigma_p/\bar{p}$ = .050,

σ_ϕ = .115 rad.

The appropriate parabolic profile has the parameters:

z_m = 360 m,

V_m = 4.50 m/s,

H = 275 m,

V_{xav} = 3.55 m/s,

$K_S = 1.77 \times 10^{11}$ m^3.

Therefore the wind fluctuation and turbulence scales are:

σ_v = .096 m/s,

L_x = 198 m,

L_z = 154 m.

(Wind is from 250°.)

The third example typical for the third stage of equipment is taken from the Dec. 14 data (Fig. 4-1.3). Doppler shifts were integrated and recorded directly as phase shifts. The phase shifts are reliable, because signal-to-noise ratios are greater than 1. This example shows large signal variations but very little low-level wind fluctuations of comparable

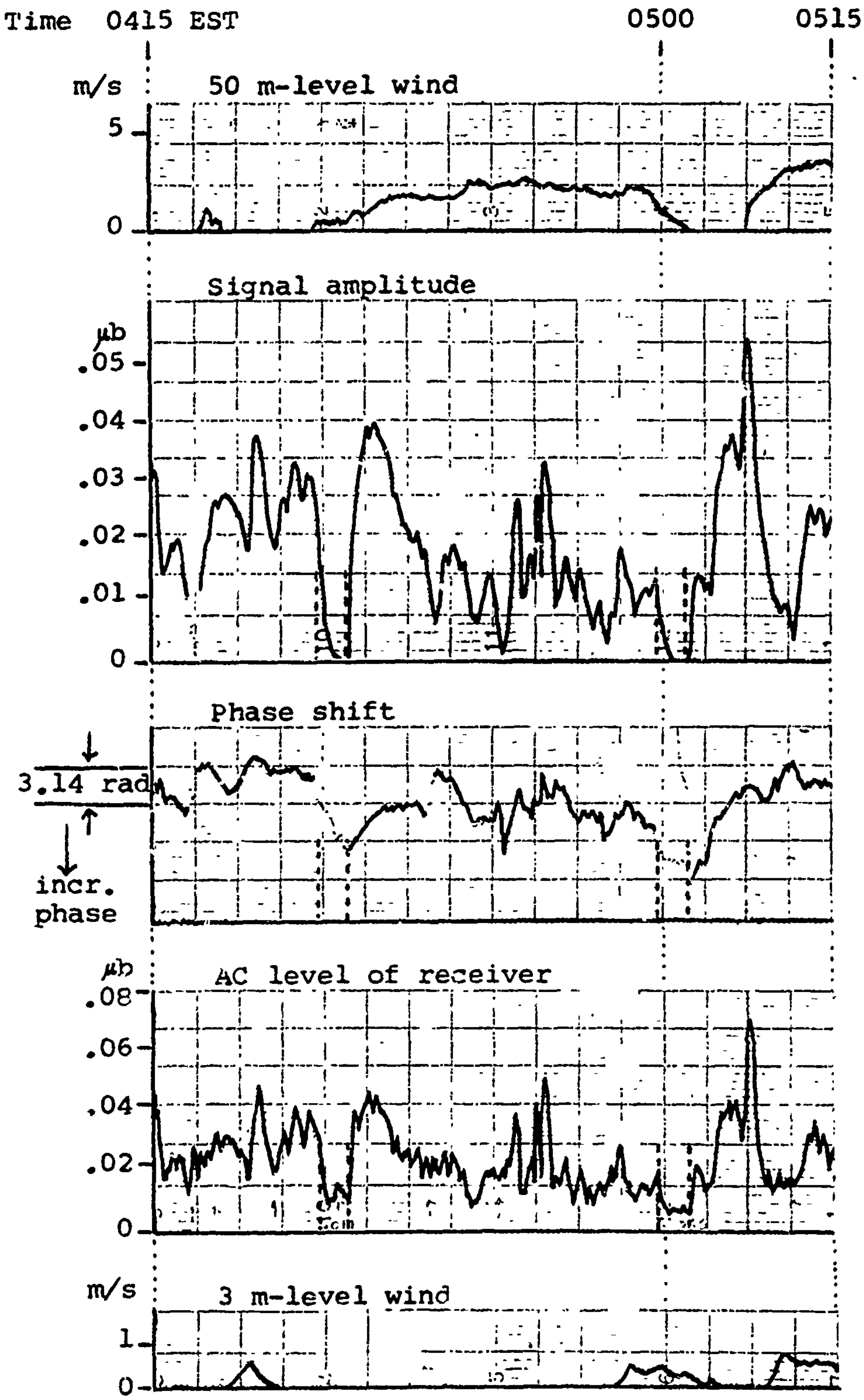

Fig. 4-1.3 An example of field data on Dec. 14, 1970

periods. The signal variations seem to be associated with an elevated shear in the winter. No significant temperature inversion in the lowest 1 km-layer is indicated by the 0700 EST upper air soundings. The average period, amplitude variation and phase shift are:

$$\tau = 72 \text{ sec},$$

$$\sigma_p/\bar{p} = .223,$$

$$\sigma_\phi = .540 \text{ rad}.$$

The suitable parabolic profile has the parameters:

$$z_m = 375 \text{ m},$$

$$V_m = 5.75 \text{ m/s},$$

$$H = 300 \text{ m},$$

$$V_{xav} = 2.0 \text{ m/s},$$

$$K_S = 1.77 \times 10^{11} \text{ m}^3.$$

Therefore the wind fluctuation and turbulence scales are:

$$\sigma_v = .463 \text{ m/s}$$

$$L_x = 140 \text{ m},$$

$$L_z = 156 \text{ m}.$$

(Wind is from 300°.)

Finally the average periods, wind fluctuations, and turbulence scales derived from all available field data are summarized in Table 4-1.1. The details are listed in Appendix 1.

The average vertical turbulence scale is 99 m (Table 4-1.1). A test of the relative importance of diffraction phenomena is the wave parameter, which is defined as the ratio

Table 4-1.1 Summary of periods, magnitudes, and scales of horizontal wind fluctuations

Date (1970)	Time of the day	Period τ (sec)	Magnitude σ_v (m/s)	Scale L_x (m)	L_z (m)
5/8	Night	188			
6/30	Night	61	.135	982	89
8/15	Night	111	.143	830	53
8/16-17	Night	35	.047	402	64
	Conv.	29	.107	236	78
11/21-22	Night	49	.128	219	122
	Conv.	49	.057	208	106
	Night	455	.229	1364	97
11/23	Conv.	43	.090	204	153
12/14	Night	99			
	Conv.	112			
12/19	Night	104	.181	581	126
	Conv.	105	.191	540	104
Average	Night	138	.144	730	92
	Conv.	68	.111	297	110
	Total	111	.131 ±.055	557	99.2 ±28

Remarks:

a) The travel distance is 4500 m for May 8, 1970 data, and is 9200 m for the remaining data.

b) "Conv." for the time of the day refers to early stages of the daily convective period (approximately from 1 hr after sunrise until 2-4 hrs before noon).

c) Because of special circumstances, the data of May 8 and December 14, 1970 does not give meaningful results about wind fluctuations and turbulence scales (Tables A-1.1 and A-1.8).

of the cross-sectional area of the first Fresnel zone to the area scale of inhomogeneities, i.e.,

$$D = 2 \lambda Y / (\pi a_z^2)$$
$$= \lambda Y / (2 L_z^2).$$

The wave parameter for transmissions to the 9.2 km is found to be 12. Therefore, the diffraction phenomena are not negligible. One should investigate how much the scattered rays have interfered with the direct ray.

To estimate the effect of diffraction phenomena on signal fluctuations in the boundary turbulence, one can modify the formulas of intermediate values of the wave parameter which have been derived for a plane wave (Obuchow 1953, p. 167; Chernov 1960, p. 83) as

$$\overline{(\Delta \phi)^2} = E \left[1 + (\tan^{-1} D) / D \right] \qquad (1a)$$

$$\overline{(\Delta p)^2} / \bar{p}^2 = E \left[1 - (\tan^{-1} D) / D \right] \qquad (1b)$$

where

$$E = \overline{(\Delta v_e)^2}\, \pi^{\frac{1}{2}}\, a_y\, \omega^2\, Y / (2\, \bar{c}^4),$$

and the correlation scales perpendicular to the source-receiver line, a_z and a_x, are here assumed to be equal. In the limit of ray approximation, i.e., for small wave parameters, Eqs. (1) and (2) approach Eqs. (2) and (3) in Section 3-5 respectively except for a factor in the formulas of amplitude variations, which varies with the average effective shear. Thus, in the ray theory, one has

$$\overline{(\Delta\phi)^2} = 2E \tag{2a}$$

$$\overline{(\Delta p)^2} / \bar{p}^2 = E\,(KD)^2 / 3, \tag{2b}$$

where D is the wave parameter defined above, and K the factor determined by average shear structures. For the plane wave,

$$K = 1.$$

For the point source in a linear effective wind profile,

$$K = 1 / (10)^{1/2}.$$

For the point source in a parabolic effective wind profile,

$$K = \left[3K_S / (8\,\pi^{1/2}\,Y^3) \right]^{1/2},$$

where the coefficient K_S for Y = 9200 m can be read from Fig. 3-5.1. From Eqs (1) and (2), one can have generalized formulas of intermediate values of the wave parameter for signal propagation in the turbulent boundary layer as

$$\overline{(\Delta\phi)^2} = E\,\left[1 + (\tan^{-1} D) / D \right] \tag{3a}$$

$$\overline{(\Delta\ p)^2} / \bar{p}^2 = E \left\{ 1 - \left[\tan^{-1} (KD) \right] / (KD) \right\}. \tag{3b}$$

These formulas should allow one to infer more nearly correct values of wind fluctuations and turbulence scales. From Eq. (3a), it was found that the wind fluctuation has been underestimated by using the ray theory. The correction factor is

$$C_{\Delta v} = \left\{ 2 / \left[1 + (\tan^{-1} D/D) \right] \right\}^{1/2}$$
$$= 1.33\ .$$

Therefore the wind fluctuation is possibly underestimated with the ray theory by almost **33%.** A more nearly accurate evaluation of turbulence scales calls for solving the equation, from Eqs. (3),

$$(R_S - 1)\, D = (R_S/K)\, \tan^{-1}(KD) + \tan^{-1} D,$$

where

$$R_S = \sigma_\Phi^{\,2} / (\sigma_p^{\,2}/\bar{p}^2) \qquad \text{(given by field data)},$$

and K is given by the average boundary shear model. The accuracy of inferring turbulence scales by the ray theory depends on R_S, which ranges from 1.1 to 15.2, averaging at 5.3 (Tables A-1.1 to A-1.9). The correction factor for diffraction is found to be

$$C_{Lz} = .34, \text{ for } R_S = 1.1,$$

$$C_{Lz} = .98, \text{ for } R_S = 5.3,$$

and $$C_{Lz} = 1.06, \text{ for } R_S = 15.2.$$

Therefore the error of inferring turbulence scales by the ray theory is generally within 5% except for values of R_S very close to unity, when the vertical turbulence scale may be overestimated by 70%.

The results of data analysis can have errors due to the inaccuracy of V_{xav} (average horizontal wind component perpendicular to the source-receiver line), the error of which is estimated to be within about 30%. Therefore, the errors of inferred wind fluctuations and horizontal turbulence scales are estimated to be within 15% and 30% respectively. The error of inferred vertical turbulence scales caused by the inaccuracy of f (the focusing factor) is estimated to be within about 20%.

4-2. The inferred horizontal wind fluctuations

The wind fluctuations inferred from the probe data approximately represent the horizontal wind fluctuations at the average ray heights, which, in this experiment, range from 141 m to 258 m, averaging at 192 m (Table A-1.10). All the field data were collected with strong boundary shears. Unless the shear is elevated, the fluctuation of the 50 m-level wind is usually a good indicator of the boundary turbulence. The Nov. 21-22, 1970 data is a typical example (Fig. 4-2.1). The night started with a very turbulent boundary layer as indicated by the wind record. It became generally quieter later on, except a few brief periods with strong turbulence (e.g., 0420-0510 EST). The average ray height that night was estimated to be 168 m. The inferred rms wind fluctuations (σ_v) vs. the rms wind fluctuations monitored at 50 m (σ_{v50}) are listed in Tables A-1.11 and A-1.12 (Appendix 1) and plotted in Fig. 4-2.2. The data spreads over a wide range. σ_{v50} is about 1 to 14 times σ_v. If a linear proportionality exists between σ_{v50} and σ_v, the 50 m-level wind fluctuation is roughly 3 times the inferred wind fluctuation as indicated by the eye-drawn average slope in Fig. 4-2.2. Despite the wide spread of slopes, the inferred wind fluctuation at 168 m is clearly smaller than the wind monitored at 50 m.

The fact that the wind fluctuations at upper levels are smaller than those at lower levels in the boundary layer has been demonstrated by direct measurements with aircraft (Bunker

Fig.4-2.1 The 50m-level wind and probe signal records on Nov.21-22, 1970

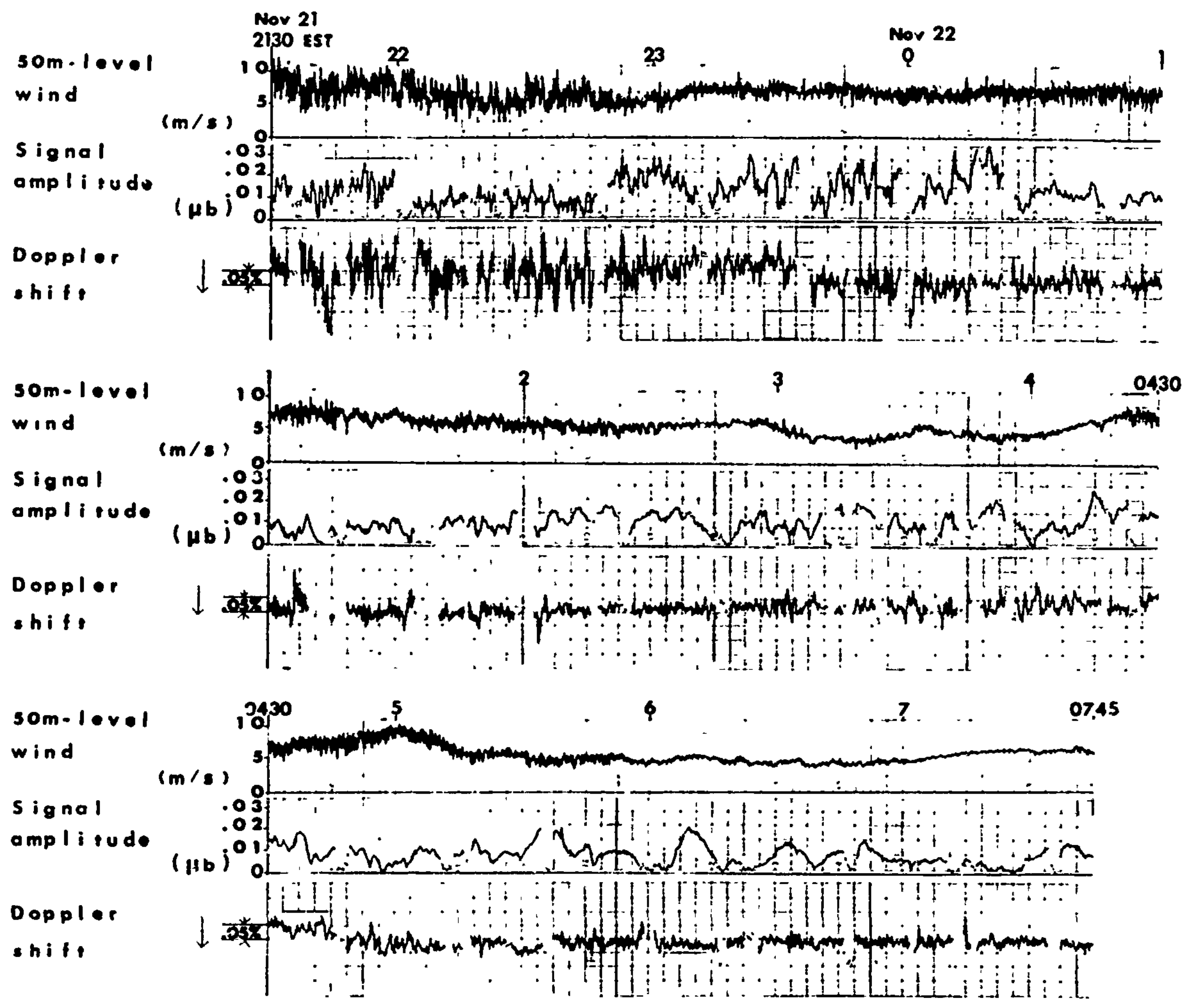

Fig. 4-2.2 rms fluctuations of inferred wind vs. 50 m-level wind on Nov. 21-22, 1970

O: short-period data (Table A-1.11)
Δ: long-period data (Table A-1.12)

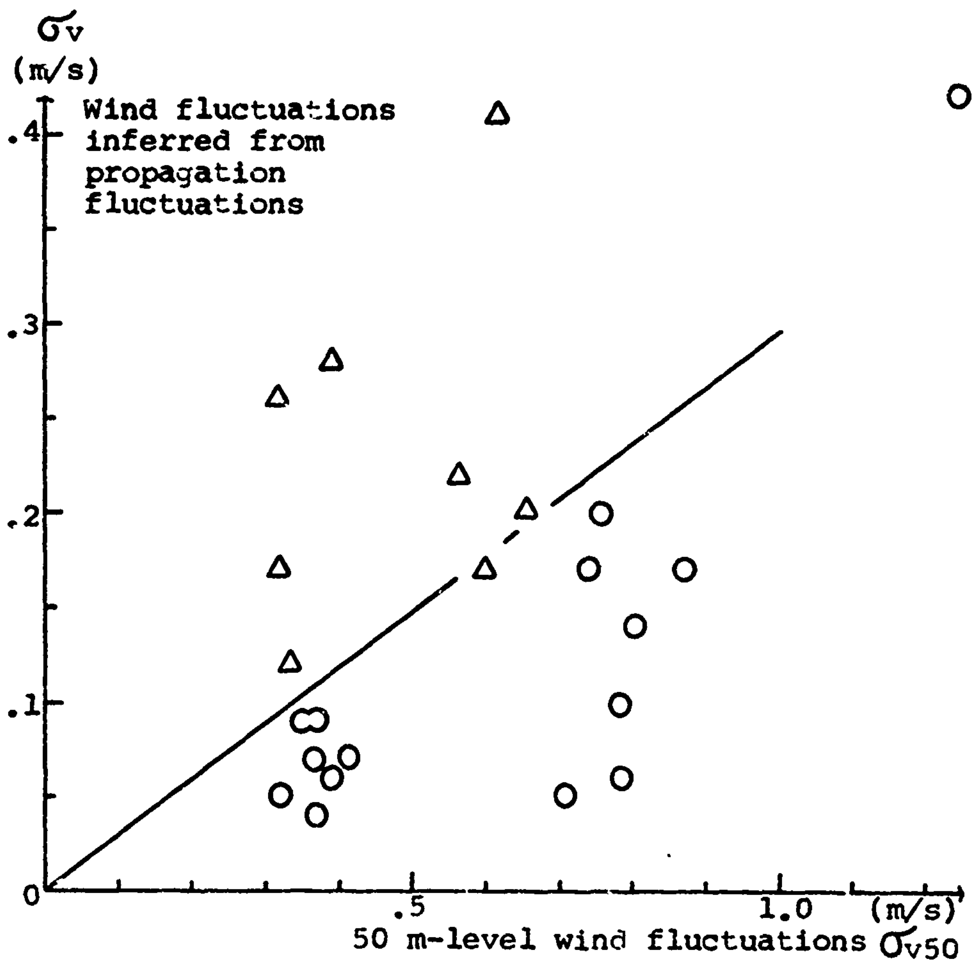

1955, Lettau and Davidson 1957), and with anemometers mounted on high towers (Bysova et al 1965). The aircraft measurements were mostly conducted during periods of strong convection. The horizontal wind fluctuations detected with aircraft over the North Atlantic Ocean and over the O'Neill, Neb. plains all roughly show that the fluctuation at 168 m is smaller than that at 50 m by a factor of about 2. The Obninsk 300-m tower data includes a stable case which also indicates that the 50 m-fluctuation is greater than the 168 m-fluctuation by a factor of about 2. In comparison with the aircraft and tower measurements, the inferred wind fluctuations at 168 m on Nov. 21-22, 1970 seem to be slightly smaller but of the same order.

The rms wind fluctuation averaged over all the available data (Table 4-1.1) is .13 ± .06 m/s. This represents the horizontal wind fluctuation at about 192 m, which is the average H_{av} as listed in Table A-1.10. In comparison with the Obnink tower data, the wind fluctuation inferred from propagation fluctuations is also slightly smaller but of the same order. The Obninsk data (Byzova et al 1965, p. 79) gives the ratio of $\sigma_v/\bar{V}_{300}$ at 192 m as about .03 ± .006. The average wind at 300 m ($\bar{V}_{300}$) for this experiment is estimated to be about 10 m/s. Therefore the rms wind fluctation at 192 m should be .30 ± .06 m/s. Even if one corrects for the possible underestimation by the ray theory (Section 4-1), the inferred wind fluctuation is still smaller than the wind fluctuation measured with meteorological towers. The reason for a smaller wind fluctuation inferred from propagation fluctuations seems to be that the probing signal mainly propagates near the shear vanishing height. The wind near shear vanishing heights is expected to fluctuate less than at lower levels.

4-3. The inferred eddy sizes

The inferred turbulence has horizontal scales of 204 m to 1364 m, which are dictated by characteristics of the recording system. The inferred vertical turbulence scales range from 53 m to 153 m with an average of 99 ± 28 m. Therefore, the eddies seem to be mostly elongated in the horizontal direction. The ratios of horizontal to vertical scales (L_x/L_z) are plotted vs. horizontal scales (L_x) in Fig. 4-3.1. The isotropic eddies have scales of about 100 m. As the horizontal scale becomes greater, the eddy becomes more and more elongated horizontally.

In the literature, the only report about turbulence scales, which can be compared with the results of this experiment, was given by Lumley and Panofsky (1964, p. 196). They analyzed the data, which Singer obtained at Brookhaven, and concluded that, in the stable air, large eddies are about 4 times as long (2000 m) as they are high (500 m), and small eddies are more nearly isotropic. They did not mention how small their isotropic eddies are. However, their results agree with those of this experiment on the general trend that small eddies are more nearly isotropic. The eddies in the boundary shear layer as inferred by the probe become anisotropic at smaller scales than what Singer observed at Brookhaven. With the same ratio (L_x/L_z) of 4, for example, the eddies of this experiment have horizontal scales of about 420 m instead of 2000 m as reported by Lumley and Panofsky.

Fig. 4-3.1 L_x/L_z vs. L_x

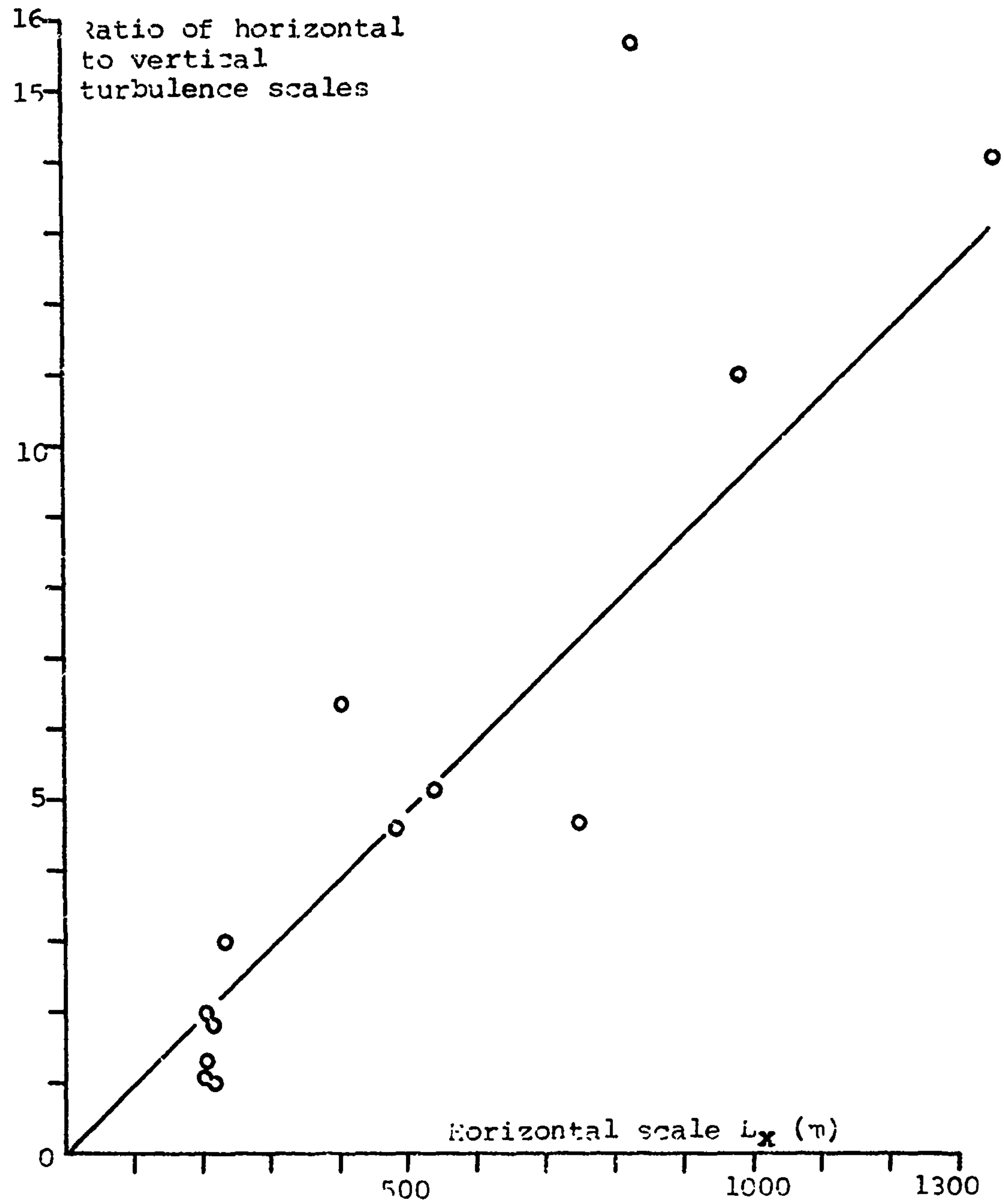

In other words, the eddies in the boundary shear layer seem to be more elongated horizontally. The shape of the eddies inferred by the probe measurements seems to have been modified by the boundary shear in such a way that they are more elongated horizontally than those observed by direct measurements. Panofsky & Singer (1965) and Mielke & Panofsky (1970), using data from various locations, calculated the phase lag between wind fluctuations at different heights. The upper portions of the eddies were found to be downwind of the lower portions, and had slopes which are of order unity, becoming more nearly vertical with height. The phase lag of wind fluctuations could contribute to the flattening of eddies. The decrease of phase lag with height seems to imply that the wind shear decreases with height in the boundary layer.

It is also interesting to investigate the relations among the vertical turbulence scale, the average ray height, and the boundary shear thickness (z_m). Fig 4-3.2 plots the average ray height (H_{av}) vs. the vertical scale (L_z). The ratio of L_z/H_{av} is found to be .57 $\pm$ .22. Similarly one gets the ratio of L_z/z_m to be .29 $\pm$ .13. In other words, the vertical scale of the eddies is roughly 57% of the average ray height and 29% of the boundary shear thickness.

Fig. 4-3.2 H_{av} vs. L_z

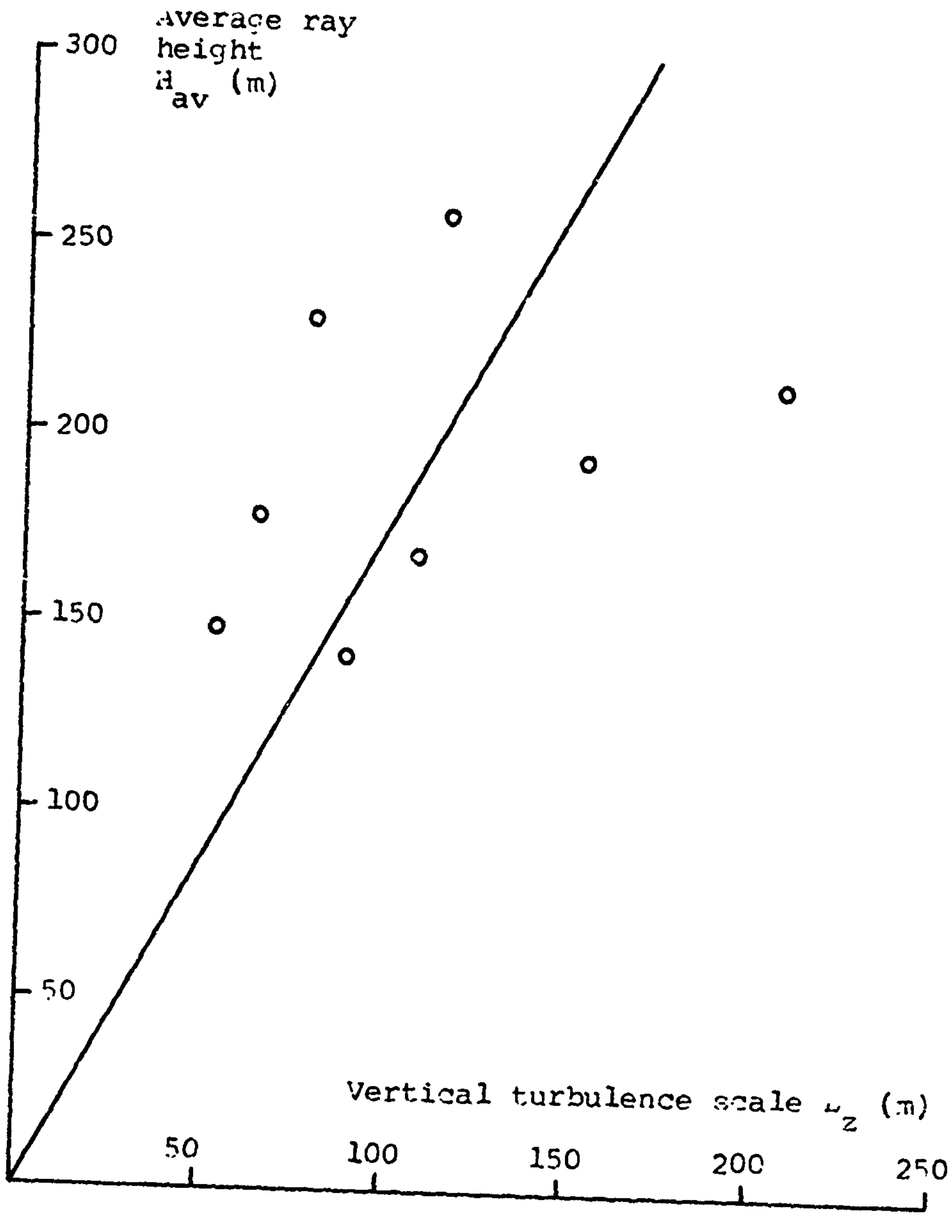

4-4. About detecting gravity waves

During the probe measurements over the 9.2 km travel distance from June 29 through Dec. 30, 1970, a microbarograph array was continuously monitoring the gravity wave pressure in the experiment area. The microbarograph records were compared with the probe signal records. No significant correlation among them was found. According to a simple gravity wave theory (Madden and Claerbout 1968), a few gravity waves recorded by the microbarographs should have caused detectable doppler shifts of the received signal, but no corresponding signal frequency variations were obtained. The actual reason for this is still not clear. The doppler shifts due to gravity waves could have been obscured by stronger doppler shifts with shorter periods due to the boundary layer turbulence. Later in the experiment, more electronic filtering was introduced to the receiving system in order to show long-period signal variations more clearly. Also the doppler shifts were integrated through a high-pass filter to give signal phase shifts. But, unfortunately, the signal transmitter was still under the constant-frequency control mode. The phase of the signal source was not steady enough over long periods. This might be another reason for not having detected gravity wave winds. Besides these, from the 50 m-level wind records, which did not clearly show the perturbing winds of gravity waves, it seems that a detailed theory of gravity waves propagating in the turbulent boundary layer is needed in order to predict correct signal doppler shifts.

The signal transmitter has now been put under the constant-phase control mode. This mode should give a probing signal with steadier phase over long periods. Three more signal receivers are being assembled. The probe will soon have an array of receivers. These improvements of the equipment should greatly increase the chance of detecting gravity waves.

4-5. Diurnal variations of the atmospheric boundary layer

The prolonged operation of the probe with the receiver located at the 9.2 km site has shown diurnal variations of the atmospheric boundary layer. Various effective wind profiles are indicated by the diurnal variation of average signal amplitudes. Usually no signal is received from noon to sunset. The receiver starts getting the signal around sunset, and usually continues to have signal until 2-4 hours before noon of the next day. The strongest signals of the day often appear both at the beginning and at the end of the receiving period. Fig. 4-5.1 is a typical example which shows diurnal variations of the signal amplitude, the wind speeds at 3 m- and 50 m-levels, and the surface temperature. The example includes two signal receiving periods on Aug. 15-17, 1970. Four effective wind profiles at 0700 and 1900 EST each day were obtained by taking averages of the regular upper air soundings at Albany, N. Y., Nantucket Mass., and Portland, Maine. They indicate that the night of Aug. 16-17 certainly had a stronger effective boundary shear than the night before, and that the shear vanishing height varies from 200 m to 500 m on those days. Also shown in Fig. 4-5.1, are two effective wind profiles from Boston pibal soundings taken at 1 am EST each day. The following is a qualitative discussion about the typical effective wind profiles for different times of the day.

In the period from noon to sunset, when no signal is

Fig. 4-5.1 An example of diurnal variations of the atmospheric boundary layer on Aug. 15-17, 1970

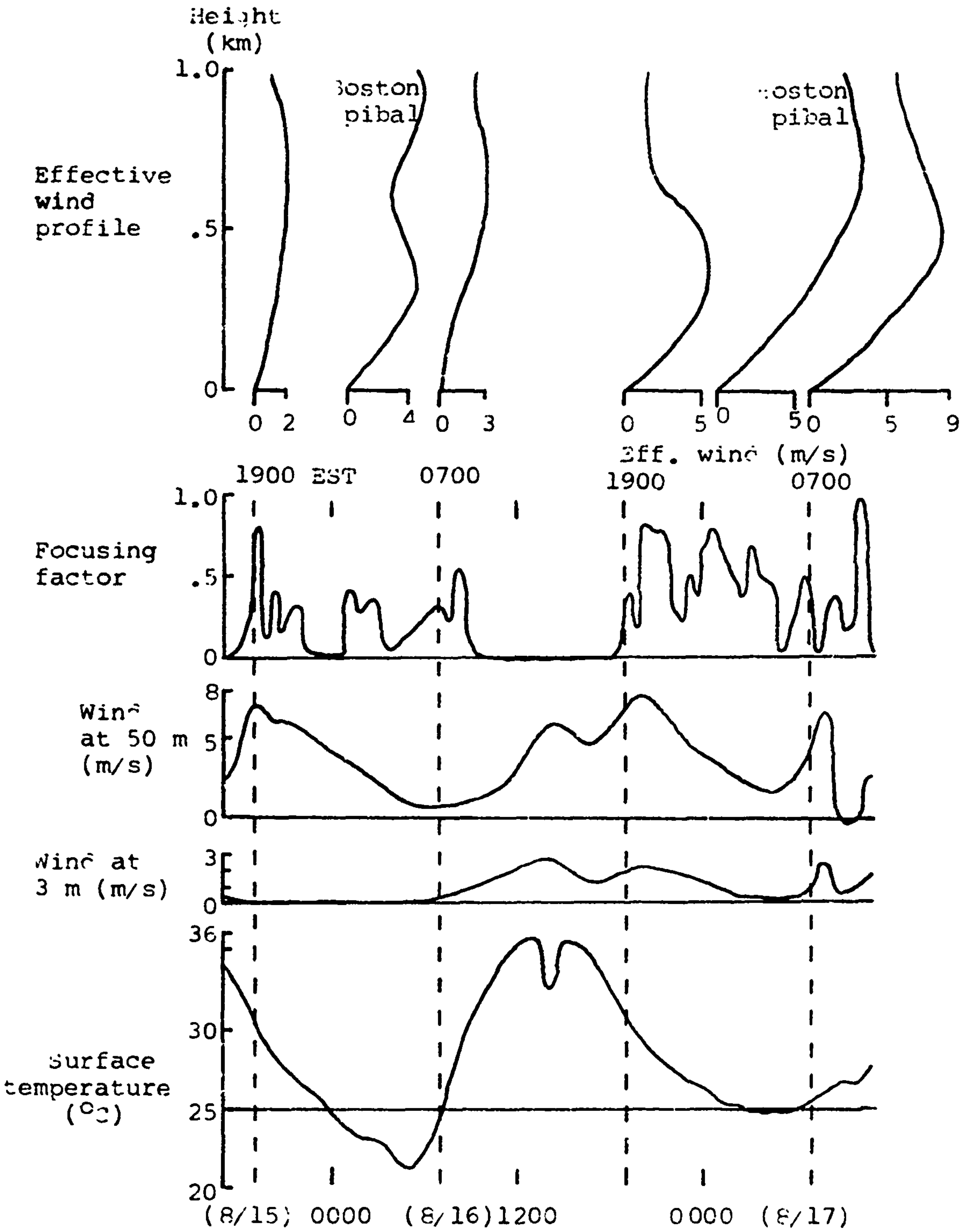

received, the effective shear is negative because of the strong temperature lapse rate.

At night, the effective wind profile is possibly parabolic or logarithmic when the focusing factor is small, presumably less than .5, and the signal penetrates up to where the shear almost vanishes or becomes very small. When the focusing factor is large, presumably greater than .5, the signal penetrates only the lower part of the boundary shear, and the effective wind profile is possibly linear or even has a positive curvature.

The effective wind profile, which is responsible for the strong signals at both ends of receiving period, is possibly an elevated shear. As shown in Fig. 4-5.1, the strong signal in the early evening accompanies the maximum rate of decrease of the surface temperature. On the other hand, the strong signal before noon accompanies the maximum rate of increase of the surface temperature. In the early evening, the wind records show large shears in the lowest 50 m-layer. But because of the residual temperature lapse rate from the daytime surface heating, the effective shear at low levels is reduced, so that a positive curvature may exist. Before noon, a large temperature lapse rate at low levels is formed due to the ground heating, and the wind records often indicate almost no shear in the lowest 50 m-layer. As a result, the effective profile before noon is likely elevated shear type b or c, which has a zero or negative surface shear (Fig. 3-3.4).

Diurnal variations of the signal amplitude are less obvious in winter than summer. Also weather disturbances can obscure diurnal variations. A summary of the 9.2 km signal transmissions is shown in Fig. 4-5.2, where the focusing factors have not been corrected for the relaxation damping, and are smaller than the actual focusing factors by about 7% in summer and 30% in winter (Section 3-1). All the actual focusing factors are smaller than unity except that in the early evening of June 12, 1970. Sunset, sunrise and noon appear to be the natural dividing times between periods of different transmission levels. The annual probability of signal transmission to the 9.2 km site is about 83% at night, 64% before noon, and 27% in the afternoon.

Fig. 4-5.2 Signal amplitudes received at 9.2 km to the SE of the source

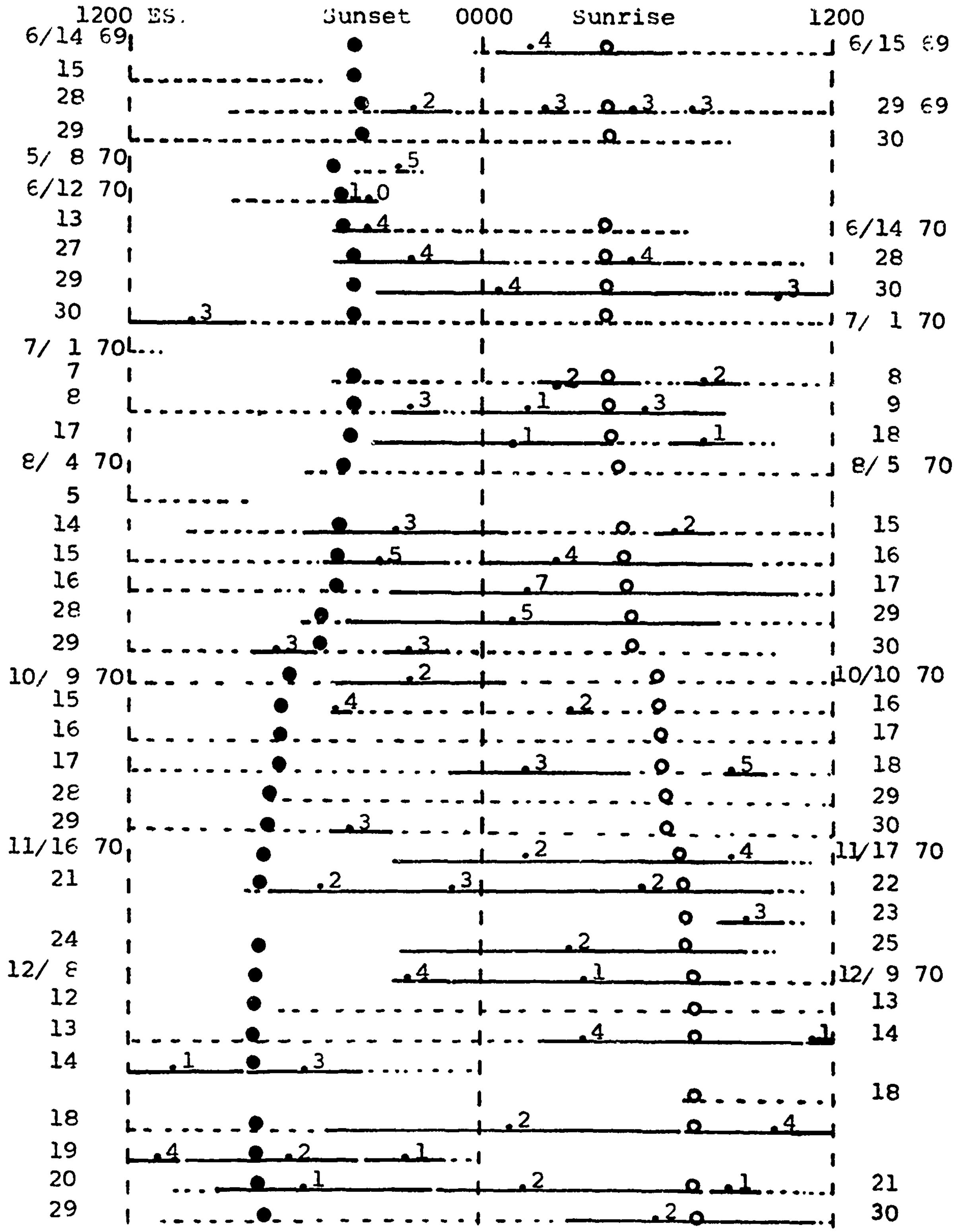

Remarks: The numbers with solid lines indicate the average focusing factors. The broken line indicates no detectable signal.

CHAPTER 5. CONCLUSIONS, RECOMMENDATIONS, AND APPLICATIONS

The infra-sonic wave probe has demonstrated its capability of measuring wind fluctuations and turbulence scales in the atmospheric boundary layer. The results are generally consistent with those of meteorological tower measurements and aircraft measurements. The inferred wind fluctuations averaged over the entire ray path are mostly smaller than the wind fluctuations monitored at 50 m-level. This seems to indicate that turbulence is stronger at 50 m-level than at the average signal propagating height, which is estimated to be about 140 m to 260 m from average signal amplitudes and synoptic meteorological information. The boundary layer eddies inferred from the probe data seem to be more elongated in horizontal directions than the eddies reported from tower measurements. The ratio of horizontal to vertical turbulence scales ranges from about 1/1 to 16/1 for horizontal turbulence scales of about 200 m to 1400 m. The vertical turbulence scale is 99 ± 28 m, which is roughly 57% of the average ray height and 30% of the boundary shear thickness.

Diurnal variations of temperature and wind structures in the atmospheric boundary layer have been indicated by average signal ampliutdes received at a location 9200 m to the SE of the signal source. Six fundamental effective wind profiles are used to predict ray trajectories and focusing factors of the probing signal at different times of the day. A shear vanishing height at about 200 m to 600 m seems to be often suggested by the nighttime probe data and pertinent meteorological information. Elevated effective wind shears are believed to be responsible for strong signal amplitudes, which are frequently observed at both ends of the daily signal receiving period, i.e., in the early evening as well as at about 4 to 6 hours after sunrise.

An array of receivers is recommended to increase the accuracy of probe measurements. By continuously measuring average signal amplitudes with several receivers located at various distances from the signal source, one could investigate time variations of effective wind profiles in detail. By measuring signal amplitude variations and phase shifts as functions of the travel distance with multi-receivers, one could test and improve theories of signal propagation in a random medium. By studying spatial correlations of signal amplitude variations and phase shifts, the structure of atmospheric turbulence and its effects on wave propagation could be better understood.

The probe seems to be ready to detect the wind fluctuations due to gravity waves. With an array of receivers deployed at different azimuthal angles with respect to the signal source, the chance of receiving clear signal fluctuations due to gravity wave winds would be greatly increased.

The probe could be used in air pollution meteorology. The horizontal wind fluctuation and vertical turbulence scale measured by the probe could help predict the horizontal dispersion and vertical mixing of pollutants in the atmospheric boundary layer. The shear vanishing height, which is indicated by average signal amplitudes over periods of hours, seems to be associated with weakly turbulent flows, and, therefore, could be important to certain air pollution problems (Slade 1969).

Appendix 1. The probe data

This appendix is a collection of tables listing all available field data and results of analysis. Examples showing how to analyze field data are given in Section 4-1, where the accuracy of these experimental results is also discussed.

Table A-1.1 Probe data (May 8, 1970, λ = 4.5 km)*

Time	Period	Sig. var.		Wind fluc.	Scale	
					Hori.	Vert.
	τ	$\sigma_p/\bar{p}$	σ_ϕ	σ_v	L_x	L_z
(EST)	(sec)		(rad)	(m/s)	(m)	(m)
1705	153	.089	.195			
1706	160	.026	.200			
1708	250	.053	.425			
Night aver.	188	.056	.273			

*The average signal amplitude has a focusing factor of 1.67. A positive curvature profile with zero surface shear and an effective wind of 7.3 m/s at the 300 m-level (Section 3-3), for example, could predict a caustic at the receiver. However, the simple ray theory can not determine the exact value of average signal amplitude near the caustic. The average wind seems to have blown along the source-receiver line in that evening. The cross wind component (V_{xav}) was, therefore zero. Then, according to the model of frozen turbulence drifting with the average wind (Section 3-5), the signal fluctuations were mainly caused by the turbulence near the source as well as near the receiver. Because of these special circumstances, the field data was not analyzed for average horizontal wind fluctuations and turbulence scales.

Table A-1.2 Probe data (June 30, 1970)

Time	Period	Sig. var.		Wind fluc.	Scale	
	τ	$\sigma_p/\bar{p}$	σ_ϕ	σ_v	Hori. L_x	Vert. L_z
(EST)	(sec)		(rad)	(m/s)	(m)	(m)
0136	41	.074	.207	.102	1058	101
0142	56	.156	.276	.117	889	80
0212	45	.074	.188	.088	1023	96
0226	56	.156	.420	.178	1070	99
0257	57	.200	.344	.144	878	79
0315	56	.156	.319	.135	947	86
0333	46	.151	.289	.134	901	84
0510	97	.168	.353	.113	1030	87
0514	96	.292	.652	.210	1058	90
Night aver.	61	.158	.339	.135	982	89

Table A-1.3 Probe data (Aug. 15, 1970)

Time	Period	Sig. var.		Wind fluc.	Scale	
					Hori.	Vert.
	τ	$\sigma_p/\bar{p}$	σ_ϕ	σ_v	L_x	L_z
(EST)	(sec)		(rad)	(m/s)	(m)	(m)
1916	131	.537	.695	.223	915	43
1928	95	.108	.156	.058	694	43
1943	107	.167	.416	.148	877	66
Night aver.	111	.271	.422	.143	830	53

Table A-1.4 Probe data (Aug. 16-17, 1970)

Time	Period	Sig.	var.	Wind fluc.	Scale	
					Hori.	Vert.
	τ	$\sigma_p/\bar{p}$	σ_Φ	σ_v	L_x	L_z
(EST)	(sec)		(rad)	(m/s)	(m)	(m)
2030	41	.131	.126	.062	392	61
2048	39	.082	.099	.051	433	68
0047	32	.044	.057	.031	436	70
0332	30	.074	.062	.036	354	57
0419	32	.094	.099	.056	399	64
1042	26	.163	.138	.104	206	66
1053	32	.106	.163	.110	267	90
Night aver.	35	.085	.089	.047	402	64
Conv. aver.	29	.134	.150	.107	236	78

Table A-1.5 Short-period probe data (Nov. 21-22,1970)

Time	Period	Sig. var.		Wind fluc.	Scale	
	τ	$\sigma_p/\bar{p}$	σ_ϕ	σ_v	Hori. L_x	Vert. L_z
(EST)	(sec)		(rad)	(m/s)	(m)	(m)
2155	69	.319	.695	.416	291	147
2300	50	.144	.289	.204	235	142
2324	50	.138	.195	.136	219	119
2351	45	.181	.225	.167	200	112
0021	56	.151	.262	.174	244	131
0034	50	.099	.138	.097	218	118
0232	38	.050	.089	.071	196	133
0320	56	.082	.138	.092	243	129
0351	45	.082	.119	.089	207	120
0430	50	.069	.082	.057	211	108
0610	45	.044	.074	.055	213	129
0633	41	.050	.057	.044	186	106
0740	45	.074	.062	.046	186	91
0808	60	.082	.106	.067	242	113
0924	38	.057	.057	.046	173	99
Night aver.	49	.114	.186	.128	219	122
Conv. aver.	49	.070	.082	.057	208	106

'able A-1.6 Long-period probe data (Nov. 21-22,1970)

Time	Period	Sig.	var.	Wind	Scale	
				fluc.	Hori.	Vert.
	τ	$\sigma_p/\bar{p}$	σ_ϕ	σ_v	L_x	L_z
(EST)	(sec)		(rad)	(m/s)	(m)	(m)
2330	338	.41	1.34	.41	1014	106
0015	390	.28	.90	.26	1170	105
0215	360	.21	.58	.17	1080	97
0230	255	.14	.33	.12	765	91
0440	375	.28	.76	.22	1125	96
0530	300	.20	.52	.17	900	95
0615	720	.67	.97	.20	2160	71
0740	900	.41	1.52	.28	2700	113
Night aver.	455	.325	.865	.23	1364	97

Table A-1.7 Probe data (Nov. 23, 1970)

Time	Period	Sig. var.		Wind fluc.	Scale	
	τ	$\sigma_p/\bar{p}$	σ_ϕ		Hori.	Vert.
				σ_v	L_x	L_z
(EST)	(sec)		(rad)	(m/s)	(m)	(m)
0916	41	.044	.099	.080	200	152
0920	35	.044	.082	.071	178	137
0924	45	.069	.168	.129	212	159
0928	38	.050	.089	.074	181	136
0931	56	.044	.138	.096	248	179
Conv. aver.	43	.050	.115	.090	204	153

Table A-1.8 Probe data (Dec. 14, 1970)*

Time	Period	Sig. var.		Wind fluc.	Scale	
	τ	$\sigma_p/\bar{p}$	σ_ϕ	σ_v	Hori. L_x	Vert. L_z
(EST)	(sec)		(rad)	(m/s)	(m)	(m)
0413	180	.370	1.57	.805	360	233
0424	100	.188	.482	.331	200	181
0449	41	.238	.714	.766	97	196
0510	75	.244	.425	.337	150	150
0852	112	.138	.539	.348	224	224
Night aver.	99	.260	.798	.560	202	190
Conv. aver.	112	.138	.539	.348	224	224

*The traces of signal records in that night looked very smooth (i.e., with little high frequency wiggles), despite large fluctuations with periods of a few minutes (Fig. 4-1.3). According to wind records, there were very little wind shears and wind fluctuations in the lowest 50 m-layer. Therefore, the signal variations could have been caused by wind and temperature fluctuations associated with an elevated effective wind shear, for which the ray theory may not be good enough to predict amplitude variations. Besides, no reliable average cross wind component (V_{xav}) can be computed from any available weather information. The adopted model with a V_{xav} of 2.0 m/s (Table A-1.10) is rather arbitrary. Consequently, the analysis is only tentative and the results may not be meaningful.

Table A-1.9 Probe data (Dec. 19, 1970)

Time	Period	Sig. var.		Wind fluc.	Scale	
					Hori.	Vert.
	τ	$\sigma_p/\bar{p}$	σ_ϕ	σ_v	L_x	L_z
(EST)	(sec)		(rad)	(m/s)	(m)	(m)
0555	225	.363	.588	.168	1153	80
0721	75	.082	.326	.161	454	131
0747	90	.062	.395	.179	570	166
0825	56	.082	.294	.168	316	136
0922	75	.144	.457	.227	413	117
0947	150	.464	.526	.184	769	88
1019	100	.126	.502	.214	513	126
1112	90	.126	.393	.177	462	111
1147	90	.195	.470	.213	462	97
1225	90	.131	.432	.195	462	114
1324	112	.126	.393	.160	574	111
Night aver.	104	.147	.412	.181	581	126
Conv. aver.	105	.195	.453	.191	540	104

Table A-1.10 The parabolic profiles used for the data analysis in Tables A-1.2 through A-1.9 ($Y = 9.2$ km)

Date	f_a	f	z_m	V_m	H	H_{av}	V_{xav}	ϑ
(1970)			(m)	(m/s)	(m)	(m)	(m/s)	(deg)
6/30	.40	.45	300	2.2	201	141	9.3	235
8/15	.36	.39	290	2.7	215	148	6.8	240
8/16-17	.40	.43	372	3.7	257	178	9.2	232
8/17	.41	.44	487	6.2	331	231	6.4	260
11/21-22	.25	.33	300	3.7	231	168	3.0	270
11/23	.29	.35	360	4.5	275	194	3.6	250
12/14	.22	.30	375	5.8	300	214	2.0	300
12/19	.34	.50	600	7.6	372	258	5.1	234

Remarks:

f_a = the apparent focusing factor inferred from the received signal amplitude.
f = the focusing factor estimated by correcting f_a for the dissipations due to relaxation and turbulence scattering (Section 3-1).
z_m = the shear vanishing height.
V_m = the maximum wind component.
H = the penetrating height.
H_{av} = the average ray height.
V_{xav} = the cross wind component at H_{av}.
ϑ = the prevailing wind direction.

Table A-1.11 Short-period wind fluctuations (November 21-22, 1970)

Time at (EST)	Period τ (sec)	Wind fluc. σ_v (m/s)	σ_{v50} (m/s)
2155	69	.42	1.24
2300	50	.20	.76
2324	50	.14	.80
2351	45	.17	.87
0021	56	.17	.74
0034	50	.10	.78
0232	38	.07	.41
0320	56	.09	.37
0351	45	.09	.35
0430	50	.06	.78
0610	45	.06	.39
0633	41	.04	.37
0740	45	.05	.32
0808	60	.07	.37
0924	38	.05	.71

Remarks:

The probe data are the same as listed in Table A-1.5.

σ_v = the rms wind fluctuation inferred from the probe data.

σ_{v50} = the rms wind fluctuation monitored at 50 m.

Table A-1.12 Long-period wind fluctuations (Nov. 21-22, 1970)

Time at (EST)	Period τ (sec)	Wind fluc. σ_v (m/s)	σ_{v50} (m/s)
2330	338	.41	.62
0015	390	.26	.32
0215	360	.17	.60
0230	255	.12	.33
0440	375	.22	.57
0530	300	.17	.32
0615	720	.20	.66
0740	900	.28	.39

Remarks:

σ_v = the rms wind fluctuation inferred from the probe data of Table A-1.6.

σ_{v50} = the rms wind fluctuation monitored at 50 m.

Appendix 2. Ray characteristics of fundamental effective wind profiles

THE NEGATIVE SHEAR PROFILE

For the negative shear profile,

$$V_e = - Sz, \tag{1}$$

the ray angle is

$$\alpha = (\alpha_o^2 + 2\,Sz/c_o)^{1/2}, \tag{2}$$

which does not vanish at any height. Therefore the ray will never bend back to the Earth's surface in the negative shear profile.

THE PARABOLIC PROFILE

For the parabolic profile,

$$V_e = S_o z \left[1 - z/(2z_m) \right] = (2V_m\, z/z_m) \left[1 - z/(2z_m) \right], \tag{3}$$

the ray angle vanishes at the penetrating height H, which is determined by

$$\alpha_o^2 - (2\, S_o H/c_o) \left[1 - H/(2\, z_m) \right] = 0, \tag{4}$$

whence

$$H = z_m \left\{ 1 - \left[1 - (\alpha_o/\alpha_m)^2 \right]^{1/2} \right\}, \tag{5}$$

where $\alpha_m = (S_o\, z_m/c_o)^{1/2} = (2\, V_m/c_o)^{1/2}$ is the maximum value of α_o for the signal to bend back to the Earth's surface.

The first half trajectory (from the source to the turning point) is

$$y = \int_o^z \left[dy \,/\, (\alpha_o^{\,2} - 2\,v_e \,/\, c_o)^{\frac{1}{2}}\right]$$

$$= (z_m/\alpha_m) \int_{-z_m}^{z-z_m} \left\{du/\left[u^2 - (1 - \alpha_o^{\,2}/\,\alpha_m^{\,2})\; z_m^{\,2}\right]^{\frac{1}{2}}\right\}$$

$$= \frac{z_m}{\alpha_m} \ln\left\{\frac{1 - \frac{z}{z_m} - \left[(1 - \frac{z}{z_m})^2 - (1 - \frac{\alpha_o^2}{\alpha_m^2})\right]^{\frac{1}{2}}}{1 - \frac{\alpha_o}{\alpha_m}}\right\}; \qquad (6)$$

and the second half trajectory (from the turning point to the landing point) is

$$y = \left\{\int_o^H + \int_z^H\right\}\left[dz \,/\, (\alpha_o^{\,2} - 2\,v_e/c_o)^{\frac{1}{2}}\right]$$

$$= \frac{z_m}{\alpha_m} \ln\left\{\frac{1 - \frac{z}{z_m} + \left[(1 - \frac{z}{z_m})^2 - (1 - \frac{\alpha_o^2}{\alpha_m^2})\right]^{\frac{1}{2}}}{1 - \frac{\alpha_o}{\alpha_m}}\right\}. \qquad (7)$$

The entire ray trajectory described by Eqs. (6) and (7) can be expressed in a single equation, i.e.,

$$z = z_m\left[1 + (\alpha_o/\alpha_m)\,\sinh\,(\alpha_m y/z_m) - \cosh\,(\alpha_m y/z_m)\right]. (8)$$

The travel distance is

$$Y = 2\int_o^H \left[dz/(\alpha_o^{\,2} - 2\,v_e/c_o)^{\frac{1}{2}}\right]$$

$$= (z_m/\,\alpha_m)\,\ln\,\left[(1 + \alpha_o/\,\alpha_m)/(1 - \alpha_o/\,\alpha_m)\right]$$

$$= (2z_m/\,\alpha_m)\,\tanh^{-1}\,(\alpha_o/\,\alpha_m). \qquad (9)$$

The average ray height is

$$H_{av} = (2/Y) \int_o^H \left[zdz/(\alpha_o^{\,2} - 2\, V_e/C_o)^{\frac{1}{2}} \right]$$

$$= z_m \left[1 - (\alpha_o/\alpha_m) / \tanh^{-1} (\alpha_o/\alpha_m) \right] . \qquad (10)$$

Since the derivative

$$\frac{\partial Y}{\partial \alpha_o} = (2\, C_o/S_o) / \left[1 - (\alpha_o/\alpha_m)^2 \right] ,$$

the focusing factor is

$$f = Y / \left[\left| \frac{\partial Y}{\partial \alpha_o} \right| \alpha_o \right]^{\frac{1}{2}}$$

$$= \left\{ \alpha_m \left[1 - (\alpha_o/\alpha_m)^2 \right] / (2\alpha_o) \right\}^{\frac{1}{2}} \left\{ \ln \left[(1+\alpha_o/\alpha_m)/(1-\alpha_o/\alpha_m) \right] \right\}^{\frac{1}{2}}$$

$$= \left[\frac{\alpha_m Y}{2z_m} \right]^{\frac{1}{2}} \left\{ \coth \left[\frac{\alpha_m Y}{2z_m} \right] - \tanh \left[\frac{\alpha_m Y}{2z_m} \right] \right\}^{\frac{1}{2}} , \qquad (11)$$

which is a function of either (α_o/α_m)

or $\alpha_m Y/(2z_m) = \left[Y/(2C_o)^{\frac{1}{2}} \right] V_m^{\frac{1}{2}} / z_m$.

With given Y and C_o, the f - contours on the log V_m vs. log z_m diagram are straight lines (Fig. 3-3.2).

The ray heights as fractions of z_m are functions of (α_o/α_m) and, hence, are also functions of the focusing factor f (Fig. 3-3.3).

THE LOGARITHMIC PROFILE

For the logarithmic profile

$$V_e = V_\ell \ \ln (z / z_o), \qquad (12)$$

the ray angle can be normalized

as
$$G = \left[G_o^{\,2} - \ln (z/z_o) \right]^{\frac{1}{2}}, \tag{13}$$

where $G = \alpha/\alpha_\ell$,

$G_o = \alpha_o/\alpha_\ell$,

and $\alpha_\ell = (2\, V_\ell/C_o)^{\frac{1}{2}}$.

The penetrating height is

$$H = z_o \exp (G_o^{\,2}). \tag{14}$$

The trajectory from the source to the turning point is

$$y = (1/\alpha_\ell) \int_{z_o}^{z} (dz/G)$$

$$= (-2z_o/\alpha_\ell) \exp (G_o^{\,2}) \int_{G_o}^{G} \exp (- G^2) dG$$

$$= \left[(\pi^{\frac{1}{2}} z_o/\alpha_\ell) \exp (G_o^{\,2}) \right] \left[\mathrm{erf}\, (G_o) - \mathrm{erf}\, (G) \right] , \tag{15}$$

where $\mathrm{erf}\, (G_o) = (2/\pi^{\frac{1}{2}}) \int_0^{G_o} \exp (- u^2)\, du.$

The trajectory from the turning point to the landing point is similarly obtained as

$$y = \left[(\pi^{\frac{1}{2}} z_o/\alpha_\ell) \exp (G_o^{\,2}) \right] \left[\mathrm{erf}\, (G_o) + \mathrm{erf}\, (G) \right]. \tag{16}$$

The travel distance is

$$Y = (2\, \pi^{\frac{1}{2}} z_o/\alpha_\ell) \exp (G_o^{\,2})\, \mathrm{erf}\, (G_o). \tag{17}$$

The average ray height is

$$H_{av} = z_o \exp (G_o^2) \operatorname{erf} (2^{\frac{1}{2}} G_o) / \left[2^{\frac{1}{2}} \operatorname{erf} (G_o) \right] \qquad (18)$$

Since the derivative

$$\frac{\partial Y}{\partial \alpha_o} = (4 z_o/\alpha_\ell^2) \left[1 + \pi^{\frac{1}{2}} G_o \exp (G_o^2) \operatorname{erf} (G_o) \right] ,$$

the focusing factor is

$$f = \left\{ \frac{\pi^{\frac{1}{2}} \exp (G_o^2) \operatorname{erf} (G_o)}{2 G_o \left[1 + \pi^{\frac{1}{2}} G_o \exp (G_o^2) \operatorname{erf} (G_o) \right]} \right\}^{\frac{1}{2}} . \qquad (19)$$

In a typical case, $V_\ell \sim 2$ m/s, $C_o \sim 331$ m/s. Then the normalizing angle

$\alpha_\ell = .11$ rad.

With an initial ray angle $\alpha_o \gtrsim .15$ rad, which is normalized as $G_o \gtrsim 1.4$, the error function

$\operatorname{erf} (G_o) \rightarrow 1$

(the error being less than 5%, see, e.g., Abramowitz et al 1964, p. 311). As a result, the following approximate formulas are applicable for $Y \gtrsim 250$ m.

$$Y = 2 \pi^{\frac{1}{2}} H/\alpha_\ell , \qquad (20)$$

$$H_{av} = H/2^{\frac{1}{2}} , \qquad (21)$$

$$f = 1 / \left\{ 2 \ln \left[\alpha_\ell Y/(2 \pi^{\frac{1}{2}} z_o) \right] \right\}^{\frac{1}{2}} . \qquad (22)$$

THE LINEAR PROFILE

For the linear profile

$$V_e = Sz , \qquad (23)$$

the penetrating height is

$$H = c_o \alpha_o^2/(2S). \qquad (24)$$

The trajectory is

$$y = (2\ c_o/S)^{\frac{1}{2}} \left[H^{\frac{1}{2}} \mp (H - z)^{\frac{1}{2}} \right]$$

or $$(y - c_o \alpha_o/S)^2 = (2\ c_o/S) \left[c_o \alpha_o^2/(2S) - z \right]. \qquad (25)$$

The travel distance is

$$Y = 2\ c_o \alpha_o/S. \qquad (26)$$

The average ray height is

$$H_{av} = c_o \alpha_o^2/(3S) \qquad (27)$$

$$= (2/3)H$$

The focusing factor is

$$f = 1, \qquad (28)$$

for which the second order term can be determined by first integrating the ray trajectory without shallow angle approximation and then expanding the result in small ray angles. Thus one gets

$$f = 1 - 5S^2\ Y^2\ /\ (32\ c_o^2), \qquad (29)$$

which decreases very slowly as Y increases.

THE POSITIVE CURVATURE PROFILES

The ray characteristics of the positive curvature profile type a

$$V_e = S_o\ z \left[1 + z/(2z_p) \right], \qquad (30)$$

can be obtained from the corresponding formulas of the parabolic profile by putting $z_m = - z_p$ and $\alpha_m = (-1)^{\frac{1}{2}} \alpha_p$, where $\alpha_p = (S_o\ z_p/C_o)^{\frac{1}{2}}$.

For the positive curvature profile type b

$$V_e = S_o\ z^2/(2z_p), \tag{31}$$

one gets the penetrating height

$$H = \alpha_o\ z_p/\alpha_p, \tag{32}$$

where $\alpha_p = (S_o\ z_p/C_o)^{\frac{1}{2}}$;

the ray trajectory

$$y = (z_p/\alpha_p)\left[\pi/2 \mp \cos^{-1}(z/H)\right],$$

or $$z = H \sin(\alpha_p Y/z_p); \tag{33}$$

the travel distance

$$Y = \pi z_p/\alpha_p; \tag{34}$$

the average ray height

$$H_{av} = (2/\pi)\ H \tag{35}$$

the focusing factor

$$f = \infty, \tag{36}$$

which means that a caustic is predicted at $\pi\ z_p/\alpha_p$ from the source.

For the positive curvature profile type c

$$V_e = S_o z\left[-1 + z/(2z_p)\right], \tag{37}$$

the penetrating height is

$$H = z_p\left\{1 + \left[1 + (\alpha_o/\alpha_p)^2\right]^{\frac{1}{2}}\right\}. \tag{38}$$

The first half trajectory is

$$y = \frac{z_p}{\alpha_p}\left\{ \sin^{-1} \frac{\frac{z}{z_p} - 1}{\left[1 + \left(\frac{\alpha_o}{\alpha_p}\right)^2\right]^{\frac{1}{2}}} + \cot^{-1}\left[\frac{\alpha_o}{\alpha_p}\right]\right\} \tag{39}$$

and the second half is

$$y = \frac{z_p}{\alpha_p}\left\{ \pi + \cot^{-1}\left[\frac{\alpha_o}{\alpha_p}\right] - \sin^{-1} \frac{\frac{z}{z_p} - 1}{\left[1 + \left(\frac{\alpha_o}{\alpha_p}\right)^2\right]^{\frac{1}{2}}}\right\}. \tag{40}$$

The entire trajectory can be expressed as

$$z = z_p\left\{ 1 + (\alpha_o/\alpha_p) \sin(\alpha_p y/z_p) - \cos(\alpha_p y/z_p)\right\}. \tag{41}$$

The travel distance is

$$Y = (2 z_p/\alpha_p)\left[\pi/2 + \cot^{-1}(\alpha_o/\alpha_p)\right]. \tag{42}$$

The average ray height is

$$H_{av} = z_p\left\{ 1 + (\alpha_o/\alpha_p)/\left[\pi/2 + \cot^{-1}(\alpha_o/\alpha_p)\right]\right\}. \tag{43}$$

The focusing factor is

$$f = (\alpha_p/\alpha_o)^{\frac{1}{2}}\left[1 + (\alpha_o/\alpha_p)^2\right]^{\frac{1}{2}}\left[\pi/2 + \cot^{-1}(\alpha_o/\alpha_p)\right]^{\frac{1}{2}}, \tag{44}$$

which predicts two caustics at the distances of $\pi z_p/\alpha_p$ and $2\pi z_p/\alpha_p$ from the source. All the rays land between $\pi z_p/\alpha_p$, & $2\pi z_p/\alpha_p$. The theory also predicts a skip distance of $\pi z_p/\alpha_p$, since no ray is received within this distance.

THE ELEVATED SHEAR PROFILES

The ray characteristics for elevated shears can be evaluated numerically (Wesson 1970), and the results are schematically shown in Fig. 3-3.4.

The interesting feature of elevated shear types b and c is the skip distance Y_{mini}, where a caustic is also predicted. Y_{mini} can be estimated by using a two-layer model. The lower layer of a thickness of h_1 has a negative shear $-S_1$ and the upper layer has a positive shear S_2. Then the horinontal travel distance in the lower layer is

$$(2\ c_o/S_1)\left[(\alpha_o^{\ 2} + 2S_1\ h_1/c_o)^{\frac{1}{2}} - \alpha_o'\right],$$

and that in the upper layer is from Eq. (26)

$$(2\ c_o/S_2)\ (\alpha_o^{\ 2} + 2S_1\ h_1/c_o)^{\frac{1}{2}}.$$

The total travel distance is the sum of these, i.e.,

$$Y = \frac{2c_o}{S_1}\ (1 + \frac{S_1}{S_o})\ (\alpha_o^{\ 2} + \frac{2S_1\ h_1}{c_o})^{\frac{1}{2}} - \frac{2c_o\ \alpha_o}{S_1}\ . \quad (45)$$

By putting the derivative $\frac{\partial Y}{\partial \alpha_o}$ to vanish and solving for the value of α_o, one gets

$$(\alpha_o)_{mini} = (2S_1\ h_1/c_o)^{\frac{1}{2}} \Big/ \left[(1 + S_1/S_2)^2 - 1\right]^{\frac{1}{2}} \quad (46)$$

Substitution of Eq. (46) into Eq. (45) gives

$$Y_{mini} = 2\ (2c_o h_1/S_1)^{\frac{1}{2}} \left[(1+S_1/S_2)^2 - 1\right]^{\frac{1}{2}},\ \text{(type c)} \quad (47)$$

which is the skip distance for elevated shear type c. The skip distance for elevated shear type b is obtained from Eq. (47) by setting S_1 to zero, i.e.,

$$Y_{mini} = 4\ (C_o\ h_1/S_2)^{\frac{1}{2}}. \qquad \text{(type b)} \qquad (48)$$

Appendix 3. Parabolic profile fluctuations

According to the linear theory, the time rate of fractional change of amplitude is

$$f_a = \frac{d}{dt}(\ln p)$$

$$= S_o \frac{d}{dt}(\ln S_o)\frac{d}{dS_o}(\ln p) + z_m \frac{d}{dt}(\ln z_m)\frac{d}{dz_m}(\ln p). \quad (1)$$

And the fractional doppler is

$$f_d = \Delta\omega/\omega$$

$$= \frac{d}{dt}(\ln S_o)\, D_{So} + \frac{d}{dt}(\ln z_m)\, D_{zm}, \quad (2)$$

where, according to Eq. (4) in Section 3-1,

$$D_{So} = (2S_o/C_o^2)\int_0^H dz\left(\frac{\partial\, e}{\partial S_o}/\alpha\right), \quad (2a)$$

and $D_{zm} = (2z_m/C_o^2)\int_0^H dz\left(\frac{\partial\, e}{\partial z_m}/\alpha\right).$ (2b)

Here the effect of penetrating height variations on the doppler is negligible to the first order.

To calculate $\frac{d}{dM}(\ln p)$ (M stands for S_o or z_m), one should consider that both source and receiver are fixed in position, and, therefore, the derivative includes two terms, i.e.,

$$\frac{d}{dM} = \frac{\partial}{\partial M} + \frac{\partial\alpha_o}{\partial M}\frac{\partial}{\partial\alpha_o}. \quad (3)$$

The first term is due to the explicit dependence of p on M. The second term arises because of the adjustment of the initial ray angle, α_o, to insure a constant horizontal travel distance, , while M is varying. A constant means that

$$\frac{\partial Y}{\partial M}\, dM + \frac{\partial Y}{\partial \alpha_o}\, d\alpha_o = 0, \tag{4}$$

whence

$$\frac{\partial \alpha_o}{\partial M} = -\frac{\partial Y}{\partial M} \Big/ \frac{\partial Y}{\partial \alpha_o}\,. \tag{5}$$

Now from Eq. (7) in Section 3-2, one obtains

$$\frac{\partial}{\partial M}(\ln p) = \frac{-1}{2}\left[\frac{\partial}{\partial M}\left(\frac{\partial Y}{\partial \alpha_o}\right) \Big/ \frac{\partial Y}{\partial \alpha_o} + \frac{\partial \alpha_o}{\partial M}\Big/\alpha_o\right]$$

$$= \frac{-1}{2}\left[\left(\frac{\partial^2 Y}{\partial M\, \partial \alpha_o} + \frac{\partial \alpha_o}{\partial M}\frac{\partial^2 Y}{\partial \alpha_o^2}\right) \Big/ \left(\frac{\partial Y}{\partial \alpha_o}\right) + \frac{\partial \alpha_o}{\partial M}\Big/\alpha_o\right] \tag{6}$$

After doing the algebra of Eqs. (6) and (2), one gets

$$-S_o \frac{\partial}{\partial S_o}(\ln p) = z_m \frac{d}{dz_m}(\ln p)$$

$$= (\tfrac{1}{4})\left\{\left[S_o Y/(2\, C_o \alpha_o)\right]\left[1 + (\alpha_o/\alpha_m)^2\right] - 1\right\} \tag{7a}$$

$$D_{So} = \left[z_m \alpha_o/(2\, C_o)\right]\left\{\left[S_o Y/(2\, C_o \alpha_o)\right]\left[1 + (\alpha_o/\alpha_m)^2\right] - 1\right\} \tag{7b}$$

$$D_{zm} = \left(3\, z_m \alpha_o/(2\, C_o)\right)\left\{\left[S_o Y/(2\, C_o \alpha_o)\right]\left[1 - (\alpha_o/\alpha_m)^2/3\right] - 1\right\} \tag{7c}$$

Substitution of Eq. (7) into Eqs. (1) and (2) gives Eqs. (1) and (2) in Section 3-4.

Appendix 4. Phase shifts and amplitude variations due to short-period effective wind fluctuations

The phase shift, $\Delta\phi$, is related to the travel time fluctuation, ΔT, as

$$\Delta\phi = -\omega\Delta T, \qquad (1)$$

where ω is the angular frequency. With the shallow angle approximation, the travel time can be written from Eq. (2) in Section 3-1 as

$$T = \int_0^Y dy/\frac{dy}{dt}$$

$$= (1/\bar{c})\int_0^Y dy\left[1 - (\varepsilon + \bar{V}_y + v_y)/\bar{c}\right], \qquad (2)$$

where one has assumed both sound speed and wind to have average parts and fluctuating parts, i.e.,

$$c = \bar{c} + \varepsilon$$

$$V_y = \bar{V}_y + v_y.$$

From Eqs. (1) and (2), one gets the phase shift

$$\Delta\phi = (\omega/\bar{c})\int_0^Y dy\,(\Delta v_e/\bar{c}), \qquad (3)$$

where $\Delta v_e = \Delta\varepsilon + \Delta v_y$ is the fluctuating effective wind. The mean square phase shift is

$$\overline{(\Delta\phi)^2} = \omega^2/\bar{c}^4\int_0^Y dy_1\int_0^Y dy_2\,\overline{\left[\Delta v_e(x_1,y_1,z_1)\right]\left[\Delta v_e(x_2,y_2,z_2)\right]} \qquad (4)$$

By assuming the Gaussian form of correlation function, i.e.,

$$\overline{\left[\Delta v_e(x_1,y_1,z_1)\right]\left[\Delta v_e(x_2,y_2,z_2)\right]} = \overline{(\Delta v_e)^2}\exp\left[-\left(\frac{x_1-x_2}{a_x}\right)^2 - \left(\frac{y_1-y_2}{a_y}\right)^2 - \left(\frac{z_1-z_2}{a_z}\right)^2\right], \qquad (5)$$

one can change the integration variables of Eq. (4) into

$\vec{r}_o = (\vec{r}_1 + \vec{r}_2)/2$

= the center-of-mass coordinate,

$\vec{r}' = \vec{r}_2 - \vec{r}_1$

= the separation coordinate,

and

$$(\Delta\phi)^2 = [\omega^2 (\Delta v_e)^2/\bar{c}^4] \int_0^Y dy_o \int_{-Y}^{Y} dy' \cdot$$

$$\cdot \exp\left[-(x'/a_x)^2 - (y'/a_y)^2 - (z'/a_z)^2\right] \quad (6)$$

The integration limits for y can be set to $\pm\infty$, since Y is much greater than a_y. To the first order, the integral can be evaluated at x' = z' = 0, assuming that the deviations of the actual ray trajectories from the average trajectory are small in comparison with a_x and a_z. Then Eq. (6) can be evaluated as

$$\overline{(\Delta\phi)^2} = (\pi^{1/2}\omega^2 a_y Y/\bar{c}^4)\ \overline{(\Delta v_e)^2}. \quad (7)$$

With the y - coordinate (Fig. 3-1.1) as the integration variable, the signal amplitude is given by

$$p = \left[2 P \rho c_o \Big/ \left(\pi \left|\frac{\partial Z}{\partial \alpha_o} \frac{\partial X}{\partial \gamma_o}\right|\right)\right]^{1/2}, \quad (8)$$

where α_o = the initial vertical spreading angle,

$\gamma_o = \frac{\pi}{2} - \beta_o$

= the initial spreading angle in the x-direction.

Then the fractional amplitude fluctuation is

$$\Delta p/\bar{p} = (-1/2)\left[\Delta\left(\frac{\partial Z}{\partial\alpha_o}\right)\Big/\left(\overline{\frac{\partial Z}{\partial\alpha_o}}\right) + \Delta\left(\frac{\partial X}{\partial\gamma_o}\right)\Big/\left(\overline{\frac{\partial X}{\partial\gamma_o}}\right)\right]. \quad (9)$$

The average value of the derivative $\frac{\partial Z}{\partial \alpha_o}$ can be obtained from the trajectories, which are evaluated for fundamental effective wind profiles in Section 3-3. The average $\frac{\partial X}{\partial \gamma_o}$ is equal to Y, the same as in a uniform medium. The randomly fluctuating derivatives, $\Delta\left(\frac{\partial Z}{\partial \alpha_o}\right)$ and $\Delta\left(\frac{\partial X}{\partial \gamma_o}\right)$, are now to be derived. For $\Delta\left(\frac{\partial Z}{\partial \alpha_o}\right)$, one needs Z as an integral in y, which is obtained from Eq. (2) in Section 3-1 and the shallow angle approximation as

$$Z = \int_0^Y dy \left[(C \sin\alpha + v_z)/(C \cos\alpha + v_y)\right]$$

$$= \int_0^Y dy \left[\alpha - (\epsilon + \bar{v}_y + v_y + v_z)/\bar{c}\right], \qquad (10)$$

whence

$$\frac{\partial Z}{\partial \alpha_o} = \int_0^Y dy \left(\frac{\partial \alpha}{\partial \alpha_o} - \frac{\partial}{\partial \alpha_o}(\varepsilon + \bar{v}_y + v_y + v_z)/\bar{c}\right] \qquad (11)$$

The elevation angle α is from Eqs. (2) and (3) in Section 3-1

$$\alpha = \alpha_o + \int_0^Y dy \left(\frac{1}{k}\frac{\partial k_z}{\partial t} \Big/ \frac{\partial y}{\partial t}\right)$$

$$= \alpha_o + \int_0^Y dy \left[\left(-\frac{\partial c}{\partial z} - \vec{n}\cdot\frac{\partial \vec{V}}{\partial z}\right)\Big/(c + v_y)\right]$$

$$= \alpha_o - (1/\bar{c}) \int_0^Y dy \left(\frac{\partial \varepsilon}{\partial z} + \frac{\partial \bar{v}_y}{\partial z} + \frac{\partial v_y}{\partial z}\right), \qquad (12)$$

whence

$$\frac{\partial \alpha}{\partial \alpha_o} = 1 - (1/\bar{c}) \int_0^Y dy \left[\frac{\partial}{\partial \alpha_o}\left(\frac{\partial \varepsilon}{\partial z} + \frac{\partial \bar{v}_y}{\partial z} + \frac{\partial v_y}{\partial z}\right)\right]. \qquad (13)$$

Substituting Eq. (13) in Eq. (11), taking the variation of fluctuating parts, and neglecting the second order terms, one gets

$$\Delta\left(\frac{\partial z}{\partial \alpha_o}\right) = (-1/\bar{c}) \int_o^Y dy \int_o^y d\eta \left[\frac{\partial^2 (\Delta v_e)}{\partial z^2} \frac{\partial z}{\partial \alpha_o}\right], \qquad (14)$$

where, for $\frac{\partial z}{\partial \alpha_o}$, one can use the average trajectories given in Section 3-3. Similarly, one has the random spreading in the x-direction as

$$\Delta\left(\frac{\partial x}{\partial \gamma_o}\right) = (-1/\bar{c}) \int_o^Y dy \int_o^y d\eta \left[\frac{\partial^2 (\Delta v_e)}{\partial x^2} \frac{\partial x}{\partial \gamma_o}\right], \qquad (15)$$

where, again, one can use the average spreading for $\frac{\partial x}{\partial \gamma_o}$, i.e., y.

For the linear profile, the fractional amplitude variation can now be written as

$$\Delta p/\bar{p} = \left[1/(2\bar{c}Y)\right] \int_o^Y dy \int_o^y d\eta\, \eta \left[\left(\frac{\partial^2}{\partial x^2} + \frac{\partial^2}{\partial z^2}\right)(\Delta v_e)\right]. \qquad (16)$$

Integration by parts transforms this into the form

$$\Delta p/\bar{p} = \left[1/(2\bar{c}Y)\right] \int_o^Y dy\, y\,(Y - y) \left[\left(\frac{\partial^2}{\partial x^2} + \frac{\partial^2}{\partial z^2}\right)(\Delta v_e)\right]. \qquad (17)$$

The mean square fractional amplitude variation is

$$\overline{(\Delta p)^2}/\bar{p}^2 = \left[1/(4\bar{c}^2 Y^2)\right] \int_o^Y dy_1 \int_o^{Y} dy_2\, y_1\, y_2\, (Y - y_1)(Y_1 - y_2) \cdot$$

$$\cdot \left\{\left(\frac{\partial^2}{\partial x_1^2} + \frac{\partial^2}{\partial z_1^2}\right)\left(\frac{\partial^2}{\partial x_2^2} + \frac{\partial^2}{\partial z_2^2}\right) \overline{\left[(\Delta v_e(\vec{r}_1)\right]\left[\Delta v_e(\vec{r}_2)\right]}\right\}$$

$$=\left[\overline{(\Delta v_e)^2}/(4\,\bar{c}^2\,Y^2)\right]\int_0^Y dy_o \int_{-Y}^{Y} dy'\,(y_o^{\,2} - y'^2/4)\,\cdot$$

$$\cdot\,(Y^2 - 2y_o\,Y + y_o^{\,2} - y'^2/4)\,\cdot$$

$$\cdot\left\{\left(\frac{\partial^2}{\partial x'^2} + \frac{\partial^2}{\partial z'^2}\right)^2 \exp\left[-(x'/a_x)^2 - (y'/a_y)^2 - (z'/a_z)^2\right]\right\} \quad (18)$$

Here the center-of-mass coordinate, r_o, the separation coordinate, r', and the Gaussian correlation function have been used. By noting that $Y \gg a_y$, and assuming small deviations of actual ray trajectories from the average trajectory, one can evaluate the integrations of Eq. (18) and obtain

$$\overline{(\Delta p)^2}/\bar{p}^2 = \left[\overline{(\Delta v_e)^2}\;a_y/\bar{c}^2\right]\cdot$$

$$\cdot\left[(\pi^{\frac{1}{2}}\,Y^3/10)/a_z + (\pi^{\frac{1}{2}}Y^3/15)\,/\,(a_z^{\,2}\,a_x^{\,2})\right.$$

$$\left.+\,(\pi^{\frac{1}{2}}Y^3/10)\,/\,a_x^{\,4}\right] \quad (19)$$

Similarly, one can derive the mean square fractional amplitude fluctuation for the parabolic profile as

$$\overline{(\Delta p)^2}/\bar{p}^2 = \left[\overline{(\Delta v_e)^2}\;a_y/\bar{c}^2\right]\cdot$$

$$\cdot\left[K_1\,/\,a_z^{\,4} + K_2/(a_z^{\,2}\,a_x^{\,2}) + K_3\,/\,a_x^{\,4}\right], \quad (20)$$

where

$$K_1 = \left\{3\,\pi^{\frac{1}{2}}\,Y\,(z_m/\alpha_m)^2/\left[4\,\sinh^2(Y^*)\right]\right\}\cdot$$

$$\cdot\left[\sinh(2\,Y^*)\,/\,(2\,Y^*) - 1 - (2/3)\,(Y^*)^2\,\exp\,(a_y^{\,*}/2)^2\right],$$

$$K_2 = \left[4 \pi^{1/2} \exp \ (a_y^* / 4)^2 \ (z_m / \alpha_m)^3 \ / \ \sinh (Y^*) \right] \cdot$$

$$\cdot \left[2 + \cosh (Y^*) - (3 / Y^*) \sinh (Y^*) \right],$$

$$K_3 = \pi^{1/2} Y^3 / 10,$$

$$Y^* = Y \alpha_m / z_m,$$

$$a_y^* = a_y \alpha_m / z_m,$$

$$\alpha_m = (2 V_m / C_o)^{1/2} = (S_o z_m / C_o)^{1/2},$$

$$\exp \ (a_y^* / 2)^2 \sim \exp \ (a_y^* / 4)^2 \sim 1.$$

REFERENCES

Abramowitz, Milton and Irene A. Stegun 1964
Handbook of Mathematical Tables
U. S. National Bureau of Standards Applied Mathematics Series 55 (1964)

Batchelor, G. K. 1957
Wave scattering due to turbulence
Symposium on Naval Hydrodynamics (F. S. Sherman, Ed., 1957) pp. 409-430

Bunker, Andrew F. 1955
Turbulence and shearing stresses measured over the North Atlantic Ocean by an airplane-acceleration technique
J. Meteor. Vol. 12 (Oct. 1955) pp. 445-455

Byzova, N. L., V. N. Ivanov and S. A. Morozov 1965
Characteristics of the wind velocity and temperature fluctuations in the atmospheric boundary layer
Proceedings of the international colloquim on atmospheric turbulence and radio wave propagation (Moscow, 1965) publishing house "NAUKA" Moscow (1967) pp. 76-92

Chernov, Lev A. 1960
Wave propagation in a random medium
Dover Pub., Inc. New York (1960)

Cole, John E. III and Richard A. Dobbins 1970
Propagation of sound through atmospheric fog
J. the Atmos. Sci. Vol. 27 (1970) pp. 426-434

Daniels, Fred B. 1959
Noise-reducing line microphone for frequencies below 1 cps
J. Acous. Soc. Am. Vol. 31, No. 4 (April 1959) pp. 529-531

Gardner, Floyd Martin 1967
Phaselock techniques
New York Wiley (1967)

Haurwitz, Bernhard 1941
Dynamic Meteorology
McGraw-Hill Book Company, Inc. (1941)

Hayes, Wallace D. 1970
Kinematic wave theory
Proc. Roy. Soc. Lond. Vol. A320 (1970) pp. 209-226

Huschke, Ralph E. 1959
Glossary of Meteorology
Am. Meteor. Soc., Boston, Mass. (1959)

Kneser, H. C. 1965
Relaxation processes in gases
"Physical Acoustics" (W. P. Mason, Ed.), Academic Press Inc., New York Vol. 2A (1965) pp. 133-202

Lettau, Heinz H. and Ben Davidson 1957
Exploring the atmosphere's first mile
Pergamon Press (1957) Two volumes
(Aircraft measurements are described on pp. 267-275, 471, and 495-496)

Lighthill, M. J. 1965
Group velocity
J. Inst. Math. Appl. Vol. 1, (1965) pp. 1-28

Lumley, John L. and Hans A. Panofsky 1964
The structure of atmospheric turbulence
Interscience Publishers (1964)

Madden, T. R. and J. F. Claerbout 1968
Jet stream associated gravity waves and implications concerning jet stream stability
Symposium proceedings on "acoustic-gravity waves in the atmosphere" at Boulder, Colorado on 15-17 July 1968 (ed., T. M. Georges) pp. 121-134

Morse, Philip M. 1948
Vibration and sound
McGraw-Hill Book Company, Inc., 2nd edition (1948)

Morse, Philip M. and K. Uno Ingard 1968
Theoretical acoustics
McGraw-Hill Book Co. (1968)

Obuchow, A. M. 1953
Über den Einfluss schwacher Inhomogenitäten der Atmosphäre auf die Schall- und Lichtausbreitung
"Sammelband zur statistischen Theorie der Turbulenz" (edited and translated by Herbert Goering) Akademie-Verlag Berlin (1958) pp. 157-171

Olson, Harry F. 1947
Elements of acoustic engineering
D. Van Nostrand Co., Inc. 2nd Ed. (1947)

Panofsky, H. A. and I. A. Singer 1965
Vertical structure of turbulence
Quart. J. Roy. Meteor. Soc. Vol. 91 (1965) pp. 339-344

Pielke, R.A. and H. A. Panofsky 1970
Turbulence characteristics along several towers
Boundary-Layer Meteor. Vol. 1 (1970) pp. 115-130

Piercy, J. E. 1969
Role of the vibrational relaxation of nitrogen in the absorption of sound in air
J. Acous. Soc. Am. Vol. 46 (1969) pp. 602-604

Slade, David H. 1969
Low turbulence flow in the planetary boundary layer and its relation to certain air pollution problems
J. Appl. Meteor., 8 (Aug. 1969) pp. 514-522

Tatarski, V. I. 1961
Wave propagation in a turbulent medium
Dover Pub., Inc. New York (1961)

Taylor, G. I. 1935
Statistical theory of turbulence
Proc. Roy. Soc. Lond. Vol. A151 (1935) pp. 421-478

Thuillier, R. H. and U. O. Lappe 1964
Wind and temperature profile characteristics from observations on a 1400 ft tower
J. Appl. Meteor. Vol. 3 (June 1964) pp. 299-306

Wesson, Robert L. 1970
A time Integration method for computation of the intensities of seismic waves
Bull. Seis. Soc. Am. Vol. 60, No.2 (1970) pp. 307-316

ACKNOWLEDGEMENTS

I am most indebted to Professor T. R. Madden for his guidance and encouragement throughout the course of this thesis. He designed all of the electronic circuits, and shared many of the exploratory field trips with me. I would also like to acknowledge very helpful discussions with K. Aki, John M. Brown, L. W. Dean, Tom De Fazio, Dave Fitterman, D. P. Keily, E. L. Mollo-Christensen, A. D. Pierce, F. Sanders, and Ron Ward.

My sincere thanks also go to Sam Hendryx, George Dumont, and many others who have kindly assisted in carrying out the experiments.

I express my affectionate gratitude for my wife's understanding, sacrifice, and skillful typing, and to my late father-in-law, Mr. Yen-Ching Lin, without whose generosity my study at M.I.T. would never have been possible.

General support was received from the U.S. Army Research Office Contract No. DA-31-124-ARO-431.

BIOGRAPHICAL NOTE

The author received his undergraduate education at National Taiwan University, China, and obtained a B.S. in Physics in 1961. He attended graduate school at National Tsing-Hua University, Taiwan, China from 1961 to 1963 (M.S.) as well as at MIT, U.S.A. from 1965 to 1972 (Ph.D.).

The author was married to Shu-Mei Lin in 1964. They have a daughter named Iris Ting-Lan Chung.